Volume 10, Number 1, Winter 2024

ACERP
Advanced Ceramics Progress

ISSN 2423-7477
e-ISSN 2423-7485

# Advanced Ceramics Progress

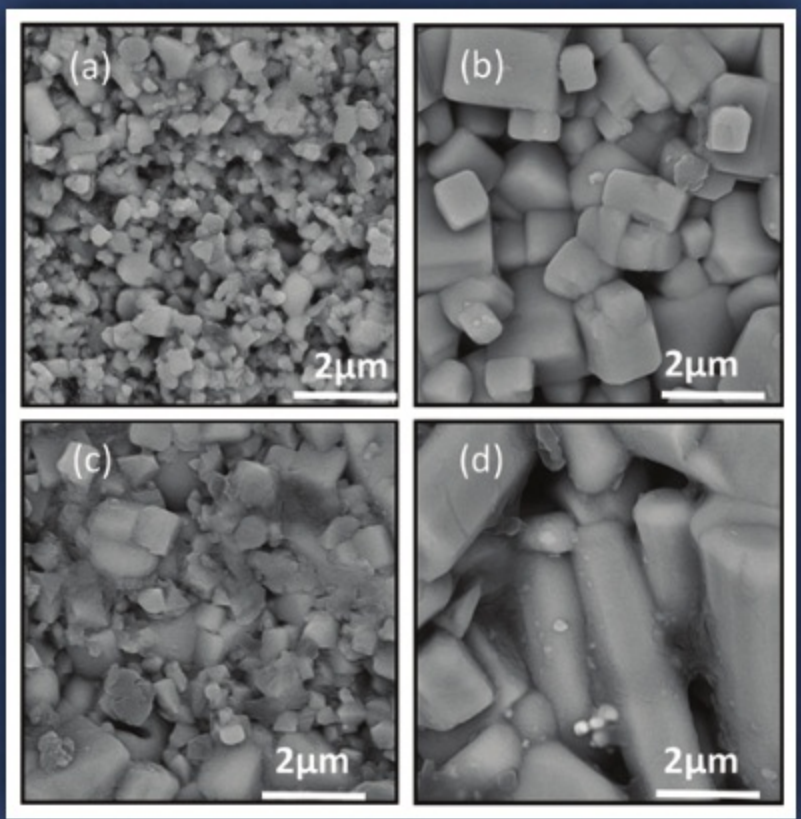


Materials and Energy
Research Center

Iranian Ceramic Society

*In The name of God*

# *Advanced Ceramics Progress*


**DIRECTOR-IN-CHARGE**
**H. Omidvar**
Amirkabir University of Technology, Tehran, Iran

**EDITOR-IN-CHIEF**
**M. R. Rahimipour**
Materials and Energy Research Center, Karaj, Iran

**EXECUTIVE MANAGER**
**M. Razavi**, Materials and Energy Research Center, Karaj, Iran

## Editorial Board

**A. R.Aghaei**, Materials and Energy Research Center, Karaj, Iran

**P. Alizadeh**, Tarbiat Modares University, Tehran, Iran

**T. Ebadzadeh**, Materials and Energy Research Center, Karaj, Iran

**M. A.Faghihi Sani**, Sharif University of Technology, Tehran, Iran

**M. Ghassemi Kakroudi,** University of Tabriz, Tabriz, Iran

**A.R. Khavandi,** Iran University of Science& Technology, Tehran, Iran

**M. M. Mohebi**, Imam Khomeini University, Qazvin, Iran

**H. Omidvar**, Amirkabir University of Technology, Tehran, Iran

**M. R. Rahimipour**, Materials and Energy Research Center, Karaj, Iran

**M.Razavi**, Materials and Energy Research Center, Karaj, Iran

**E. Salahi**, Materials and Energy Research Center, Karaj, Iran

**M. Salehi**, Isfahan University of Technology, Isfahan, Iran

**M. T. Salehi**, Iran University Science and Technology, Tehran, Iran

**Ştefan Ţălu**, Technical University of Cluj-Napoca, Romania

**EDITORIAL ADVISORY BOARD**
Ş. Ţălu, F.S. Torknik

**MANAGING EDITOR**
M. Fouladian

**ENGLISH LANGUAGE EDITUR**
M. Sabzevari

**TECHNICAL STAFF**
M.Fouladian, V. Hajabdolali, R. Chaluei



**DISCLAIMER**
The publication of papers in Advanced Ceramics Progress does not imply that the editorial board, editorial advisory board, reviewers or the publisher accept, approve or endorse the data and conclusions of authors.



**A**dvanced **Cer**amics **P**rogress (ISSN 2423-7477) (e-ISSN 2423-7485)

Web Site: www.acerp.ir, E-mail: office@acerp.ir
Tel: +98 (0) 26 36280040-7 ext.: 173, Fax: +98 (0) 26 36201888
Tel:+98 (0)21 88771626-7 ext.: 8931, Fax: +98 (0)21 88773352

Materials and Energy Research Center (MERC); Iranian Ceramic Society (ICERS)

ISSN: 2423-7477; e-ISSN: 2423-7485

Advanced Ceramics Progress: Vol. 10 , No. 1, (Winter 2024) 1-48

CONTENTS

## AIMS AND SCOPE

*Advanced Ceramics Progress* (ACERP) as an ISC international journal is devoted to elucidating the fundamental aspects of chemistry and physics occurring at a wide range of oxide and nonoxide ceramics and composite materials and their processing, microstructure, properties, and applications. The journal provides a unique venue for publishing new exciting research, focusing on dynamic growth areas in this field.

## INSTRUCTIONS FOR AUTHORS

Submission of manuscript represents that it has neither been published nor submitted for publication elsewhere and is result of research carried out by author(s).
Authors are required to include a list describing all the symbols and abbreviations in the paper. Use of the international system of measurement units is mandatory.

- On-line submission of manuscripts results in faster publication process and is recommended. Instructions are given in the ACERP web site: www.acerp.ir
- Hardcopy submissions must include MS Word and jpg files.
- Manuscripts should be typewritten on one side of A4 paper, double-spaced, with adequate margins.
- References should be numbered in brackets and appear in sequence through the text. List of references should be given at the end of the paper.
- Figures' captions are to be indicated under the illustrations. They should sufficiently explain the figures.
- Illustrations should appear in their appropriate places in the text.
- Tables and diagrams should be submitted in a form suitable for reproduction.
- Photographs should be of high quality saved as jpg files.
- Tables, illustrations, figures and diagrams will be normally printed in single column width (8 cm). Exceptionally large ones may be printed across two columns (17 cm).

## PAGE CHARGES AND REPRINTS

ACERP subscribers do not need to make any payment for publication and reprints.

## AUTHORS CHECKLIST

- Author(s), bio-data including affiliation(s) and mail and e-mail addresses.
- Manuscript including abstract, key words, illustrations, tables, figures with figures' captions and list of references.
- MS Word files of the paper.

**A**dvanced **Cer**amics **P**rogress,
P.O. Box 31787-316, Karaj, Alborz, I. R. Iran
Materials and Energy Research Center, Imam Khomeini Blvd, Meshkin Dasht, Karaj, Alborz, I. R. Iran
P.O. Box 14155-4777, Tehran, I. R. Iran
No. 5, Ahuramazda St., Alvand Ave., Argentine Sq., Tehran, I. R. Iran

www.merc.ac.ir - www.acerp.ir

Advanced Ceramics Progress: Vol. 10, No. 1, (Winter 2024) 1-10

Materials and Energy Research Center
MERC

Contents lists available at **ACERP**

Advanced Ceramics Progress

Journal Homepage: www.acerp.ir

**Original Research Article**

# Gamma-ray Shielding Capacity of Ceramics Tb and Fe Doped with $Y_2Zr_2O_7$

Mohamadreza Alipoor [a], Mahdi Eshghi [b] *

[a] *PhD Candidate, Department t of Physics, Imam Hossein Comprehensive University, Tehran, Iran.*
[b] *Assistant Professor, Department t of Physics, Imam Hossein Comprehensive University, Tehran, Iran.*

* Corresponding Author Email: eshgi54@gmail.com. meshghi@ihu.ac.ir (Mahdi Eshghi) URL: https://www.acerp.ir/article_206532.html

*ARTICLE INFO*

*Article History:*
Received: 03 December 2023
Revised: 06 April 2024
Accepted: 07 September 2024

*Keywords*:
Monte Carlo Simulations,
Gamma-ray Shielding,
Attenuation Coefficient,
Ceramics.

*ABSTRACT*

In this research, a Monte Carlo simulation was used to estimate the gamma-ray shielding properties of ceramics doped with Tb and Fe in $Y_2Zr_2O_7$, within the photon energy range of 0.015 to 15 MeV. We calculated the linear and mass attenuation coefficients, half-value layer, tenth-value layer, mean free path, effective atomic number, and fast neutron removal cross section. To validate the simulation, the results were compared with data obtained from the Phy-X program. It was observed that the data from the Phy-X program and the Geant 4 simulation tool were in good agreement. The ceramic sample YTF015, due to the addition of terbium, showed a significant increase in densification and microstructural development, leading to improved flexural strength and enhanced protection against fast neutrons and gamma radiation. The results indicate that energy levels significantly affect gamma-ray penetration. Furthermore, for the photon energy of 0.511 MeV, where the mass attenuation coefficient increased from 0.058 to 0.096 $cm^2/g$, YTF015 demonstrated superior shielding performance against gamma rays compared to other samples. In conclusion, YTF015 ceramics exhibited strong shielding properties, achieving 35% to 55% of the shielding capacity of pure lead element in the intermediate energy range of 0.1 to 2 MeV. This shows that the composition and microstructure of ceramic materials can be optimized to improve damping properties for applications in medical physics applications.

https://doi.org/10.30501/acp.2024.428521.1140

## 1. INTRODUCTION

Gamma rays are the most penetrating form of ionizing radiation and are widely used in medicine, including X-ray imaging and radiation therapy for cancer treatment. Other fields, such as nuclear power generation, also heavily rely on radiation. However, the growing range of radiation applications increases the risk of exposure to high-energy ionizing radiation (Asal & Erenturk, 2021). Ionizing radiation has been shown to cause permanent damage to both the human body and the environment, necessitating comprehensive preventive measures to mitigate these risks (Tekın at al., 2021). Radiation shielding materials must possess an adequate attenuation coefficient, strength, chemical stability, and temperature resistance (Alipoor & Eshghi, 2024, Hamad, 2023, Temir atal., 2021). Traditional radiation shields, such as lead and concrete, have limitations. Lead, despite its excellent attenuation properties, is unsuitable for long-term use in high-temperature environments due to its low melting point. Similarly, concrete suffers from damage such as cracking and flaking when exposed to radiation at high temperatures, which can impair its performance (Thiyagarajan at al., 2022, Han & Guo, 2017, Gu at al., 2022). As radiation shielding technology has evolved, various materials, including glasses, concretes, metal

Please cite this article as: Alipoor, M. & Eshghi, M. (2024). Gamma-ray Shielding Capacity of Ceramics Tb and Fe Doped with $Y_2Zr_2O_7$, *Advanced Ceramics Progress*, 10(1), 1-10. https://doi.org/10.30501/acp.2024.428521.1140

2423-7485/© 2024 The Author(s). Published by MERC.
This is an open access article under the CC BY license (https://creativecommons.org/licenses/by/4.0/).

composites, and ceramics, have been explored for their potential use in shielding applications (Magnere at al., 2024, Ratep at al., 2024, Saleh at al., 2024, Naeema at al., 2024). For instance, composites are valued for their tunable structural properties but are less desirable for handling radioactive materials due to their poor heat transfer capabilities (Mahmoud at al., 2024, Ghule, 2024). Ceramics are a promising class of radiation shielding materials due to their ease of fabrication, durability, non-toxicity, and high melting points. These materials typically consist of non-metallic compounds (e.g., metal oxides, nitrides, carbides) combined with metallic elements, resulting in a crystalline or semi-crystalline structure (Alver at al., 2023, Madej at al., 2021). Over the past decades, ceramics and ceramic composites have been utilized in industry and medicine. Their high temperature resistance (>1200°C), conductivity, hardness, insulation properties, strong oxidation resistance, low thermal expansion, and low dielectric constant make them effective at shielding against gamma rays (Lakshminarayana at al., 2018, Aktaş at al., 2019, Kaçal at al., 2018). Recent studies have focused on improving the production and design of ceramics, as well as adjusting their phase and composition, expanding their potential applications (Khattari at al., 2024, Oto at al., 2019, Hannachi at al., 2023, Alhindawy at al., 2023, Rao at al., 2023). Doped zirconium ceramics have garnered significant attention for their excellent radiation shielding properties. Zirconium, known for its high hardness, wear resistance, and corrosion resistance, can be enhanced with rare earth elements (REEs) such as cerium, ytterbium, neodymium, and gadolinium. These dopants can impart desirable properties such as increased strength, electrical conductivity, and, importantly, enhanced radiation attenuation. REE-doped zirconia improves protective abilities by enhancing microstructure and density, making it effective at absorbing harmful photons due to its high atomic number and density. Additionally, REE-doped zirconia can reduce secondary radiation by capturing scattered electrons produced during absorption (Bawazeer at al., 2023, Okafor at al., 2021, Pantulap at al., 2023). Nickel-cobalt-boron (Ni-Co-B) doped boron nitride ceramics show excellent gamma-ray attenuation properties across various current densities. Investigations into the radiation shielding properties of Dufric ceramics with carbon nanotubes (CNTs) have shown that while CNTs can affect the network structure and unit cell shrinkage, their addition impacts the results (Du at al., 2013). Adding $Y_2O_3$ to ceramics, due to its high molecular mass, can enhance shielding properties, particularly against charged radiation and photons. Additionally, $Y_2O_3$ has a high neutron interaction cross-section (Alrowaili at al., 2023b).

In practice, the versatility and high stability of oxides combined with zirconium and yttrium elements are exceptional. These ceramics are also promising hosts due to their ability to incorporate a wide variety of dopants into their structure (Khan at al., 2023, Chan at al., 2023). Additionally, this structure is highly flexible; for example, the lattice can accommodate ionic replacements at all its crystal sites, as well as vacancies, which can enhance structural defects (Yao at al., 2022).

Considering the increasing need for radiation protection in various industries such as medicine and nuclear energy, zirconium ceramics doped with yttrium and terbium make it a suitable option for radiation protection applications. Also, the addition of these two elements, Yttrium and Terbium, can increase the neutron shielding of doped Zirconium ceramics and make it a suitable shield for use in radiation protection applications. Therefore, the currently investigated zirconium-doped ceramics can become a safe (lead-free), transparent, and robust alternative with high temperature resistance for radiation protection and control in hospitals, industries, and other areas where radiation is applied.

## 2. MATERIALS AND METHODS

To ensure better understanding, a theoretical background of common formulas for gamma radiation protection is given below. Then, the Geant4 simulation tool is briefly described.

### 2.1. Theory

The linear attenuation coefficient (μ) measuring the attenuation capacity (absorption + scattering) of the material against photon radiation is obtained using Formula 1 (Alipoor & Eshghi, 2024):

$$\mu = \frac{ln\,(\frac{I_0}{I})}{x} \quad (1)$$

where the I and $I_0$ values are the photon intensities measured and x is the thickness of the irradiated material. The mass attenuation coefficient ($\mu_\rho$, $cm^2/g$) is obtained from relation 2 by dividing μ by the specific weight of the material :

$$\mu_m = \sum_{i=1} W_i\,(\frac{\mu}{\rho})_i \quad (2)$$

Half value of layer (HVL) and tenth value layer (TVL) are the thickness of the shield that reduced the half and the tenth of the incident radiation intensity, respectively, and these parameters can be calculated utilizing Equations 3 and 4 :

$$HVL(cm) = \frac{ln\,2}{\mu} = \frac{0.693}{\mu} \quad (3)$$

$$TVL(cm) = \frac{ln\,10}{\mu} = \frac{2.3026}{\mu} \quad (4)$$

The values of effective atomic number ($Z_{eff}$) and effective electron density ($N_{eff}$) of studied ceramics are determined by Equations 5 and 6 :

$$Z_{eff} = \frac{\sigma_a}{\sigma_e} \quad (5)$$

$$N_{eff}\left(electron/_{g}\right) = N_A \frac{nZ_{eff}}{A} = \frac{\mu_m}{\sigma_e} \quad (6)$$

The parameter $\Sigma_R$ (removal cross-section) parameter could be explained as possibility of a fast neutron being removed from a group of high energetic uncollided neutrons after the first collision with the any substance. The value $\Sigma_R$ for a multi-element material is calculated as follows (Alipoor & Eshghi, 2024):

$$\Sigma_R/\rho = \sum_i W_i \left(\Sigma_R/\rho\right) \quad (7)$$

### 2.2. Toolkit for the simulation Geant4

The mass attenuation coefficient for all ceramic samples was determined using the Geant4 Monte Carlo simulation, based on the geometry shown in Figure 1. Geant4 is an object-oriented simulation toolkit based on C++ and is widely used in various fields, including nuclear physics, medical physics, and high-energy physics. This simulation tool offers advanced options for defining elements, chemical compositions, and types of radiation (such as gamma rays and electrons) across a broad energy range, using a variety of comprehensive libraries.

Geant4 allows users to define materials (elements and compounds with different isotopes), create diverse detector geometries, generate particles and beams, and collect data on particle transport. The significance and validity of Geant4 simulations are discussed in references (Taheri at al., 2023). In this simulation, gamma photons were set with an energy spectrum ranging from 0.015 to 10 MeV. To achieve the desired outcome, several input files were created, including material, source, geometry, and detector information. The material was modeled as a blade with dimensions of 10×10×1 cm along the x, y, and z coordinates. Figure 1 shows a 3D view of the simulation, depicting a schematic representation of the narrow beam transmission geometry for gamma photons passing through the ceramic sample. In Figure 1, the green lines inside the blade represent the traces of gamma rays.

Photon attenuation was determined by simulating all possible physical processes affecting photons (such as photoelectric effects, Compton scattering, Rayleigh scattering, and pair production), as well as bremsstrahlung, ionization, and positron annihilation for electrons and positrons. These processes were simulated using physics models for electromagnetic processes available in G4EMStandardPhysics (options 1-4). These physics models are part of the Electromagnetics package, which utilizes evaluated data libraries to calculate time steps that model the interactions of photons and electrons with matter. To ensure accuracy, each simulation was performed with 10 million gamma photons and used option 4 of the electromagnetic physics models (Kelsey at al., 2023, Eshghi &Alipoor, 2024).

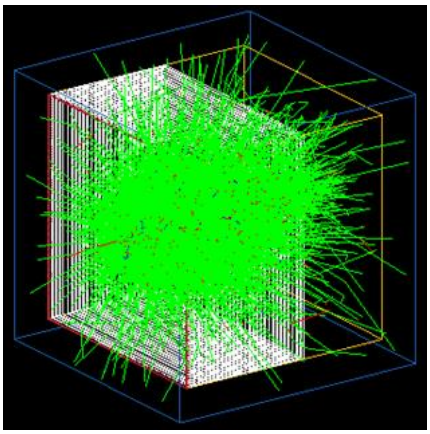

**Figure 1.** Schematic of configuration of shielding in Geant4 tool.

## 3. RESULTS AND DISCUSSION

In Table 1, five zirconium ceramics doped with Y and Fe are investigated for their gamma and neutron shielding properties (Jovaní at al., 2016).

**TABLE 1.** Chemical compounds of the selected ceramics.

| Material | Density | %Weight Fractions | | | | |
|---|---|---|---|---|---|---|
| | | Y | Zr | Fe | O | Tb |
| YF015 | 5.42 | 0.5216 | 0.2676 | 0.1638 | 0.0419 | -- |
| YF025 | 4.6 | 0.4225 | 0.2167 | 0.1327 | 0.2281 | -- |
| YF035 | 4.74 | 0.4225 | 0.1167 | 0.2327 | 0.2281 | -- |
| YTF015 | 6.71 | 0.2164 | 0.222 | 0.1359 | 0.0389 | 0.3868 |
| YTF025 | 5.8 | 0.1811 | 0.1858 | 0.1138 | 0.1956 | 0.3237 |
| YTF035 | 5.94 | 0.1811 | 0.0858 | 0.2138 | 0.1956 | 0.3237 |

First, we calculated the mass attenuation coefficients using the Geant4 tool. Medical radiation is a branch of medicine that uses radiation to diagnose conditions such as bone fractures or tumors, and to treat these conditions. Diagnostic medical radiation typically ranges from approximately 0.015 to 0.5 MeV, while therapeutic medical radiation ranges from approximately 0.5 to 15 MeV. To illustrate the differences in shielding requirements for these energy ranges, we investigated both diagnostic and therapeutic energy fields in this study.

Mass attenuation coefficients were determined for each ceramic sample across a range of energies from 0.015 MeV to 15 MeV. In the next step, the same ceramic compounds (as listed in Table 1) were defined, including their densities, in the Phy-X/PSD program. Overall, the results obtained from the two programs were in good agreement with each other.

**TABLE 2.** Mass attenuation coefficients in terms of photon energy for the ceramics.

| Energy (MeV) | YF015 | | YF025 | | YF035 | | YTF015 | | YTF025 | | YTF035 | |
|---|---|---|---|---|---|---|---|---|---|---|---|---|
| | our work | Phy-X | our work | Phy-X | our work | Phy-X | our work | Phy-X | our work | Phy-X | our work | Phy-X |
| **0.015** | 27.716 | 27.910 | 22.797 | 22.956 | 26.033 | 26.202 | 56.011 | 56.133 | 47.177 | 47.280 | 50.413 | 50.526 |
| **0.02** | 59.518 | 59.374 | 48.367 | 48.254 | 43.685 | 43.585 | 52.280 | 52.172 | 43.897 | 43.805 | 39.214 | 39.135 |
| **0.02634** | 28.616 | 28.665 | 23.266 | 23.307 | 20.945 | 20.968 | 25.122 | 25.136 | 21.103 | 21.115 | 18.782 | 18.776 |
| **0.04** | 9.248 | 9.206 | 7.539 | 7.506 | 6.756 | 6.730 | 8.150 | 8.154 | 6.863 | 6.866 | 6.080 | 6.090 |
| **0.0595** | 3.089 | 3.094 | 2.538 | 2.542 | 2.279 | 2.283 | 6.644 | 6.622 | 5.592 | 5.573 | 5.333 | 5.313 |
| **0.08** | 1.403 | 1.404 | 1.168 | 1.169 | 1.058 | 1.057 | 3.053 | 3.070 | 2.582 | 2.597 | 2.471 | 2.484 |
| **0.103** | 0.7416 | 0.743 | 0.6297 | 0.631 | 0.5751 | 0.577 | 1.598 | 1.600 | 1.363 | 1.364 | 1.308 | 1.309 |
| **0.15** | 0.3285 | 0.328 | 0.2917 | 0.291 | 0.2732 | 0.273 | 0.6428 | 0.639 | 0.5599 | 0.557 | 0.5414 | 0.539 |
| **0.284** | 0.1317 | 0.132 | 0.1273 | 0.128 | 0.1247 | 0.125 | 0.1863 | 0.187 | 0.1737 | 0.174 | 0.1710 | 0.172 |
| **0.364** | 0.1065 | 0.107 | 0.1051 | 0.105 | 0.1041 | 0.104 | 0.1343 | 0.135 | 0.1286 | 0.129 | 0.1275 | 0.128 |
| **0.4** | 0.0996 | 0.100 | 0.0989 | 0.099 | 0.0981 | 0.098 | 0.1213 | 0.121 | 0.1171 | 0.117 | 0.1163 | 0.116 |
| **0.511** | 0.0853 | 0.085 | 0.0856 | 0.085 | 0.0854 | 0.085 | 0.0964 | 0.096 | 0.0948 | 0.095 | 0.0946 | 0.094 |
| **0.662** | 0.0738 | 0.073 | 0.0745 | 0.074 | 0.0745 | 0.074 | 0.0791 | 0.079 | 0.0789 | 0.078 | 0.0789 | 0.078 |
| **0.723** | 0.0703 | 0.070 | 0.0711 | 0.071 | 0.0712 | 0.071 | 0.0745 | 0.074 | 0.0745 | 0.074 | 0.0746 | 0.074 |
| **0.826** | 0.0654 | 0.065 | 0.0664 | 0.066 | 0.0665 | 0.066 | 0.0682 | 0.068 | 0.0685 | 0.068 | 0.0687 | 0.068 |
| **1.1173** | 0.0542 | 0.054 | 0.0551 | 0.055 | 0.0553 | 0.055 | 0.0554 | 0.055 | 0.0556 | 0.055 | 0.0558 | 0.055 |
| **1.275** | 0.0519 | 0.051 | 0.0528 | 0.052 | 0.0531 | 0.053 | 0.0524 | 0.052 | 0.0531 | 0.053 | 0.0533 | 0.053 |
| **1.333** | 0.0507 | 0.050 | 0.0516 | 0.051 | 0.0517 | 0.051 | 0.0511 | 0.051 | 0.0518 | 0.052 | 0.052 | 0.052 |
| **1.5** | 0.0478 | 0.047 | 0.0485 | 0.048 | 0.0487 | 0.049 | 0.0481 | 0.048 | 0.0487 | 0.048 | 0.0489 | 0.049 |
| **2** | 0.0418 | 0.042 | 0.0423 | 0.042 | 0.0425 | 0.042 | 0.0423 | 0.042 | 0.0427 | 0.043 | 0.0428 | 0.043 |
| **3** | 0.0362 | 0.036 | 0.0361 | 0.036 | 0.0361 | 0.036 | 0.0373 | 0.037 | 0.0370 | 0.037 | 0.0370 | 0.037 |
| **4** | 0.0339 | 0.034 | 0.0334 | 0.033 | 0.0331 | 0.033 | 0.0355 | 0.036 | 0.0348 | 0.035 | 0.0346 | 0.035 |
| **5** | 0.0329 | 0.033 | 0.0319 | 0.032 | 0.0316 | 0.032 | 0.0351 | 0.035 | 0.0338 | 0.034 | 0.0336 | 0.034 |
| **6** | 0.0325 | 0.033 | 0.0312 | 0.031 | 0.0308 | 0.031 | 0.0352 | 0.035 | 0.0336 | 0.034 | 0.0334 | 0.033 |
| **8** | 0.0327 | 0.033 | 0.0308 | 0.031 | 0.0303 | 0.030 | 0.0361 | 0.036 | 0.0339 | 0.034 | 0.0335 | 0.034 |
| **10** | 0.0334 | 0.034 | 0.0310 | 0.031 | 0.0305 | 0.031 | 0.0374 | 0.038 | 0.0347 | 0.035 | 0.0342 | 0.034 |
| **15** | 0.0357 | 0.036 | 0.0324 | 0.033 | 0.03172 | 0.032 | 0.0407 | 0.041 | 0.0371 | 0.037 | 0.0364 | 0.037 |

However, many factors can affect the results of Monte Carlo simulations. Phy-X/PSD is a web-based tool that allows users to explore different shielding properties based on material definitions and energy ranges. Notably, the relative error between the outcomes of the two programs ranged from 0.84% to 0.09%. After verifying the compatibility of the simulation results, we calculated additional shielding parameters. The density and chemical composition of the manufactured ceramics are provided in Table 1. From this table, it is evident that the density of the ceramics increases with higher terbium concentration (Tb, Z=65), with the YTF015 sample showing the highest density value. According to Table 2, YTF015 exhibits the highest mass attenuation coefficients across the entire energy range, while YF025 shows the lowest coefficients.

From Figure 2, it was observed that there are peaks for the ceramics at photon energies of 17.03 and 17.99 keV. Since these photon energies fall within the region where the photoelectric absorption effect predominates, all ceramics exhibit the highest mass attenuation coefficients (μ) at these energies compared to other energy levels. These peaks correspond to the K-edge absorption of yttrium (at 17.0384 keV). As the energy increases, the probability of photoelectric absorption decreases, while the probability of Compton scattering increases. Consequently, the μ values decrease with increasing energy. Our findings clearly show that the YTF025 sample exhibits the highest values across all energies.

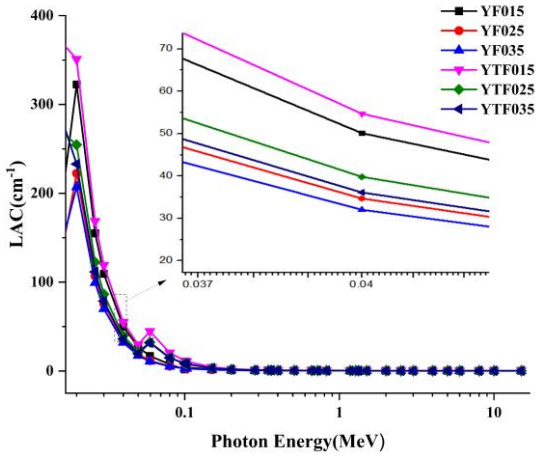


**Figure 2.** Linear attenuation coefficient ($cm^{-1}$) in terms of photon energy for ceramics.

It is important to note that the results were closely aligned due to variations in the incorporation of zirconium and terbium into the ceramics. However, the presence or absence of terbium had a substantial impact on the mass attenuation coefficients of the ceramics. Furthermore, as a density-independent parameter, the mass attenuation coefficient provides critical insights into the material's performance in relation to its elemental composition.

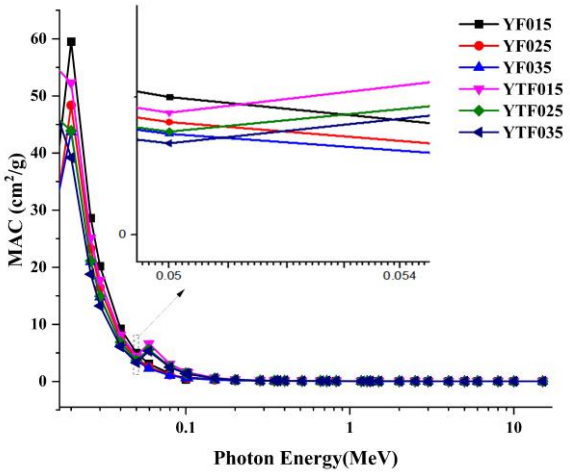


**Figure 3.** Mass attenuation coefficient($cm^2/g$) in terms of photon energy for ceramics.

Meanwhile**,** Figure 3 clearly depicts the onset of the K-edge absorption peak for yttrium in the ceramics, as shown in magnification. This figure illustrates the variation of mass attenuation coefficients ($\mu_m$) within the energy range from 0.15 to 15 MeV. Consistent with previous findings, the YTF015 sample exhibits the highest values. This observation can be partially attributed to the differing structural and atomic arrangements in YF015 and YTF015, which directly influence their gamma-ray attenuation properties.

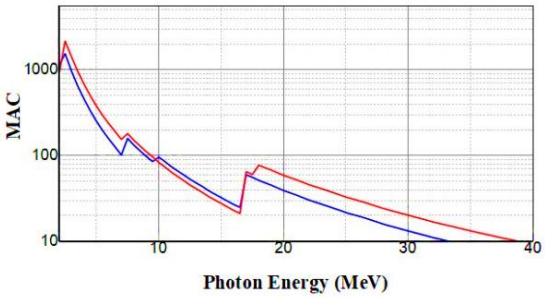


**Figure 4.** Mass attenuation coefficient ($cm^2/g$) in terms of photon energy for ceramics.

Figure 4 clearly illustrates the peaks associated with the photoelectric effect near the L2, L1, L3, and K edge absorptions of the yttrium element (at energies of 2.3725, 2.1555, 2.08, and 17.0384 keV, respectively), as well as the K edge absorption of the zirconium element (at an energy of 17.9976 keV). In addition, the L1 edge absorption of the terbium element is observed at 8.708 keV, extending up to 40 keV.

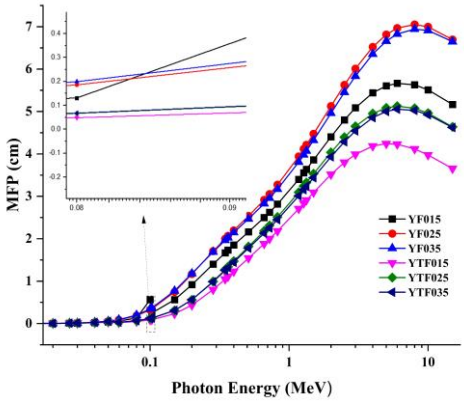


**Figure 5.** Mean free path(cm) in terms of photon energy for ceramics.

Another critical parameter for evaluating photon shielding characteristics is the mean free path (MFP), which represents the average distance a particle (photon, atom, or molecule) travels between two consecutive collisions. These collisions affect the particle's direction, energy, and other properties. The MFP is a crucial parameter that determines the effectiveness of radiation shielding. As depicted in Figure 5, the MFP is influenced by photon energy, with an increase in gamma photon energy leading to a longer MFP for the material. The changes in MFP are displayed over an energy range of 0.015 to 10 MeV. It is observed that, at lower energies below 1 MeV, the MFP increases slightly, while at energies above 1 MeV, the increase is more pronounced. Within the energy range of 0.1 to 1 MeV, the MFP increases almost uniformly. Notably, YF025 and YF035 exhibit higher MFP values compared to other materials, indicating that these materials interact less with photons and may not be ideal for shielding

applications. A significant increase in MFP is observed for the ceramic YF015 at an energy of 0.06 MeV (Figure 5).

The half-value layer (HVL) is another essential shielding parameter used to determine the specific thickness of an absorber required to reduce the photon intensity to 50% of its original value. A material with a lower HVL is generally more suitable for practical applications. Therefore, researchers aim to identify protective materials with relatively low HVL values. Figure 6 presents a graphical representation of the HVL data for the studied ceramics.

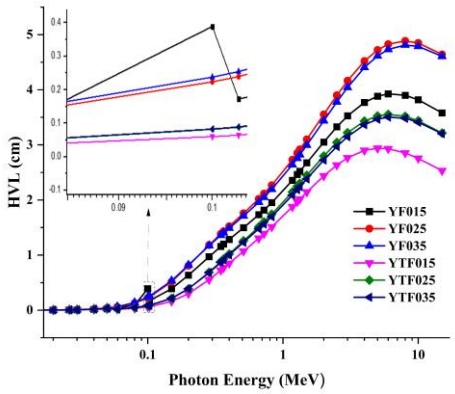


**Figure 6.** The half-value layer(cm) in terms of photon energy for ceramics.

The half-value layer (HVL) values exhibit a strong dependence on photon energy, increasing as the energy ranges from 0.1 to 10 MeV. The findings also indicate that HVL values are influenced by the composition and quantity of iron and terbium incorporated into the ceramics. Specifically, the results show that HVL is affected by the density of the material. Notably, the HVL for the YTF015 ceramic is lower compared to other ceramics. This observation suggests that an increase in the concentration of iron and terbium enhances the ability of the studied ceramics to attenuate photons.

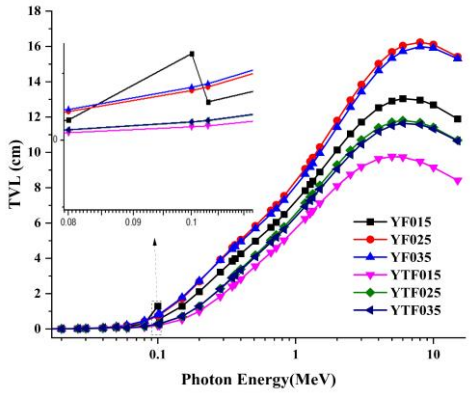


**Figure 7.** The tenth-value layer(cm) in terms of photon energy for ceramics.

In addition, another valuable parameter commonly used to estimate the attenuation effect of photons in various materials is illustrated in Figure 7. The tenth-value layers (TVLs) increase rapidly with energy, consistent with findings from studies analyzing TVL for the ceramics under investigation. In other words, the results for TVL closely match those for the half-value layer (HVL) reported previously. Our results indicate that the YTF015 sample, with the highest terbium (Tb) content, exhibits the lowest TVL values across all energy levels.

For instance, at an energy of 0.511 MeV, the TVL values for the samples were reported as 4.976 cm, 5.844 cm, 5.685 cm, 3.555 cm, 4.183 cm, and 4.095 cm for YF015, YF025, YF035, YTF015, YTF025, and YTF035, respectively. Both TVL and HVL values vary with increasing iron and terbium content and with the increasing density of the studied ceramics.

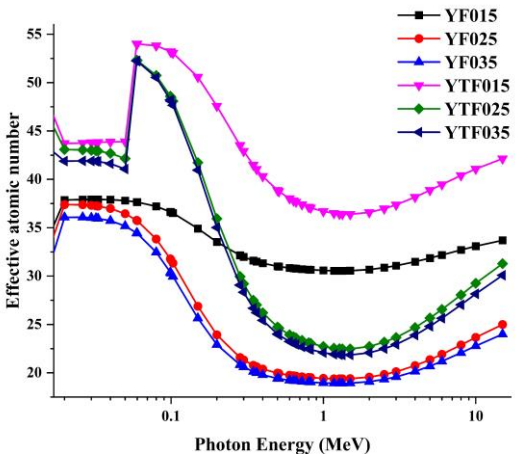


**Figure 8.** The effective atomic number, $Z_{eff}$, in terms of photon energy for ceramics.

The concept of effective atomic number ($Z_{eff}$) is employed to characterize the electromagnetic interaction of gamma ray photons with a compound. This parameter considers both the atomic composition and the density of the material. $Z_{eff}$ is defined as a calculated value representing the average atomic numbers of the constituent elements, adjusted for their respective electron densities. An increased $Z_{eff}$ value indicates a higher frequency of scattering interactions, thereby enhancing the material's effectiveness in scattering low-energy gamma rays. At higher energy levels, the significance of $Z_{eff}$ diminishes, with other factors, particularly the nuclear properties of the shielding materials and their role in pair production interactions, becoming more relevant. Thus, a thorough analysis of shielding material selection, considering gamma ray energy and specific interaction processes, is essential for optimizing shielding performance. Figure 8 illustrates the variations in $Z_{eff}$ values for the studied ceramics across different gamma ray energies. The YTF015

sample consistently exhibits the highest effective atomic number ($Z_{eff}$) values at all energy levels, which may be attributed to its superior gamma ray absorption capabilities.

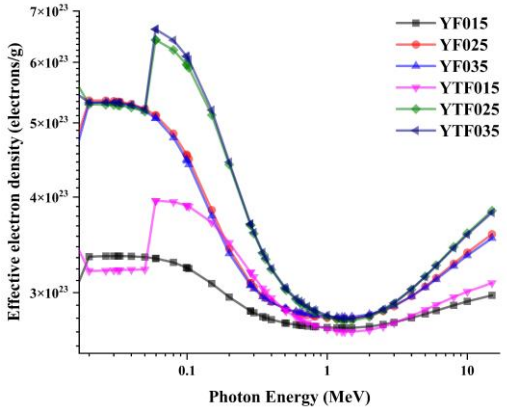


**Figure 9.** The effective electron density, $N_{eff}$, in terms of photon energy for ceramics.

Figure 9 displays the dependence of electron density, $N_{eff}$, values on photon energy across the range of 0.015 to 10 MeV for all samples. It is evident from the figure that fluctuations in $N_{eff}$ are significant, mirroring the trends observed for the effective atomic number $Z_{eff}$. These trends are also influenced by the average atomic mass (A), where Z represents the number of protons or electrons in each sample.

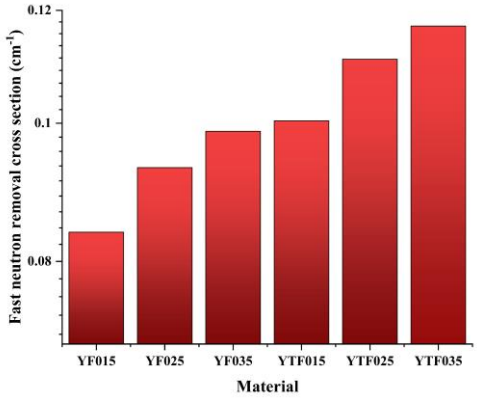


**Figure 10.** Fast neutron removal cross section ($cm^{-1}$) with photon energy for ceramics.

The effective fast neutron removal cross-section ($\Sigma_R$) is shown in Figure 10 for all samples using bar representation in units of $cm^{-1}$. The calculated $\Sigma_R$ for all studied ceramics shows that YTF035 has the highest value ($\Sigma_R$ = 0.117), indicating the fact that the effective removal cross-section of fast neutrons increases with decreasing zirconium percentage. On the contrary, the lowest calculated $\Sigma_R$ = 0.083 is for sample YF015 with the most zirconium. These related variations of $\Sigma_R$ with respect to physical and mechanical properties may suggest a way to design ceramic composites that can meet the engineering and shielding requirements of gamma and neutron radiation for specific applications. Depending on the shielding parameters considered, it may be possible to determine the best shielding parameter for a particular application.

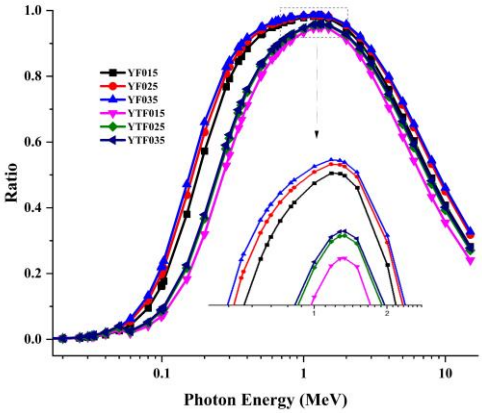


**Figure 11.** The $Ratios\ (\mu_m)_{Compton} / (\mu_m)_{total}$ with photon energy for ceramics.

Further, variation of ratios $(\mu_m)_{Compton} / (\mu_m)_{total}$ versus the energy photon (0.015–10 MeV) is presented for ceramics in Figure 11. The value of $(\mu_m)_{Compton}/(\mu_m)_{total}$ at ~1000 keV belongs to the maximum value of $(\mu_m)_{Compton} / (\mu_m)_{total}$. This figure clearly illustrates that as photon energy increases and Compton scattering becomes more dominant, the radiation absorption performance decreases. According to Figure 11, YTF015 ceramic exhibits favorable characteristics for radiation protection, demonstrating a lower absorption-to-scattering ratio compared to other samples.

- Buildup factors play a crucial role in the design of effective radiation shields. This study aimed to quantify the energy absorption exposure buildup factor (EBF) values for the ceramics under investigation, considering various mean free path parameters. Figures 10 and 11 demonstrate that the relative EBF values tend to be higher for stable nuclei under low-energy conditions. This observation suggests that stable nuclei are held together by strong forces, requiring significant energy input to destabilize them. Conversely, light nuclei may exhibit lower EBF values, yet they still indicate a bound state.
- At intermediate energy levels, EBF values can remain significantly high, although they are more sensitive to the specific reaction mechanisms involved. Certain reactions may have increased likelihoods and enhanced energetic favorability, leading to alterations in nuclear characteristics. This variability explains why the photoelectric effect and transitions are prominent in low and high-energy regions. In these processes, photons are either fully

absorbed or significantly reduced, resulting in less accumulation.

- At moderate energies, Compton scattering predominates, causing photons to scatter rather than being completely absorbed. This scattering also leads to multiple photon interactions, which affects the EBF. As the proportion of zirconium (Zr) decreases, energy absorption in YF ceramics diminishes, particularly noticeable in the 50 to 100 keV energy range. Moreover, a decrease in the percentage of terbium (Tb) leads to a reduction in energy absorption in YFT ceramics. This effect is particularly noticeable at energies below 100 keV.

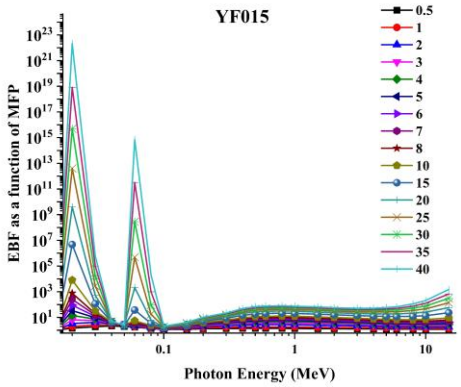


**Figure 12-a.** Variation of exposure buildup factor (EBF) with photon energy at different mean free paths for ceramics.

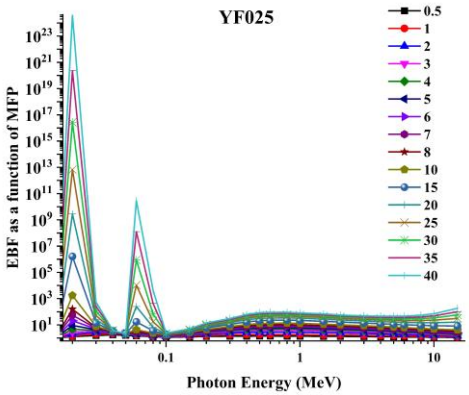


**Figure 12-b.** Variation of exposure buildup factor (EBF) with photon energy at different mean free paths for ceramics.

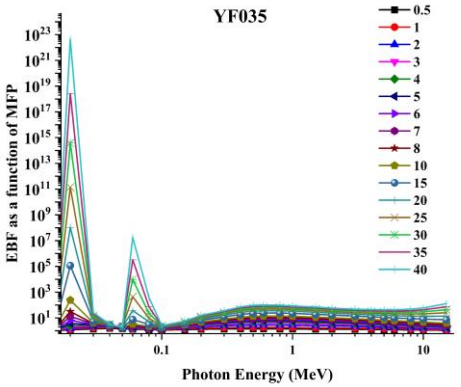


**Figure 12-c.** Variation of exposure buildup factor (EBF) with photon energy at different mean free paths for ceramics.

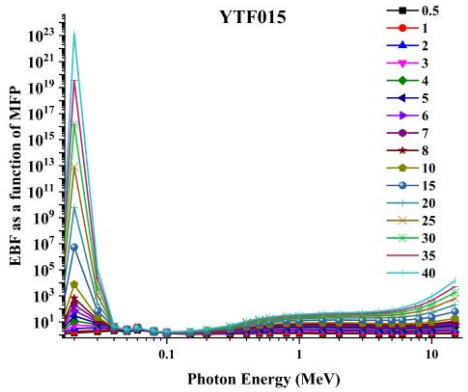


**Figure 12-d.** Variation of exposure buildup factor (EBF) with photon energy at different mean free paths for ceramics.

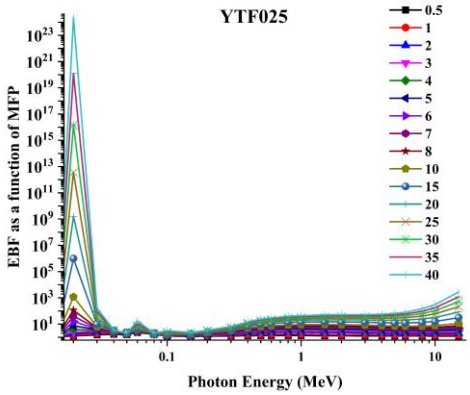


**Figure 12-e.** Variation of exposure buildup factor (EBF) with photon energy at different mean free paths for ceramics.

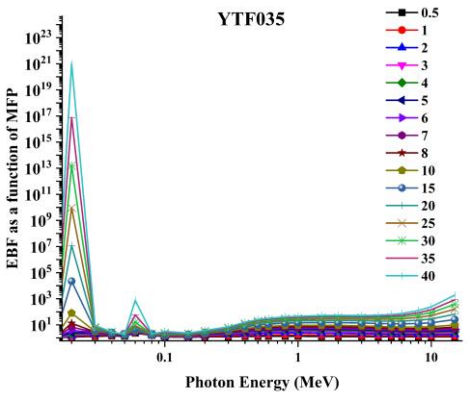


**Figure 12-f.** Variation of exposure buildup factor (EBF) with photon energy at different mean free paths for ceramics.

## 4. CONCLUSION

In this study, we examined the shielding properties of ceramics against ionizing radiation, including linear attenuation coefficient, mass attenuation coefficient, half-value layer, tenth-value layer, and mean free path (MFP) across a photon energy range of 0.015 to 15 MeV, using the Geant4 and Phy-X programs, which produced consistent results. The findings indicated that the YTF015 ceramic, enhanced with terbium, showed notable improvements in densification, microstructural development, and flexural strength, leading to increased protection against fast neutron and gamma radiation. The study also demonstrated that energy levels significantly impact gamma ray penetration, with YTF015 exhibiting strong shielding performance at 0.511 MeV, where the mass attenuation coefficient dropped from 0.58 to 0.096 cm. Compared to pure lead, YTF015 ceramics offered effective shielding, achieving 35% to 55% of pure lead's shielding capacity in the 0.1 to 2 MeV energy range, highlighting the potential of ceramic materials' composition and microstructure in optimizing attenuation properties for medical physics applications.

## ACKNOWLEDGEMENTS

Thanks to the dear referees who helped improve the quality of the article. Also, we appreciate and thank all the magazine officials for the good editing of the proof of the article.

## REFERENCES

1. Aktas, B., Yalcin, S., Dogru, K., Uzunoglu, Z., & Yilmaz, D. (2018). Structural and radiation shielding properties of chromium oxide doped borosilicate glass. *Radiation Physics and Chemistry*, 156, 144–149. https://doi.org/10.1016/j.radphyschem.2018.11.012
2. Alipoor, M. R., & Eshghi, M. (2024). Nickel/Multiwalled carbon nanotube composites as Gamma-Ray shielding. *NANO*, 19(06). https://doi.org/10.1142/s1793292024500279
3. Alipoor, M., & Eshghi, M. (2024). Monte Carlo simulation and determination of gamma ray protection characteristics of composites containing Bismuth Oxide and elements of Gadolinium, Titanium, Tungsten, Zirconium, Zinc and Yttrium. *Journal of Science and Technology of Composites*, 10(4), 2348-2356. https://doi.org/10.22068/jstc.2024.2007267.1845
4. Alipoor, M., & Eshghi, M. (2024). Shielding properties of iron-doped nano-hydroxides against gamma-rays. *Journal of Nuclear Science, Engineering and Technology (JONSAT)*, 45(4). https://doi.org/10.24200/nst.2024.1643
5. Alhindawy, I. G., Sayyed, M., Aloraini, D. A., Almuqrin, A. H., Alomar, M. S., Elawadi, G. A., & Mahmoud, K. (2024). A multi-phase investigation to understand the function of lanthanum and neodymium in the zirconia ceramics' synthesis, structural, and gamma-ray protective ability. *Radiation Physics and Chemistry*, 215, 111336. https://doi.org/10.1016/j.radphyschem.2023.111336
6. Alrowaili, Z., Kırkbınar, M., İbrahimoğlu, E., Çalışkan, F., Alruwaili, N. S., Elhadi, M., Al-Buriahi. (2023b). Radiation shielding performance of recycled waste CRT glasses doped with $Li_2O$ and $Y_2O_3$: Potential applications in medical facilitates. *Radiation Physics and Chemistry*, 212, 111200. https://doi.org/10.1016/j.radphyschem.2023.111200
7. Alver, Ü., Duran, S. U., Demirköz, M., Muçogllava, B., Aslan, M., Çava, K., Dindar, O. (2023). Ulexite/HDPE-Bi2O3/HDPE layered composites for neutron and gamma radiation shielding. *Applied Radiation and Isotopes*, 200, 110940. https://doi.org/10.1016/j.apradiso.2023.110940
8. Asal, S., Erenturk, S. A., & Haciyakupoglu, S. (2020). Bentonite based ceramic materials from a perspective of gamma-ray shielding: Preparation, characterization and performance evaluation. *Nuclear Engineering and Technology*, 53(5), 1634–1641. https://doi.org/10.1016/j.net.2020.11.009
9. Bawazeer, O., Makkawi, K., Aga, Z. B., Albakri, H., Assiri, N., Althagafy, K., & Ajlouni, A. (2023). A review on using nanocomposites as shielding materials against ionizing radiation. *Journal of Umm Al-Qura University for Applied Sciences*, 9(3), 325–340. https://doi.org/10.1007/s43994-023-00042-9
10. Chen, Y., Zhang, R., Hu, S., Jiang, P., Sun, J., Zhang, B., & Zhang, Y. (2022). Mechanical properties of (ZrYTaErTi)O composites. *Ceramics International*, 49(3), 5261–5268. https://doi.org/10.1016/j.ceramint.2022.10.044
11. Du, Q., Zhou, G., Zhou, J., Jia, X., & Zhou, H. (2012). Enhanced luminescence of novel $Y_2Zr_2O_7:Dy^{3+}$ phosphors by $Li_+$ co-doping. *Journal of Alloys and Compounds*, 552, 152–156. https://doi.org/10.1016/j.jallcom.2012.10.074
12. Eshghi, M., & Alipoor, M. (2024). A Comprehensive Study of Gamma-rays Shielding Features of Binary Compounds. *Progress in Physics of Applied Materials*, 4(1), 59-67. https://doi.org/10.22075/ppam.2024.32949.1082
13. Ghule, P. G., Bholane, G., Joshi, R., Dahiwale, S., Shelke, P., & Dhole, S. (2023). Gamma radiation shielding properties of unsaturated polyester /$Bi_2O_3$ composites: An experimental, theoretical and simulation approach. *Radiation Physics and Chemistry*, 216, 111452. https://doi.org/10.1016/j.radphyschem.2023.111452
14. Gu, Y., Wang, J., Wang, Y., Xu, C., Liu, Y., Du, L., Liu, Q. (2022). Low-dose ionizing radiation exposure and risk of leukemia: results from 1950–1995 Chinese medical X-ray workers' cohort study and meta-analysis. *Journal of the National Cancer Center*, 2(2), 90–97. https://doi.org/10.1016/j.jncc.2022.01.001
15. Hamad, M. K. (2023). Effects of bismuth substitution on the structural and ionizing radiation shielding properties of the novel BaSnBiO perovskites: An experimental study. *Materials Chemistry and Physics*, 308, 128254. https://doi.org/10.1016/j.matchemphys.2023.128254
16. Han, J., & Guo, G. (2017). Characteristics of energy deposition from 1-1000 MeV proton and neutron induced nuclear reactions in silicon. *AIP Advances*, 7(11). https://doi.org/10.1063/1.4995529
17. Hannachi, E., Sayyed, M., Slimani, Y., Almessiere, M., Baykal, A., & Elsafi, M. (2023). Experimental study on the radiation protecting ability of composites containing barium titanate and nanospinel ferrite. *Radiation Physics and Chemistry*, 212, 111126. https://doi.org/10.1016/j.radphyschem.2023.111126
18. Jovaní, M., Sanz, A., Beltrán-Mir, H., & Cordoncillo, E. (2016). New red-shade environmental-friendly multifunctional pigment based on Tb and Fe doped $Y_2Zr_2O_7$ for ceramic applications and cool roof coatings. *Dyes and Pigments*, 133, 33–40. https://doi.org/10.1016/j.dyepig.2016.05.042
19. Kacal, M. R., Akman, F., & Sayyed, M. I. (2018). Investigation of radiation shielding properties for some ceramics. *Radiochimica Acta*, 107(2), 179–191. https://doi.org/10.1515/ract-2018-3030

20. Kelsey, M., Agnese, R., Alam, Y., Langroudy, I. A., Azadbakht, E., Brandt, D., Zatschler, S. (2023). G4CMP: Condensed matter physics simulation using the Geant4 toolkit. *Nuclear Instruments and Methods in Physics Research Section a Accelerators Spectrometers Detectors and Associated Equipment*, 1055, 168473. https://doi.org/10.1016/j.nima.2023.168473

21. Khan, M. Z., Gul, I. H., Javaid, F., Ali, A., Hafeez, S., & Baig, M. M. (2023). Synthesis and characterization of $Zr^{4+}$-$Y^{3+}$ substituted BA-SR hexaferrite nanoparticles for microwave absorption and electromagnetic shielding applications. *Materials Research Bulletin*, 168, 112468. https://doi.org/10.1016/j.materresbull.2023.112468

22. Khattari, Z. Y., Zakaly, H. M. H., Alrowaily, A. W., Ene, A., Shams, M. S., Issa, S. a. M., Rammah, Y. S. (2023). A comprehensive study on optical, physical, mechanical and radiation shielding properties of calcium bismuth borophosphate glass–ceramics with distinct $V_2O_5$ contents. *Optical and Quantum Electronics*, 56(1). https://doi.org/10.1007/s11082-023-05598-8

23. Lakshminarayana, G., Baki, S., Sayyed, M., Dong, M., Lira, A., Noor, A., Mahdi, M. (2017). Vibrational, thermal features, and photon attenuation coefficients evaluation for $TeO_2$-$B_2O_3$-BaO-ZnO-$Na_2O$-$Er_2O_3$-$Pr_6O_{11}$ glasses as gamma-rays shielding materials. *Journal of Non-Crystalline Solids*, 481, 568–578. https://doi.org/10.1016/j.jnoncrysol.2017.11.049

24. Madej, D., Silarski, M., & Parzych, S. (2020). Design, structure, microstructure and gamma radiation shielding properties of refractory concrete materials containing Ba- and Sr-doped cements. *Materials Chemistry and Physics*, 260, 124095. https://doi.org/10.1016/j.matchemphys.2020.124095

25. Magnere, S. M., Toledo, E. A., Yazdani-Pedram, M., Fuentealba, P., Contreras-Soto, A., Bascuñan-Heredia, A., Aguilar-Bolados, H. (2024). High performance fluoroelastomer composites filled with graphite and/or bismuth oxide for applications in gamma-ray shielding. *Polymer Composites*. https://doi.org/10.1002/pc.28237

26. Mahmoud, K., Binmujlli, M., Marashdeh, M., Sayyed, M., Aljaafreh, M. J., Akhdar, H., & Alhindawy, I. G. (2024). Comprehensive analysis of the effects of Mo and Co on the synthesis, structural, and radiation-shielding properties of $TiO_2$ based composites. *Progress in Nuclear Energy*, 169, 105105. https://doi.org/10.1016/j.pnucene.2024.105105

27. Naeema, N., Kadhim, O. J., Abdullah, N. J., Aldhuhaibat, M. J., Bakhtiar, H., & Salim, A. (2024). Shielding performance of metal oxide nanoparticles-doped polypropylene composites against gamma rays and neutrons exposure. *Radiation Physics and Chemistry*, 216, 111461. https://doi.org/10.1016/j.radphyschem.2023.111461

28. Okafor, C. E., Okonkwo, U. C., & Okokpujie, I. P. (2021). Trends in reinforced composite design for ionizing radiation shielding applications: a review. *Journal of Materials Science*, 56(20), 11631–11655. https://doi.org/10.1007/s10853-021-06037-3

29. Oto, B., Kavaz, E., Durak, H., Aras, A., & Madak, Z. (2019). Effect of addition of molybdenum on photon and fast neutron radiation shielding properties in ceramics. *Ceramics International*, 45(17), 23681–23689. https://doi.org/10.1016/j.ceramint.2019.08.082

30. Pantulap, U., Arango-Ospina, M., & Boccaccini, A. R. (2021). Bioactive glasses incorporating less-common ions to improve biological and physical properties. *Journal of Materials Science Materials in Medicine*, 33(1). https://doi.org/10.1007/s10856-021-06626-3

31. Rao, L. S., Hussain, S., Navalika, A., & Hila, F. C. (2024). Morphology, structural, and radiation shielding characteristics of $Bi_2O_3$-$B_2O_3$-$Cr_2O_3$: $ZrO_2$ glass ceramics. *Ceramics International*, 50(6), 9811–9819. https://doi.org/10.1016/j.ceramint.2023.12.302

32. Ratep, A., Abdelaziem, A., Hanfi, M. Y., Mahmoud, K. A., & Kashif, I. (2023). Enhancing gamma-ray shielding with bismuth oxide-infused boron oxides. *Optical and Quantum Electronics*, 56(2). https://doi.org/10.1007/s11082-023-05788-4

33. Saleh, A., Almohiy, H., Shalaby, R. M., & Saad, M. (2023). Comprehensive investigation on physical, structural, mechanical and nuclear shielding features against X/gamma-rays, neutron, proton and alpha particles of various binary alloys. *Radiation Physics and Chemistry*, 216, 111443. https://doi.org/10.1016/j.radphyschem.2023.111443

34. Taheri, A., Khandaker, M. U., Moradi, F., & Bradley, D. A. (2023). A review of recent advances in the modeling of nanoparticle radiosensitization with the Geant4-DNA toolkit. *Radiation Physics and Chemistry*, 212, 111146. https://doi.org/10.1016/j.radphyschem.2023.111146

35. Tekin, H. O., Bilal, G., Zakaly, H. M. H., Kilic, G., Issa, S. a. M., Ahmed, E. M., & Ene, A. (2021). Newly developed Vanadium-Based glasses and their potential for nuclear radiation shielding aims: A Monte Carlo Study on gamma ray attenuation parameters. *Materials*, 14(14), 3897. https://doi.org/10.3390/ma14143897

36. Temir, A., Zhumadilov, K., Zdorovets, M., Kozlovskiy, A., & Trukhanov, A. (2021). Study of gamma radiation shielding efficiency with radiation-resistant $Bi_2O_3$-$TeO_2$-$WO_3$ ceramics. *Solid State Sciences*, 115, 106604. https://doi.org/10.1016/j.solidstatesciences.2021.106604

37. Thiyagarajan, G. B., Koroleva, E., Filimonov, A., Vakhrushev, S., & Kumar, R. (2021). Thermally tunable dielectric performance of t-$ZrO_2$ stabilized amorphous Si(Pb,Zr)OC ceramic nanocomposites. *Materials Chemistry and Physics*, 277, 125495. https://doi.org/10.1016/j.matchemphys.2021.125495

38. Yao, Y., Ren, G., Yu, Y., Che, J., Liang, T., Li, L., . . . Zhao, X. (2022). Thermal conduction mechanism of ferroelastic Zr-Y-Yb-Ta-Nb-O high-entropy oxides with glass-like thermal conductivity. Journal of the American Ceramic Society, 105(6), 4360–4374. https://doi.org/10.1111/jace.18374

Advanced Ceramics Progress: Vol. 10, No. 1, (Winter 2024) 11-17

Materials and Energy Research Center
MERC

Contents lists available at ACERP

Advanced Ceramics Progress

Journal Homepage: www.acerp.ir

**Original Research Article**

# The Effect of Electrospinning Parameters on the Final Structure of the Electrospun PCL Fibers

Sepehr Afsharian [a], Seyede Fateme Mousavi Nasab [b], Neda Sami [b], Sahar Mollazadeh Beidokhti [c,*], Abbas Yousefi [d]

[a] *BSc degree, Department of Materials Engineering, Faculty of Engineering, Ferdowsi University of Mashhad, Iran.*
[b] *MSc student, Department of Materials Engineering, Faculty of Engineering, Ferdowsi University of Mashhad, Iran.*
[c] *Assistant Professor, Department of Materials Engineering, Faculty of Engineering, Ferdowsi University of Mashhad, Iran.*
[d] *Professor, Research Institute Paretavous, Mashhad, Iran.*

* Corresponding Author Email: molazadeh.b@um.ac.ir (S. Mollazadeh Beidokhti) URL: https://www.acerp.ir/article_207848.html

*ARTICLE INFO*

*Article History:*
Received: 15 April 2024
Revised: 06 May 2024
Accepted: 07 September 2024

*Keywords*:
*Poly-caprolactone (PCL),*
*Electro Spinning,*
*Wound Dressing,*
*Tissue Engineering*

*ABSTRACT*

In the last decade, regenerating damaged tissues has been a primary focus in tissue engineering research. An ideal wound dressing can be produced from synthetic polymers, such as polycaprolactone (PCL), via electrospinning. The processing variables significantly affect fiber morphology and characteristics, including fiber size and porosity. These factors directly influence the properties of wound dressings. This study investigated how the electrospinning process variables—specifically needle-to-plate distance, flow rate, and applied voltage—affect the diameter and morphology of nanofibers. By adjusting these parameters, researchers can optimize the performance of this technique and enhance the properties of the resulting fibers. Initially, PCL solutions with varying compositions and concentrations were prepared. The results indicated that increasing the voltage from 12 kV to 16 kV across three samples resulted in a decrease in the nanofiber diameter from 205.28 ± 50 nm to 175.74 ± 41 nm. Conversely, changing the flow rate from 0.4 to 0.6 ml/h in two samples increased the average fiber diameter from 210.66 ± 43 nm to 223.18 ± 44 nm. Additionally, increasing the needle-to-plate distance also led to a reduction in fiber diameter. Scanning electron microscopy (SEM) images revealed that interconnected, thin, bead-free nanofibers could be achieved at high voltages, low flow rates, and longer distances. However, at voltages above 18 kV and distances greater than 18 cm, bead formation in the nanofiber structure became inevitable. Furthermore, the polymer solution containing a certain amount of salt exhibited high conductivity, which resulted in fiber breakage.

https://doi.org/10.30501/acp.2024.448334.1150

## 1. INTRODUCTION

Tissue engineering represents a novel therapeutic approach for regenerating damaged tissues in living organisms (Siddiqui et al., 2021). This advanced field aims to develop innovative regeneration treatments by repairing and restoring various types of tissues, including skin, tendons, bone, cartilage, nerve tissue, maxillofacial tissue, and blood vessels. By combining cells, biomaterials, and biochemical factors, tissue engineering significantly enhances the quality of life for patients (Azimi et al., 2014; Ghaffarian et al., 2015; Siddiqui et al., 2021). Skin replacement stands out as one of the earliest successful applications of tissue regeneration,

Please cite this article as: Afsharian, S., Mousavi Nasab, S. F., Sami, N., Mollazadeh Beidokhti, S. & Yousefi, A. (2024). The Effect of Electrospinning Parameters on the Final Structure of the Electrospun PCL Fibers, *Advanced Ceramics Progress*, 10(1), 11-17. https://doi.org/10.30501/acp.2024.448334.1150

2423-7485/© 2024 The Author(s). Published by MERC.
This is an open access article under the CC BY license (https://creativecommons.org/licenses/by/4.0/).

enabling the regrowth of damaged skin (Moniri Javadhesari, 2022).

The skin serves a crucial role in protecting the body from bacteria and regulating its physiological functions. Sudden contact with hard and rough foreign objects can damage the skin, necessitating immediate tissue regeneration to prevent pathogenic factors and adverse effects (Joseph et al., 2019). In cases where wound healing is compromised or conventional therapeutic methods are ineffective, appropriate skin substitutes must be available. These healing procedures aim to improve wounds either temporarily or permanently (Dias et al., 2018; Vyas & Vasconez, 2014). Alternative wound dressings, characterized by specific properties, are designed to accelerate the healing process by conforming to the wound's shape and maintaining a moist interface. Additionally, these dressings should absorb exudate without supporting bacterial growth and prevent bleeding and fluid leakage. Furthermore, they must protect the wound and surrounding tissues, promote healing, and be easy to remove with minimal trauma to the injury injury (Dias et al., 2017; Dickinson & Gerecht, 2016; Dong et al., 2020; Ferreira et al., 2021; Vig et al., 2017; Wang et al., 2011).

Recent investigations have explored both synthetic and natural polymers as functional skin substitutes (Dwivedi et al., 2019). These polymers can perform a variety of skin functions and are often in direct contact with cells and tissues (Joseph et al., 2019). Key advantages of polymer biomaterials include biocompatibility, suitable mechanical and physical properties, and good processability (Liu et al., 2012). Biodegradable polymers have gained significant attention for medical applications due to their rapid degradation rates (Dong et al., 2020).

A prominent class of biodegradable polymers includes polyesters such as polycaprolactone (PCL), polyglycolic acid (PGA), and polylactic acid (PLA). PCL, in particular, is a biocompatible polymer that has garnered extensive interest in tissue engineering (Joseph et al., 2019). With a melting point higher than normal body temperature (59–64 °C) and a glass transition temperature below 60 °C, PCL exhibits notable mechanical properties, including high toughness, at physiological conditions. As a non-toxic and tissue-compatible material, PCL is utilized in absorbable sutures, scaffolds, and drug delivery systems. However, its degradation under physiological conditions is relatively slow, occurring over a period of 2–3 years (Abrisham et al., 2020; Dwivedi et al., 2019; Gil-Castell et al., 2019; Linh et al., 2022; Loh & Choong 2013; Stratton et al. 2016).

Numerous techniques have been established for synthetic polymer scaffolds, with novel nanotechnology methods continually emerging. Among these, electrospinning is one of the most widely used techniques for producing wound dressings and scaffolds (Elkhouly et al., 2021). Compared to standard bandages, electrospun wound dressings exhibit unique characteristics, such as enhanced bleeding control, increased wound fluid absorption, and improved adaptability to the wound (Dias et al., 2017).

Electrospinning creates nano- or microfibers by applying electrostatic forces. By reducing fiber diameter from micrometers to nanometers, this technique results in a high surface-to-mass ratio, flexibility in surface functionalities, and superior mechanical performance (Abdollahi, & Bakhsheshi-Rad, 2018). Electrospun fibers are typically collected randomly, yielding a high surface area (Joseph et al., 2019; Yang et al., 2017). The process requires an upper voltage source, a collector plate, and a syringe pump. Initially, high voltage is applied to a syringe containing the polymer solution, held by surface tension at its tip. The electrical field generates mutual charge repulsion that counters the surface tension, leading to jet formation (Ginestra et al., 2016). Figure 1 illustrates the electrospinning process.

As the solvent evaporates, the fibers are deposited onto the collector plate after jet formation. The resulting fibers can exhibit a range of morphologies and pore structures, influenced by various parameters, including solution viscosity, conductivity, and process variables like applied voltage (Joseph et al., 2019). Therefore, precise control of these factors is essential for obtaining fibers with desirable morphological and biological characteristics.

Electrospinning enables the production of interconnected nanofibers, resembling the structure of the extracellular matrix (Elkhouly et al., 2021; Gil-Castell et al., 2019; Jun et al., 2018). This similarity enhances cellular function. Electrospun PCL layers can be employed as cell-free wound dressings or as cell-assisted skin substitutes. Significant research has focused on how different variables affect the morphology of electrospun PCL fibers. Consequently, researchers have developed predictive models for determining the final diameter of these fibers, as suggested in Equation 1 (Baji et al., 2010)

$$D = \left[ \gamma\varepsilon \frac{Q^2}{I^2} \left( \frac{2}{\pi \left( 2 \left( ln \frac{l}{d} - 3 \right) \right)} \right) \right]^{\frac{1}{3}} \quad (1)$$

where ε is the dielectric constant, Q is the flow rate, I is the applied current, l is the initial length of the jet, and d is the needle diameter. A common morphology reported by several researchers is a combination of fibers and beads. Yet, the reason for bead formation is unknown. According to the results, the main factors controlling this behavior are the solution's viscoelasticity and surface tension.

Beachley et al. investigated the impact of various processing parameters on the morphology of polycaprolactone (PCL) fibers (Beachley & Wen, 2008).

Applied voltage plays a crucial role in determining fiber structure; as voltage increases, both fiber length and diameter tend to decrease due to heightened tension on the surface of the electrospinning jet. This finding contrasts with the study by Dustgani, which indicated that higher voltage could result in increased solution injection from the syringe, subsequently leading to larger fiber diameters (Doustgani, 2015). Moreover, elevated voltage has been observed to influence fiber morphology by reforming Taylor Cone jets and facilitating bead formation within the electrospun fibers (Chinnappan et al., 2022). Conversely, another study reported that a decrease in voltage could also lead to bead formation (Jarusuwannapoom et al., 2004).

The concentration of the polymer solution is another critical factor affecting fiber spinning ability. Insufficient polymer concentrations often result in the breakdown of electrospun fibers, preventing proper formation. Conversely, an increase in polymer concentration typically leads to an increase in fiber diameter (Chinnappan et al., 2022; Liverani & Boccaccini, 2016). Additionally, the incorporation of ionic salts, such as NaCl and $KH_2PO_4$, can enhance the electrical conductivity of polymer solutions, resulting in the formation of nanofibers with smaller diameters (Chinnappan et al., 2022).

Flow rate is a vital parameter as well, as it influences the properties of the newly synthesized polymer solution passing through the syringe. A high flow rate tends to produce fibers that contain beads and exhibit larger diameters. Furthermore, adjusting the needle-to-plate distance can significantly alter fiber structure; shorter distances can prevent fibers from solidifying before collection, while excessively long distances may induce bead formation (Baji et al., 2010; Ginestra et al., 2016; Liverani & Boccaccini, 2016).

This study aims to explore the effects of various processing parameters on the morphology of electrospun PCL fibers. As highlighted, the electrospinning process is significantly influenced by these variables, which ultimately affect the chemical composition, fiber size, porosity, and overall morphological characteristics essential for scaffold performance in tissue engineering. By examining these attributes, researchers can enhance the efficacy of the electrospinning technique. Therefore, this study investigates how different variables impact the morphology of electrospun fibers and seeks to identify optimal parameters for producing the most desirable fiber characteristic.

## 2. MATERIALS AND METHODS

### 2. 1. Materials

This study utilized polycaprolactone (PCL) sourced from the Solar Bio brand, characterized by an average molecular weight of 80,000 g/mol, as a natural biopolymer. To enhance the conductivity of the polymer solution and prevent blockage in the syringe, dichloromethane (DCM) and dimethylformamide (DMF) were employed as solvents. DCM, with a concentration exceeding 99% and a molecular weight of 84.3 g/mol, and DMF, of Extra Pure Grade with a concentration greater than 99.5% and a molecular weight of 73.09 g/mol (DrMojallali brand), were both selected for their efficacy in improving solution performance.

### 2.2. Preparation of Solution

Three types of polymer solutions with varying concentrations and compositions were prepared. Solution (1) was created by dissolving 1 g of polycaprolactone (PCL) in 8 ml of dichloromethane (DCM) and 1 ml of dimethylformamide (DMF). Solution (2) comprised 1.5 g of PCL in 8 ml of DCM and 1 ml of DMF. Solution (3) was identical to Solution (2), but included an additional 0.01 g of lithium chloride (LiCl). Initially, DMF and DCM were mixed, after which PCL was incorporated into the solution. The resulting polymer mixture was stirred for 12 hours to ensure complete dissolution.

### 2.3. Electrospinning

For this study, the ES1000 device from Nanoscale Technologies was utilized. The PCL solution was placed in a 5 ml syringe fitted with a 22-gauge needle. The solution flow rate was adjusted between 0.1 and 0.3 ml/h. Upon applying voltage, a fluid jet was ejected from the needle. Each experiment lasted for 5 minutes per sample, after which the samples were analyzed using a Scanning Electron Microscope (SEM). Experiments were conducted under various conditions to examine the effects of several variables on the morphology of the PCL fibers. Specifically, the influence of applied voltage, needle-to-plate distance, flow rate, and the presence of salt in the polymer solution was investigated. The distance was measured from the tip of the needle to the top of the collecting plate. Table 1 summarizes the parameters used for each sample.

### 2.4. Morphological examination

The results were evaluated to assess how variations in processing parameters affect the diameter and morphology of the nanofibers. For this purpose, Scanning Electron Microscopy (SEM) images were analyzed to measure the diameter of both the fibers and beads. The average diameter of 50 fibers and the maximum average diameter of 45 beads were calculated using ImageJ software.

## 3. RESULTS

### 3.1. Applied Voltage

The applied voltage is a critical parameter influencing the morphology and diameter of the fibers. Generally, a voltage exceeding 6 kV is necessary to generate polymer solution jets from Taylor cones (Ifegwu & Anyakora, 2018). Figure 2 displays the SEM images of samples S6, S7, and S8, which were subjected to different voltages while maintaining the same solution. The needle-to-plate

distance and flow rate were fixed at 13 cm and 0.6 ml/h, respectively. Sample S6, with an applied voltage of 12 kV, exhibited an average fiber diameter of 225.28 ± 88 nm. Conversely, S8 and S7, subjected to 14 kV and 16 kV, yielded average diameters of 205.28 ± 50 nm and 175.74 ± 41 nm, respectively.

A reduction in fiber diameter correlated with an increase in applied voltage. To enhance the analysis, additional sets of samples were tested: S9 and S10 received voltages of 16 kV and 12 kV, while maintaining a needle-to-plate distance of 13 cm and a flow rate of 1 ml/h. Their average fiber diameters were recorded as 194.4 ± 41 nm and 231.1 ± 76 nm, respectively. For S12 and S13, voltages of 18 kV and 17 kV were applied, with a flow rate of 0.4 ml/h and a needle-to-plate distance of 20 cm, resulting in average diameters of 385.6 ± 149 nm and 424.6 ± 125 nm. Further, S16 and S17 were subjected to 19 kV and 18 kV, producing average fiber diameters of 335.1 ± 181 nm and 423.28 ± 130 nm, respectively. In S18 and S19, voltages of 20 kV and 19 kV resulted in average diameters of 385.18 ± 183 nm and 506.62 ± 149 nm. Overall, fiber diameter consistently decreased with increasing voltage, as illustrated in Figure 3. These findings align with results reported by Beachley et al., which noted a reduction in diameter as voltage increased (Beachley & Wen, 2008). The increase in applied voltage enhances the electric field between the needle and the collector plate, leading to elevated surface tension due to heightened coulombic forces. Consequently, the nanofiber diameter decreases with increased voltage (Can-Herrera et al., 2021).

As depicted in SEM images in Figures 2 and 4, the morphology of the nanofibers consists of both fibers and beads. Figure 5 illustrates how increasing voltage affects fiber morphology; specifically, the average diameter of beads in the fibers diminishes with higher voltage. Increased voltage can eliminate the beaded structure within the nanofibers, consistent with observations by Jarusuwannapoom et al. (Jarusuwannapoom et al., 2004). Bead formation may result from viscosity-related forces and surface tension, as the number of charge carriers in the jet rises with increasing electrostatic fields. This increase leads to stronger electrostatic and coulombic forces, which in turn elevate surface tension and enhance repulsion between the fibers, reducing the likelihood of bead formation.

### 3.2. Flow Rate

The flow rate significantly influences the morphology and diameter of the fibers by controlling the volume of the electrospinning solution. In samples S4 and S5, where the voltage was set at 12 kV and the needle-to-plate distance at 12 cm, changing the flow rate from 0.4 to 0.6 ml/h resulted in an increase in average fiber diameter from 210.66 ± 43 nm to 223.18 ± 44 nm.

When the flow rate was increased under a voltage of 16 kV and a needle-to-plate distance of 13 cm, the average fiber diameters for samples S7 and S9, with flow rates of 0.6 and 1 ml/h, were 175.74±41 nm and 194.4±41 nm, respectively. Further testing with additional sample groups (S6 and S10) showed that increasing the flow rate from 0.6 to 1 ml/h led to fiber diameters of 225.28 ± 88 nm and 232.4±74 nm. Similarly, for samples S16 and S19, an increase in flow rate from 0.6 to 0.8 ml/h resulted in average fiber diameters of 335.1 ± 118 nm and 506.62 ± 142 nm, respectively. Figure 6 illustrates the impact of flow rate on fiber diameter.

Previous research has indicated a direct correlation between fiber diameter and flow rate (Zargham et al., 2012). At higher flow rates, a larger volume of solution exits the needle, requiring more time for solvent evaporation. If the flow rate is too high, there may not be enough time for the solvent to evaporate completely, causing the remaining solvent to either draw the fibers together or create droplets at the needle tip. This results in thicker fibers often exhibiting a beaded structure. As shown in Figure 7, samples contain a mixture of fibers and beads. Figure 8 further highlights how lower flow rates yield fibers with smaller beads. Additionally, insufficient time for solvent evaporation can lead to other defects, such as branched fibers.

### 3.3. Needle-to-plate distance

The needle-to-plate distance is another critical variable in the electrospinning process. For samples S4 and S3, where the voltage was set at 12 kV and the flow rate at 0.4 ml/h, an increase in distance from 12 to 15 cm resulted in a decrease in fiber diameter, with average diameters reported at 210.66 ± 43 nm and 181.62±37 nm, respectively. Similarly, in samples S15 and S13, increasing the distance from 18 to 20 cm led to a reduction in average fiber diameter from 457.5 ±140 nm to 424.6±130 nm. Previous studies have also demonstrated a decrease in fiber diameter with increased needle-to-plate distance (Ginestra et al., 2016).

A longer distance allows the polymer solution more time for solvent evaporation, which contributes to a reduction in fiber diameter. However, contrasting results were observed in samples S6 and S10; as the distance increased from 11 to 13 cm, fiber diameters were reported at 201.92±35 nm and 225.28±38 nm, respectively. Yogendra Pratap et al. (Singh et al., 2020) noted that while increasing the needle-to-plate distance initially reduces fiber diameter due to extended solvent evaporation time, a further increase can lead to larger diameters because of a diminished electrostatic field. Figure 9 illustrates the effect of varying the needle-to-plate distance on the diameter of electrospun fibers. SEM images in Figure 10 reveal a beaded structure in the electrospun fibers. A short needle-to-plate distance may hinder complete solvent evaporation, resulting in non-dried fibers being deposited on the collector plate. If solvent remains in the final solution, the fibers can merge or form droplets at the needle tip. Figure 11 shows that

the diameter of the beads decreases as the distance increases, with a significant reduction observed for samples S3 and S4.

### 3.4. Solution conductivity

The conductivity of the polymer solution is influenced by the choice of solvents, salts, and polymers. An increase in the solution's electrical conductivity significantly correlates with a decrease in the diameter of electrospun nanofibers. This phenomenon occurs because the repulsive forces between the charges on the surface of the electrospinning jet enhance the stretching of the solution. As the conductivity of the solution rises, the charge on the polymer jet increases, leading to a reduction in fiber diameter. Additionally, incorporating small quantities of salt compounds, such as NaCl, into the polymer solution can help prevent the formation of beaded fibers, resulting in more uniform structures. However, achieving a high solution conductivity can complicate the electrospinning process, even at elevated voltages (Jarusuwannapoom et al., 2004).

In this study, samples S20 and S21 were electrospun with flow rates of 0.6 ml/h and 0.5 ml/h, voltages of 11.5 kV and 16 kV, and needle-to-plate distances of 18 cm and 16 cm, respectively. Solution 4, which contained a small amount of LiCl salt, produced fragile and bead-free fibers, as confirmed by SEM images, owing to the high conductivity of the solution. Nevertheless, while increased conductivity can enhance fiber uniformity, it also poses challenges in fiber collection. Figure 12 displays SEM images of S20 and S21, illustrating fractured and separated fibers due to the high conductivity of the solution.

## 4. DISCUSSION

Studies have indicated that multiple variables influence the morphology of scaffolds in the electrospinning process. This study demonstrated that increasing the voltage reduces the diameter of electrospun fibers, aligning with previous findings. However, some researchers argue that higher applied voltage can lead to an increase in fiber diameter due to reduced solvent evaporation time (Dickinson & Gerecht, 2016). Notably, smaller beads were observed within the fiber structure at elevated voltages. The effects of other variables—such as flow rate, needle-to-plate distance, and solution conductivity—were also examined.

SEM images from samples S12 to S21 revealed bead-free fibers. The high conductivity of the solution, resulting from the addition of LiCl salt in samples S20 and S21, facilitated the formation of these bead-free fibers. Table 1 summarizes the processing conditions for each sample. Samples S12 to S19 exhibited higher applied voltages and longer needle-to-plate distances, with beaded structures observed at voltages below 18 kV. Bead-free fibers were predominantly found in samples with lower flow rates. The effect of distance on fiber morphology was also investigated, revealing that the presence of beads is inevitable at distances less than 18 cm. Fibers characterized by thicker diameters and a bead-free structure were found to be superior.

As highlighted, understanding the simultaneous effects of various parameters is crucial for identifying optimal conditions. For instance, while increasing the distance generally reduces nanofiber diameter, an optimal distance can further decrease fiber diameter (Singh et al., 2020). It is essential to recognize that each parameter has a specific optimal value.

In summary, several processing variables significantly impact the morphology of nanofibers in the electrospinning process. Achieving a desirable structure of electrospun fibers requires careful control of these parameters, which is vital for applications in healthcare. The use of polymers in wound dressings has garnered considerable attention, with polycaprolactone (PCL) emerging as a preferred choice due to its remarkable properties. However, its hydrophobic nature can result in poor cellular responses. These findings indicate that adjusting electrospinning parameters can facilitate the creation of an ideal fiber structure.

## 5. CONCLUSION

PCL is highly regarded in medical applications due to its exceptional properties. Electrospinning PCL can create an ideal wound dressing with excellent characteristics. The processing conditions significantly impact the structure of electrospun fibers, and this research aims to develop interconnected, bead-free PCL fibers. By accurately and concurrently controlling processing variables, it is possible to achieve such a desired structure.

The results indicated that smooth, bead-free fibers can be produced at low flow rates, high voltages, and longer distances. However, excessive conductivity in the solution can lead to fiber breakage. Additionally, the semi-crystalline and hydrophobic nature of PCL results in slow degradation (2 to 4 years), which can limit its application as a wound dressing. Therefore, further research on the electrospinning process of PCL is necessary to enhance its hydrophobicity.

## 6. Acknoledgement

The authors would like to acknowledge Paretavous Research Institute for all supports throughout this work.

## REFERENCES

1. Abdollahi, E., & Bakhsheshi-Rad, H. (2018). Evaluation of mechanical properties and apatite formation of synthesized fluorapatite-hardystonite nanocomposite scaffolds. *Advanced* Ceramics Progress, *4*(Issue 3-4), 8-15. https://doi.org/10.30501/acp.2018.92930

2. Abrisham, M., Noroozi, M., Panahi-Sarmad, M., Arjmand, M., Goodarzi, V., Shakeri, Y., Golbaten-Mofrad, H., Dehghan, P., Sahzabi, A. S., Sadri, M., & Uzun, L. (2020). The role of polycaprolactone-triol (PCL-T) in biomedical applications: A state-of-the-art review. European Polymer Journal, 131, 109701. https://doi.org/10.1016/j.eurpolymj.2020.109701

3. Azimi, B., Nourpanah, P., Rabiee, M., & Arbab, S. (2014b). Poly (-caprolactone) fiber: an overview. Journal of Engineered Fibers and Fabrics, 9(3), 155892501400900. https://doi.org/10.1177/155892501400900309
4. Baji, A., Mai, Y., Wong, S., Abtahi, M., & Chen, P. (2010). Electrospinning of polymer nanofibers: Effects on oriented morphology, structures and tensile properties. Composites Science and Technology, 70(5), 703–718. https://doi.org/10.1016/j.compscitech.2010.01.010
5. Beachley, V., & Wen, X. (2008). Effect of electrospinning parameters on the nanofiber diameter and length. Materials Science and Engineering C, 29(3), 663–668. https://doi.org/10.1016/j.msec.2008.10.037
6. Can-Herrera, L., Oliva, A., Dzul-Cervantes, M., Pacheco-Salazar, O., & Cervantes-Uc, J. (2021). Morphological and mechanical properties of electrospun polycaprolactone scaffolds: effect of applied voltage. Polymers, 13(4), 662. https://doi.org/10.3390/polym13040662
7. Chinnappan, B. A., Krishnaswamy, M., Xu, H., & Hoque, M. E. (2022). Electrospinning of Biomedical Nanofibers/Nanomembranes: Effects of process parameters. Polymers, 14(18), 3719. https://doi.org/10.3390/polym14183719
8. Dias, J., Baptista-Silva, S., De Oliveira, C., Sousa, A., Oliveira, A., Bártolo, P., & Granja, P. (2017). In situ crosslinked electrospun gelatin nanofibers for skin regeneration. European Polymer Journal, 95, 161–173. https://doi.org/10.1016/j.eurpolymj.2017.08.015
9. Dias, J., Baptista-Silva, S., Sousa, A., Oliveira, A., Bártolo, P., & Granja, P. (2018). Biomechanical performance of hybrid electrospun structures for skin regeneration. Materials Science and Engineering C, 93, 816–827. https://doi.org/10.1016/j.msec.2018.08.050
10. Dickinson, L. E., & Gerecht, S. (2016). Engineered biopolymeric scaffolds for chronic wound healing. Frontiers in Physiology, 7. https://doi.org/10.3389/fphys.2016.00341
11. Dong, Y., Zheng, Y., Zhang, K., Yao, Y., Wang, L., Li, X., Yu, J., & Ding, B. (2020). Electrospun Nanofibrous materials for wound healing. Advanced Fiber Materials, 2(4), 212–227. https://doi.org/10.1007/s42765-020-00034-y
12. Doustgani, A. (2015). Effect of electrospinning process parameters of polycaprolactone and nanohydroxyapatite nanocomposite nanofibers. Textile Research Journal, 85(14), 1445–1454. https://doi.org/10.1177/0040517514566109
13. Dwivedi, R., Kumar, S., Pandey, R., Mahajan, A., Nandana, D., Katti, D. S., & Mehrotra, D. (2019). Polycaprolactone as biomaterial for bone scaffolds: Review of literature. Journal of Oral Biology and Craniofacial Research, 10(1), 381–388. https://doi.org/10.1016/j.jobcr.2019.10.003
14. Elkhouly, H., Mamdouh, W., & El-Korashy, D. I. (2021). Electrospun nano-fibrous bilayer scaffold prepared from polycaprolactone/gelatin and bioactive glass for bone tissue engineering. Journal of Materials Science Materials in Medicine, 32(9). https://doi.org/10.1007/s10856-021-06588-6
15. Ferreira, C. a. M., Januário, A. P., Félix, R., Alves, N., Lemos, M. F. L., & Dias, J. R. (2021). Multifunctional Gelatin/Chitosan Electrospun Wound Dressing Dopped with Undaria pinnatifida Phlorotannin-Enriched Extract for Skin Regeneration. Pharmaceutics, 13(12), 2152. https://doi.org/10.3390/pharmaceutics13122152
16. Ghaffarian, Z., FaqihImani, A., Doostmohammadi, A., & Saeri, M. (2015). Fabrication, Characterization and Process Parameters Optimization of Electrospun 58S Bioactive Glass Submicron Fibers. *Advanced Ceramics Progress*, *1*(3), 16-21. https://doi.org/0.30501/acp.2015.70007
17. Gil-Castell, O., Badia, J., Ontoria-Oviedo, I., Castellano, D., Sepúlveda, P., & Ribes-Greus, A. (2019). Polycaprolactone/gelatin-based scaffolds with tailored performance: in vitro and in vivo validation. Materials Science and Engineering C, 107, 110296. https://doi.org/10.1016/j.msec.2019.110296
18. Ginestra, P., Ceretti, E., & Fiorentino, A. (2016). Electrospinning of poly-caprolactone for scaffold manufacturing: experimental investigation on the process parameters influence. Procedia CIRP, 49, 8–13. https://doi.org/10.1016/j.procir.2015.07.020
19. Ifegwu, O. C., & Anyakora, C. (2018). The place of electrospinning in separation science and biomedical engineering. In InTech eBooks. https://doi.org/10.5772/intechopen.77221
20. Jarusuwannapoom, T., Hongrojjanawiwat, W., Jitjaicham, S., Wannatong, L., Nithitanakul, M., Pattamaprom, C., Koombhongse, P., Rangkupan, R., & Supaphol, P. (2004). Effect of solvents on electro-spinnability of polystyrene solutions and morphological appearance of resulting electrospun polystyrene fibers. European Polymer Journal, 41(3), 409–421. https://doi.org/10.1016/j.eurpolymj.2004.10.010
21. Joseph, B., Augustine, R., Kalarikkal, N., Thomas, S., Seantier, B., & Grohens, Y. (2019). Recent advances in electrospun polycaprolactone based scaffolds for wound healing and skin bioengineering applications. Materials Today Communications, 19, 319–335. https://doi.org/10.1016/j.mtcomm.2019.02.009
22. Jun, I., Han, H., Edwards, J., & Jeon, H. (2018). Electrospun Fibrous Scaffolds for Tissue Engineering: Viewpoints on architecture and Fabrication. International Journal of Molecular Sciences, 19(3), 745. https://doi.org/10.3390/ijms19030745
23. Linh, N. V. V., Du, N., My, N. T. N., Tuyen, N. N., Phu, H. D., & Tram, N. X. T. (2022). Electrospun Polycaprolactone/Hydroxyapatite (PCL/HAp) microfibers as potential biomaterials for tissue engineering. Materials Today Proceedings, 66, 2895–2899. https://doi.org/10.1016/j.matpr.2022.06.553
24. Liu, X., Holzwarth, J. M., & X, P., MA. (2012). Functionalized synthetic biodegradable polymer scaffolds for tissue engineering. Macromolecular Bioscience, 12(7), 911–919. https://doi.org/10.1002/mabi.201100466
25. Liverani, L., & Boccaccini, A. (2016). Versatile production of Poly(Epsilon-Caprolactone) fibers by electrospinning using benign solvents. Nanomaterials, 6(4), 75. https://doi.org/10.3390/nano6040075
26. Liverani, L., & Boccaccini, A. (2016b). Versatile production of Poly(Epsilon-Caprolactone) fibers by electrospinning using benign solvents. Nanomaterials, 6(4), 75. https://doi.org/10.3390/nano6040075
27. Loh, Q. L., & Choong, C. (2013). Three-dimensional scaffolds for tissue engineering applications: role of porosity and pore size. https://doi.org/10.1089/ten.teb.2012.0437
28. Moniri Javadhesari, S., Koohi, M., & Jabraili, M. (2022). Nanomaterials: Applications in Regeneration of Damaged Tissues. *Advanced Ceramics Progress*, *8*(4), 1-14. https://doi.org/10.30501/acp.2022.356039.1100
29. Samadian, H., Maleki, H., Allahyari, Z., & Jaymand, M. (2020). Natural polymers-based light-induced hydrogels: Promising biomaterials for biomedical applications. Coordination Chemistry Reviews, 420, 213432. https://doi.org/10.1016/j.ccr.2020.213432
30. Siddiqui, N., Kishori, B., Rao, S., Anjum, M., Hemanth, V., Das, S., & Jabbari, E. (2021b). Electropsun Polycaprolactone Fibres in Bone Tissue Engineering: a review. Molecular Biotechnology, 63(5), 363–388. https://doi.org/10.1007/s12033-021-00311-0

31. Singh, Y. P., Dasgupta, S., Nayar, S., & Bhaskar, R. (2020). Optimization of electrospinning process & parameters for producing defect-free chitosan/polyethylene oxide nanofibers for bone tissue engineering. Journal of Biomaterials Science Polymer Edition, 31(6), 781–803. https://doi.org/10.1080/09205063.2020.1718824

32. Stratton, S., Shelke, N. B., Hoshino, K., Rudraiah, S., & Kumbar, S. G. (2016). Bioactive polymeric scaffolds for tissue engineering. Bioactive Materials, 1(2), 93–108. https://doi.org/10.1016/j.bioactmat.2016.11.001

33. Vig, K., Chaudhari, A., Tripathi, S., Dixit, S., Sahu, R., Pillai, S., Dennis, V., & Singh, S. (2017). Advances in skin regeneration using tissue engineering. International Journal of Molecular Sciences, 18(4), 789. https://doi.org/10.3390/ijms18040789

34. Vyas, K. S., & Vasconez, H. C. (2014). Wound healing: biologics, skin substitutes, biomembranes and scaffolds. Healthcare, 2(3), 356–400. https://doi.org/10.3390/healthcare2030356

35. Wang, T., Zhu, X., Xue, X., & Wu, D. (2011). Hydrogel sheets of chitosan, honey and gelatin as burn wound dressings. Carbohydrate Polymers, 88(1), 75–83. https://doi.org/10.1016/j.carbpol.2011.11.069

36. Yang, G., Li, X., He, Y., Ma, J., Ni, G., & Zhou, S. (2017). From nano to micro to macro: Electrospun hierarchically structured polymeric fibers for biomedical applications. Progress in Polymer Science, 81, 80–113. https://doi.org/10.1016/j.progpolymsci.2017.12.003

37. Zargham, S., Bazgir, S., Tavakoli, A., Rashidi, A. S., & Damerchely, R. (2012). The effect of flow rate on morphology and deposition area of electrospun nylon 6 nanofiber. Journal of Engineered Fibers and Fabrics, 7(4), 155892501200700. https://doi.org/10.1177/155892501200700414

Advanced Ceramics Progress: Vol. 10, No. 1, (Winter 2024) 18-21

Materials and Energy Research Center
MERC

Contents lists available at ACERP

Advanced Ceramics Progress

Journal Homepage: www.acerp.ir

**Original Research Article**

# Investigating the Effects of $CeO_2$ Addition on the Structure of $MgO-Al_2O_3-SiO_2$ Glass Using FTIR and Raman Analysis

Farshad Soleimani [a]*, Hamed Aghababaei [b], Mostafa Kargar [c], Masoumeh Torkashevand [c], Alireza Hemmati [c]

[a] *Assistant Professor, Department of Materials Engineering, Engineering Faculty, Malayer University, Malayer, Hamedan, Iran.*
[b] *PhD student, Department of Ceramics, Engineering Faculty, Materials and Energy Research Center, Karaj, Iran.*
[c] *Bachlor of Science, Department of Materials Engineering, Engineering Faculty, Malayer University, Malayer, Hamedan, Iran.*

* Corresponding Author Email: F.soleimani@malayeru.ac.ir ; f.soleimany@yahoo.com (Farshad Soleimani)
URL: https://www.acerp.ir/article_207692.html

*ARTICLE INFO*

*Article History:*
Received: 29 January 2024
Revised: 07 February 2024
Accepted: 08 February 2024

*Keywords*:
Silicate Glass,
Structural Analysis,
FTIR,
Raman,
Cerium Oxide

*ABSTRACT*

The $MgO-Al_2O_3-SiO_2$ (MAS) glass system has long been of interest due to its potential to be converted into glass-ceramics containing spinel and cordierite phases. This study investigated the effect of adding varying amounts of cerium oxide (1-5% by weight) on the structure of the $MgO-Al_2O_3-SiO_2$ glass system. After mixing the raw materials, the samples were melted at 1600°C, and the density of the glass samples was measured using the Archimedes method. FTIR analyses, covering both far and mid-infrared ranges, as well as Raman spectroscopy, were conducted on the glass samples. To improve detection accuracy, the obtained spectra were deconvoluted. The results showed that the addition of cerium oxide increased the density from 2.53 g/cm³ to 2.69 g/cm³. Furthermore, the data indicated that cerium oxide in concentrations below 5% acts as a modifier. At lower concentrations, cerium predominantly exists in the $Ce^{3+}$ state, increasing the number of non-bridging oxygens (NBOs), while at higher concentrations, $Ce^{3+}$ is mostly converted to $Ce^{4+}$, which in turn reduces the NBO concentration.

https://doi.org/10.30501/acp.2024.435473.1145

## 1. INTRODUCTION

The $MgO-Al_2O_3-SiO_2$ (MAS) glass system has long been of interest due to its ability to be converted into glass-ceramics containing spinel and cordierite phases (Chen et al., 2007; Holand et al., 2012)(Rezvani et al., 2005). These glass-ceramics have been applied in various fields, including military uses such as anti-bullet armor and radomes, as well as anti-wear tiles in the construction industry (Soleimani et al., 2015; Zou et al., 2013). The properties of glass-ceramics are strongly influenced by the structural and physical characteristics of the base glass. Glass transition temperature, dilatometric and crystallization temperature, thermal expansion coefficient, and various physical and chemical properties of glass-ceramics are all affected by the base glass structure (Komatsu, 2015). Research has shown that $[SiO_4]$ and $[AlO_6]$ groups, along with smaller amounts of $[MgO_4]$ groups, are the most important structural groups in MAS glasses (El-Damrawi et al., 2018). It is well known that the introduction of certain transition cations leads to structural changes in glass and alters its properties. For instance, Zhang et al. (Zhang et al., 2020) demonstrated that the addition of $Cr^{+}$ increases the number of non-bridging oxygens (NBOs), leading to

Please cite this article as: Soleimani, F., Aghababaei, H., Kargar, M., Torkashevand, M. & Hemmati, A. (2024). Investigating the Effects of CeO2 Addition on the Structure of MgO-Al2O3-SiO2 Glass Using FTIR and Raman Analysis, *Advanced Ceramics Progress*, 10(1), 18-21. https://doi.org/10.30501/acp.2024.435473.1145

2423-7485/© 2024 The Author(s). Published by MERC.
This is an open access article under the CC BY license (https://creativecommons.org/licenses/by/4.0/).

changes in the glass network. The presence of cations like chromium has also been shown to affect the physical properties of MAS glass, such as luminescence.

Cerium oxide ($CeO_2$) is another oxide compound of interest, and its incorporation into glass compositions induces significant structural changes. $CeO_2$ has been identified as an intermediate in glasses (M. B. Volf, 1984), meaning it can act as either a modifier or a glass former depending on the glass composition, the amount of cerium oxide present, and the production conditions (Soleimani et al., 2012). In silicate and phosphate glasses, cerium oxide typically increases density and imparts luminescent properties.

The objective of this study is to investigate the structural effects induced by the addition of small amounts of cerium oxide to MAS glass using structural analysis techniques.

## 2. MATERIALS AND METHODS

A composition of 41 wt% $SiO_2$ with 5 wt% MnO and $ZrO_2$ (in equal amounts, making up the balance) was considered for the study. To prepare the raw materials, high-purity oxides (≥99%) were used according to the specified composition. To investigate the effect of adding $CeO_2$, 1 wt% (G-Ce1), 3 wt% (G-Ce3), and 5 wt% (G-Ce5) of cerium oxide were substituted for $SiO_2$ in the base composition. After mixing the raw materials, 50 g of each batch was poured into alumina crucibles and melted at 1600°C in an electric furnace. After one hour of holding at the maximum temperature, the molten glass was cast into a preheated steel mold. The cast parts were then immediately transferred to a furnace set at 600°C, where they were slowly cooled to ambient temperature.

The density of the samples was measured using the Archimedes method. Samples were then prepared from each piece for structural analysis. For this purpose, the glass pieces were ground using an agate mortar. The resulting powder samples were mixed with KBr powder at a ratio of 1:100 and pressed to create suitable samples for FTIR analysis. FTIR analysis was performed on the samples across two spectral ranges: the far-infrared range (100-400 $cm^{-1}$) and the mid-infrared range (4000-2000 $cm^{-1}$).

Raman analysis was also conducted on pure powder samples of the glasses. The deconvolution technique was applied to the FTIR spectra to more accurately determine the positions of the peaks.

## 3. RESULTS AND DISCUSSION

Table 1 shows the results of density measurement. It is determined that with the addition of $CeO_2$, density increases, given the atomic weight of Ce.

**TABLE 1.** Density of glass samples (g/cm3)

| Code | Density |
|---|---|
| Ge-Ce0 | 2.55±0.03 |
| Ge-Ce1 | 2.57±0.02 |
| Ge-Ce3 | 2.64±0.03 |
| Ge-Ce5 | 2.69±0.01 |

The FTIR absorption spectrum of the glass samples was measured in the range of 400-2000 cm-1, as shown in Figure 1.

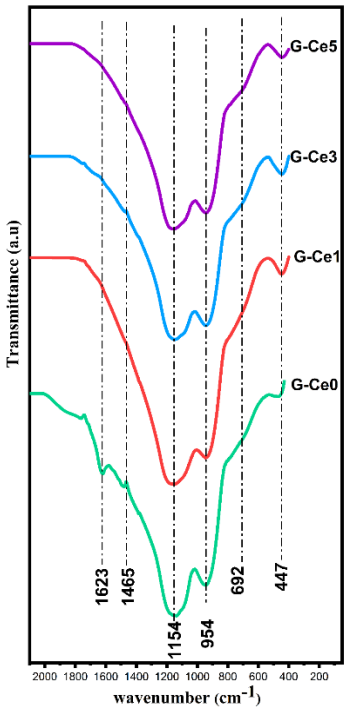


**Figure 1.** FTIR absorption spectrum of G-Ce0, G-Ce1, G-Ce3, and G-Ce5 glass samples.

The band in the range of 450 $cm^{-1}$ is attributed to the bending vibrations of O-Si-O and Si-O-Si bond (Handke et al., 1993)(Aguiar et al., 2009)(Abdelwahab et al., 2021). The peak observed around 692 $cm^{-1}$ corresponds to the bending vibrations of Si–O–Al and Si–O–Si bonds, and no significant changes were detected in the spectrum with the addition of $CeO_2$ (Yan et al., 2012). The strong absorption band in the range of 900–1120 $cm^{-1}$ exhibits the highest intensity in the IR spectra of various glasses, attributed to the stretching vibrations. Two distinct absorption bands are observed at 1954 $cm^{-1}$ and 1154 $cm^{-1}$, with the vibration intensity at 1154 $cm^{-1}$ being higher than that at 1954 $cm^{-1}$. These bands are associated with the stretching vibration of Si–O–Si in $Q^2$ (1154 $cm^{-1}$) and the asymmetric vibration of Si–O–Si in $Q^3$ (1954 $cm^{-1}$), respectively (Handke et al., 1993)(Kazancioglu et al., 2021)(Fang et al., 2020).

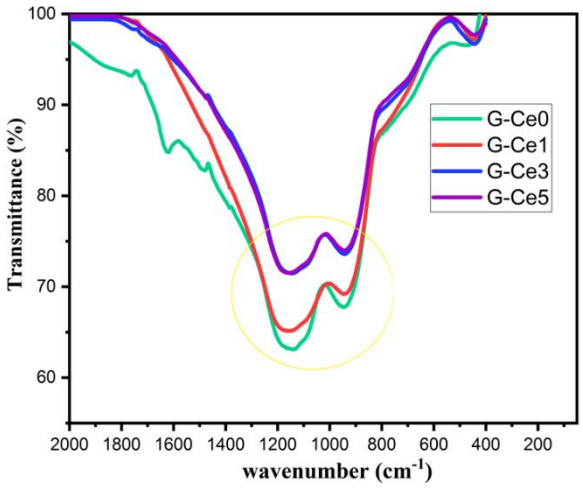


**Figure 2.** FTIR absorption spectrum of G-Ce0, G-Ce1, G-Ce3, and G-Ce5 glass samples.

Figure 2 clearly demonstrates that the addition of $CeO_2$ reduced the intensity of the bands at 1954 cm$^{-1}$ and 1154 cm$^{-1}$. The weak peak at 1465 cm$^{-1}$ is attributed to the stretching and deformation vibrations of the $CH_2$ group (Liu et al., 2020). The peak at 1623 cm$^{-1}$ corresponds to the bending vibrations of $H_2O$ molecules (Abdelwahab et al., 2021). To further examine the effect of $CeO_2$ addition, the Raman spectra of G-Ce0, G-Ce1, G-Ce3, and G-Ce5 glasses were analyzed, as shown in Figure 3.

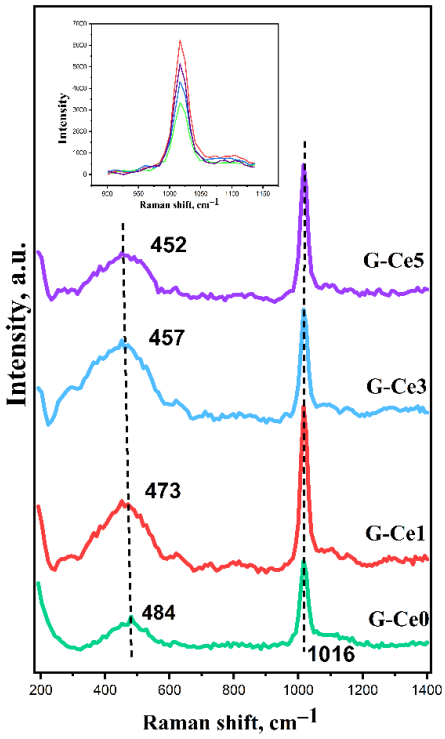


**Figure 3.** Raman spectrum of G-Ce0, G-Ce1, G-Ce3, and G-Ce5 glass samples.

The Raman spectra of G-Ce0, G-Ce1, G-Ce3, and G-Ce5 glasses are shown in Figure 3. Based on the results, the peak around 490 cm$^{-1}$ corresponds to the bending vibrations of Si–O–Si bonds (Aguiar et al., 2009). The addition of $CeO_2$ to the glass caused a shift of this peak to a lower wavenumber, indicating changes in Si–O–Si vibrations. At higher wavenumbers, a sharp peak near 1016 cm$^{-1}$, associated with Si–O vibrations in the $Q^3$ structure, was observed, and the addition of $CeO_2$ increased the intensity of this peak (Fang et al., 2020). A decrease in the intensity of the bands at 954 cm$^{-1}$ and 1154 cm$^{-1}$ in the FTIR spectrum, which are related to Si–O–Si vibrations, along with the shift of the peak at 1490 cm$^{-1}$ to a lower wavenumber and an increase in the intensity of the band at 1016 cm$^{-1}$ in the Raman spectrum upon the addition of $CeO_2$, is attributed to non-bridging oxygens (NBOs). This suggests that cerium oxide disrupts Si–O–Si bonds. In this study, it is assumed that alumina integrates into the Si–O tetrahedral network and remains unaffected by the addition of $CeO_2$. As seen in previous studies on aluminosilicate glasses (Lin et al., 1996), borosilicate (Deshpande et al., 2010), and lead silicate glasses (Wang et al., 2016) cerium oxide acts as a network modifier. The results of this study similarly show that the addition of cerium oxide increases the number of non-bridging oxygens, indicating its role as a silicate network modifier. The addition of cerium oxide to glass exhibits non-linear behavior in the Raman spectrum regarding peak intensity. This behavior is likely due to the multivalent states of cerium oxide in the glass melt. As expressed in the redox reaction (Equation 1), $Ce^{3+}$ ions promote the formation of NBOs.

$$Ce^{4+} + O^{-} \Rightarrow Ce^{3+} + O \quad (1)$$

At lower concentrations, cerium predominantly exists in the $Ce^{3+}$ state, producing more NBOs. However, at higher concentrations, $Ce^{3+}$ is mostly converted to $Ce^{4+}$, reducing NBO concentration. Thus, the variation in NBO concentration as a function of cerium content has a significant impact on the non-linear changes in the connectivity of the silicate network (Wang et al., 2015).

## 4. CONCLUSIONS

Glasses containing cerium oxide in the MAS system were successfully prepared. It was demonstrated that the addition of cerium oxide increased the density from 2.55 to 2.69 g/cm$^3$ in glasses containing 5 wt% cerium oxide. The incorporation of $CeO_2$ also reduced the intensity of the bands at 1954 cm$^{-1}$ and 1154 cm$^{-1}$. At lower concentrations, cerium primarily exists in the $Ce^{3+}$ state, leading to an increase in non-bridging oxygens (NBOs). However, at higher concentrations, $Ce^{3+}$ is largely converted to $Ce^{4+}$, resulting in a reduction in NBO concentration.

## 5. Acknowledgement

The authors would like to express sincere appreciation to Malayer University for financial support.

## REFERENCES


1. Abdelwahab, S. A., Ali, A., Abdelwahed, K., Ahmed, I., & Ali, A. I. (2021). Influence of TiO2/GO weight ratio on the structure, mechanical, and electrical properties of SiO2–Al2O3 glass–ceramics. *Journal of Materials Science: Materials in Electronics*, *32*(8), 11092–11106. https://doi.org/10.1007/s10854-021-05774-0
2. Aguiar, H., Serra, J., González, P., & León, B. (2009). Structural study of sol-gel silicate glasses by IR and Raman spectroscopies. *Journal of Non-Crystalline Solids*, *355*(8), 475–480. https://doi.org/10.1016/j.jnoncrysol.2009.01.010
3. Chen, G.-H., & Liu, X.-Y. (2007). Sintering, crystallization and properties of MgO–Al2O3–SiO2 system glass-ceramics containing ZnO. *Journal of Alloys and Compounds*, *431*(1–2), 282–286. http://dx.doi.org/10.1016/j.jallcom.2006.05.060
4. Deshpande, V. K., & Taikar, R. N. (2010). Effect of cerium oxide addition on electrical and physical properties of alkali borosilicate glasses. *Materials Science and Engineering: B*, *172*(1), 6–8. https://doi.org/10.1016/j.mseb.2010.04.003
5. El-Damrawi, G., & Behairy, A. (2018). Structural Role of Cerium Oxide in Lead Silicate Glasses and Glass Ceramics. *Journal of Minerals and Materials Characterization and Engineering*, *06*(03), 438–447. https://doi.org/10.4236/jmmce.2018.63031
6. Fang, J., Pang, Z., Xing, X., & Xu, R. (2020). Thermodynamic Properties, Viscosity, and Structure of CaO–SiO2–MgO–Al2O3–TiO2–Based Slag. *Materials*, *14*(1), 124. https://doi.org/10.3390/ma14010124
7. Handke, M., & Mozgawa, W. (1993). Vibrational spectroscopy of the amorphous silicates. *Vibrational Spectroscopy*, *5*(1), 75–84. https://doi.org/10.1016/0924-2031(93)87057-Z
8. Holand, W., & Beall, G. (2012). Glass ceramic technology. In John Wiley & Sons. John Wiley & Sons, Inc., Hoboken, New Jersey. Published. https://www.google.com/books/edition/Glass_Ceramic_Technology/tu2lDwAAQBAJ?hl=en&gbpv=0
9. Kazancioglu, M., Tsilomelekis, G., Lehman, R., & Hara, M. (2021). FTIR studies on plasticization of silicate glass with ionic liquids (conversion to silicate polymers). *Journal of Non-Crystalline Solids*, *561*(March). https://doi.org/10.1016/j.jnoncrysol.2021.120757
10. Komatsu, T. (2015). Design and control of crystallization in oxide glasses. *Journal of Non-Crystalline Solids*, *428*, 156–175. https://doi.org/10.1016/j.jnoncrysol.2015.08.017
11. Lin, S.-L., & Hwang, C.-S. (1996). Structures of CeO2 Al2O3 SiO2 glasses. *Journal of Non-Crystalline Solids*, *202*(1–2), 61–67. https://doi.org/10.1016/0022-3093(96)00138-X
12. Liu, H., Jie, C., Ma, Y., Wang, Z., & Wang, X. (2020). Synthesis and Processing Effects on Microstructure and Mechanical Properties of Forsterite Ceramics. *Transactions of the Indian Ceramic Society*, *79*(2), 83–87. https://doi.org/10.1080/0371750X.2020.1722754
13. M. B. Volf. (1984). Chemical approach to glass. *Glass Science and Technology*, 594. https://www.google.com/books/edition/Chemical_Approach_to_Glass/Zh0EfAEACAAJ?hl=en
14. Rezvani, M., Eftekhari-Yekta, B., Solati-Hashjin, M., & Marghussian, V. K. (2005). Effect of Cr2O3, Fe2O3 and TiO2 nucleants on the crystallization behaviour of SiO2–Al2O3–CaO–MgO(R2O) glass-ceramics. *Ceramics International*, *31*(1), 75–80. https://doi.org/10.1016/j.ceramint.2004.03.037
15. Soleimani, F., Aghaei, A. R., Zakeri, M., Eshraghi, M. J., & Alizadeh, M. (2015). Production of glass-ceramic from high frequency induction melted cordierite glass. *Journal of Non-Crystalline Solids*, *429*, 219–225. https://doi.org/10.1016/j.jnoncrysol.2015.09.014
16. Soleimani, F., & Rezvani, M. (2012). The effects of CeO 2 addition on crystallization behavior and pore size in microporous calcium titanium phosphate glass ceramics. *Materials Research Bulletin*, *47*(6), 1362–1367. https://doi.org/10.1016/j.materresbull.2012.03.010
17. Wang, Z., & Cheng, L. (2015). Structural Features and Synthesis of CeO2-Doped Boroaluminosilicate Oxyfluoride Transparent Glass Ceramics. *Journal of Chemistry*, *2015*. https://doi.org/10.1155/2015/597537
18. Wang, Z., & Cheng, L. (2016). Structural evolution of CeO 2-doped alkali boroaluminosilicate glass and the correlation with physical properties based on a revised structural parameter analysis. *RSC Advances*, *6*(7), 5456–5465. https://doi.org/10.1039/C5RA20487A
19. Yan, W., Liu, D., Tan, D., Yuan, P., & Chen, M. (2012). FTIR spectroscopy study of the structure changes of palygorskite under heating. *Spectrochimica Acta - Part A: Molecular and Biomolecular Spectroscopy*, *97*, 1052–1057. https://doi.org/10.1016/j.saa.2012.07.085
20. Zhang, S., Zhang, Y., & Qu, Z. (2020). Effects of soluble Cr2O3 doping on the glass structure, microstructure, crystallization behavior, and properties of MgO–Al2O3–SiO2 sapphirine glass ceramics. *Materials Chemistry and Physics*, *252*, 123115. https://doi.org/10.1016/j.matchemphys.2020.123115
21. Zou, D., Chu, X., & Wu, F. (2013). Sol-gel synthesis and infrared radiation property of Li-substituted cordierite. *Ceramics International*, *39*(4), 3585–3589. https://doi.org/10.1016/j.ceramint.2012.10.185

Advanced Ceramics Progress: Vol. 10, No. 1, (Winter 2024) 22-33

Materials and Energy Research Center
MERC

Contents lists available at ACERP

Advanced Ceramics Progress

Journal Homepage: www.acerp.ir

**Original Research Article**

# Physical, Mechanical, and Microstructural Characteristics of Al-MMCs Incorporating Zirconium Diboride Particles Fabricated by Warm Equal Channel Angular Pressing Method

Hossein Jafari [a], Masoud Rajabi [b,*], Mehdi Montazeri-Pour [c]

[a] *PhD Candidate, Department of Materials Science & Engineering, Faculty of Technology and Engineering, Imam Khomeini International University (IKIU), Qazvin, Iran.*
[b] *Associate Professor, Department of Materials Science & Engineering, Faculty of Technology and Engineering, Imam Khomeini International University (IKIU), Qazvin, Iran.*
[c] *Assistant Professor, Department of Chemical and Materials Engineering, Buein Zahra Technical University (BZTE), Buein Zahra, Qazvin, Iran.*

* Corresponding Author Email: m.rajabi@eng.ikiu.ac.ir; masoudrajabi@yahoo.com (M. Rajabi) URL: https://www.acerp.ir/article_208071.html

*ARTICLE INFO*

*Article History:*
Received: 23 December 2023
Revised: 15 March 2024
Accepted: 07 September 2024

*Keywords*:
Al Metal Matrix Composites,
Mechanical Milling,
Equal Channel Angular Pressing,
Physical Properties,
Zirconium Diboride Ceramic Particles,
Microstructural Analysis

*ABSTRACT*

This study evaluated the influence of mechanical milling time on the physical, mechanical, and microstructural properties of Al metal matrix composites (MMCs) incorporating $ZrB_2$ ceramic reinforcement. The mixing powders of aluminum with zirconium diboride were mechanically milled at different times. Then, the achieved composite powder was heated, compacted, and turned into bulk material by equal channel angular pressing (ECAP) at 250°C. SEM micrographs indicated that the size of the obtained particles decreases by increasing the mechanical alloying time by up to 18 hours. However, the particle size has increased after this time. The average size of fine particles reached 823nm using mechanical alloying for 18 hours, while coarse particles were 8µm. The size calculation of crystallites using XRD examination implied that the rate of crystallite size reduction after 12 hours of mechanical alloying is gradually reduced and reached its lowest level after 18 hours. Then, increasing the mechanical alloying time led to an increase in the size of the crystallites and a decrease in the lattice strain. The microstructure of resultant bulk composites has been characterized by optical microscopy (OM) and SEM. The bulk composite samples processed by the ECAP method, with an optimum amount of $ZrB_2$ (5 wt.%), had a relative density, hardness, shear yield stress, and ultimate shear strength of 99.3%, 170 HV, 125 MPa and 151 MPa, respectively, utilizing powders which were mechanically milled for 24 hours.

https://doi.org/10.30501/acp.2024.431922.1143

## 1. INTRODUCTION

The preparation of materials with excellent strength and flexibility has always been the interest of various researchers worldwide. Metal matrix composites (MMCs) are materials composed of one or more metallic elements as matrix and reinforcement. The synthesis of MMC powder is performed in different ways. Mechanical alloying is one of the production methods of MMC powder, which occurs through the reaction between the surfaces of reactive materials. Other

Please cite this article as: Jafari, H., Rajabi, M. & Montazeri-Pour, M. (2024). Physical, Mechanical, and Microstructural Characteristics of Al-MMCs Incorporating Zirconium Diboride Particles Fabricated by Warm Equal Channel Angular Pressing Method, *Advanced Ceramics Progress*, 10(1), 22-33. https://doi.org/10.30501/acp.2024.431922.1143

2423-7485/© 2024 The Author(s). Published by MERC.
This is an open access article under the CC BY license (https://creativecommons.org/licenses/by/4.0/).

conventional methods cannot produce powders of metal composites, intermetallic compounds, etc., fabricated by this technique (Chak et al., 2020; Sharma et al., 2024). In recent years, aluminum-based composites have generally attracted the attention of several researchers owing to their low weight and high corrosion resistance to the harsh environment (Bhoi et al., 2019; Gajević et al., 2022). The use of these composites in the automotive industry, aerospace industry, and metal structures is progressive (Bhat et al., 2021; Chandel et al., 2021; Gajević et al., 2022). Strength is the most essential factor in the selection of these composites (Lakshmikanthan et al., 2022). The production of aluminum composites using the mechanical alloying method has been widely investigated (Erturun et al., 2021; Hamilton et al., 2021). The reinforcement of aluminum-based composite with secondary phase particles such as oxides, carbides, borides, and nitrides makes a suitable combination of physical and mechanical properties of both phases of the composites. Furthermore, the amount, size, and distribution of secondary phase particles determine the main properties of the composite (Diler and Ipek, 2012). $ZrB_2$, as a reinforcing phase with a very high melting temperature of 3250°C, high strength and hardness, chemical stability, and suitable electrical conductivity, has been the focus of many researchers in fabricating metal matrix composites. Pure $ZrB_2$ is brittle, and its combination with a soft metal could improve its mechanical and corrosion properties (Kumar and Kumar, 2022). Combining this ceramic material with ductile materials could result in composites with high strength and toughness (Kumar et al., 2021).

The severe plastic deformation (SPD) techniques cause changes in its mechanical and microstructural properties by applying a very high strain to the metal matrix composite (Brodova et al., 2021; Montazeri-Pour et al., 2014). The initial and final cross-section areas generally do not vary during straining in these processes (Montazeri-Pour et al., 2015a). Different methods of severe plastic deformation have been carried out. A few of its common types are equal channel angular pressing (ECAP) (Vishnu et al., 2020), high-pressure torsion (HPT) (Edalati and Horita, 2016), and accumulative roll bonding (ARB) (Ebrahimi and Wang, 2022), etc. (Faraji et al., 2018; Montazeri-Pour et al., 2015b). The ECAP process, as shown in Figure 1, is one of the most common methods of extreme plastic deformation, in which the sample is passed through an angular die, and the strain applied to the sample creates an ultrafine grain (UFG) microstructure. Improving mechanical properties results from creating a UFG microstructure using this intense plastic deformation (Montazeri-Pour et al., 2014).

The aim of this study is to evaluate the properties of the aluminum−zirconium diboride metal matrix composites with UFG structure obtained by the mechanical alloying process, where different times of milling have been considered to determine the optimal time required to attain the desired mechanical and physical properties as well as the formation of a UFG structure. Then, the bulk samples were obtained using the warm ECAP method, and their mechanical properties and microstructure were examined by performing mechanical tests, optical microscopy and SEM observations.

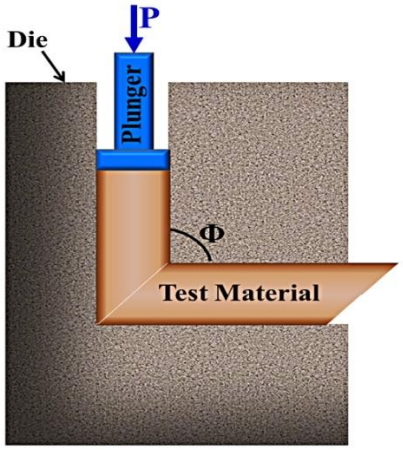


**Figure 1.** A schematic of the pressing method in ECAP die

## 2. MATERIALS AND METHODS

### 2.1. Initial Materials

The starting materials applied in this study were aluminum powders (99 wt.% purity and mean particle size (D) <20µm) and $ZrB_2$ (99 wt.% and D <5µm), which were purchased from the Chinese company of Jiaozuo Huasu Chemical Co.

SEM micrographs related to pure Al powder and primary $ZrB_2$ powder are given in Figure 2.

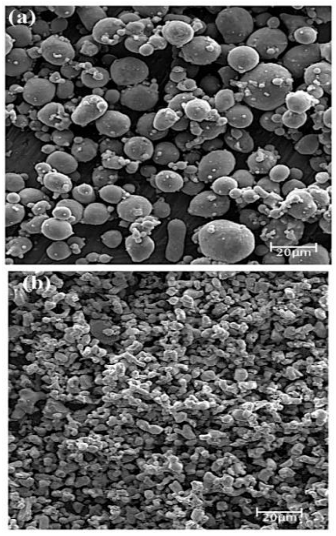


**Figure 2.** SEM images for (a) pure aluminum powder and (b) pure zirconium diboride powder

### 2.2. Production of Composite Powders

Pure aluminum powder and a mixture of 5 wt.% $ZrB_2$ plus pure aluminum powders were milled at room temperature under an argon atmosphere for 1, 6, 12, 18,

and 24 hours using a planetary ball mill with a capacity of 200ml and a rotation speed of 360rpm. The container was made of hardened steel, and the balls used in this process were made of stainless steel.

The total powder weight for this process was 20g, and the weight ratio of balls to powder was 1:15. Stearic acid (2 wt.%) was used as a process control agent (PCA) to prevent excessive cold welding of powder particles. The numbers, weights, and sizes of the balls are given in Table 1.

**TABLE 1.** Specifications of the balls used in the mechanical alloying process for the synthesis of Al-$ZrB_2$ MMC powder

| Diameter (mm) | Weight (g) | The number of balls |
|---|---|---|
| 5 | 0.65 | 30 |
| 8 | 2.09 | 20 |
| 10 | 4.02 | 15 |
| 13 | 8.96 | 13 |
| 20 | 32.52 | 2 |

### 2.3. Compaction of Composite Powders

Bulk samples were produced using the warm ECAP method in a die with an angle of Φ=90º. For this purpose, the desired powder was first placed in a copper sheath, as illustrated in Figure 3. The powder sheath in the copper tube was performed to reduce the friction of the sample with the mold and prevent the powder's dispersion during compaction. The average applied pressure was 20 tons/cm$^2$, the punch movement rate was 1.5 mm/s, and the working temperature was 250°C. The mold's inlet and outlet channels diameter was 12.70mm, and the lubricant used was $MoS_2$ powder.

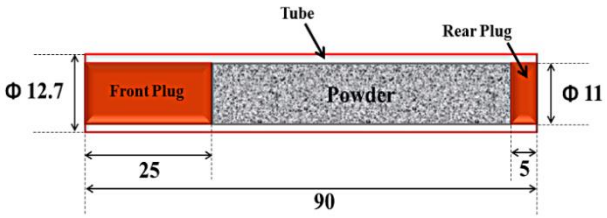


**Figure 3.** The copper sheath used in the compaction of powder by the warm ECAP method

### 2.4. Characterization of Produced Samples

Scanning electron microscopy (SEM) and optical microscopy (with a polarized camera) were used to examine the microstructure. An X-ray diffraction (XRD) test is utilized to identify the phase. Williamson-Hall Equation was used according to the following formula to evaluate the size of crystallites and lattice strain:

$$\beta\cos\theta = \frac{k\lambda}{D} + 4\varepsilon \sin\theta \quad (1)$$

where θ indicates the diffraction angle of the peak, β denotes the width of the peak at half of the maximum height, and λ presents the X-ray wavelength.

The Archimedes equation was used according to the Equation 2 to measure the density of the samples (ASTM B311-22, 2022):

$$\rho = \frac{W_{air}\left[\rho_{water} - 0.0012\right]}{0.99983\left[W_{air} - W_{water}\right]} + 0.0012 \quad (2)$$

where $W_{air}$ and $W_{water}$ represent the weight of the sample in air and in distilled water, respectively. The density ratio ($\rho_{air}/\rho_{water}$) is set to 0.0012 (Gao et al., 2021).

The samples used for the shear punch test were cut from a longitudinal section with a dimension ratio of H/D=1.5 (Figure 4 (a)), and then they were polished with soft sandpaper. The shear punch test device used was Datek, and the surface of the device jaw was lubricated to prevent friction between the jaw and the sample.

First, the samples were cut transversely from the middle part to perform the Vickers micro-hardness (HV) test on the samples (Figure 4 (b)), and the hardness was taken from different points using a Bohler micro-hardness tester with a load of 25, 120, 200, and 400gf. Finally, sandpaper 600 was used to prepare the surface of the samples to check the hardness more closely.

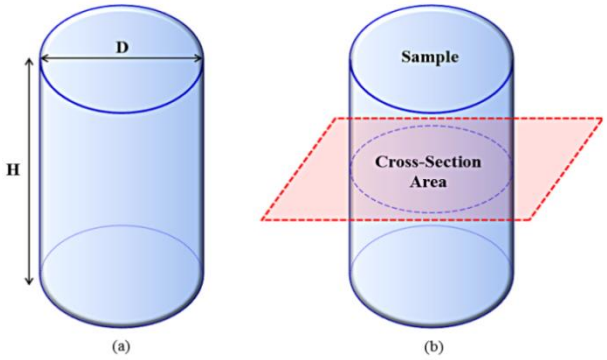


**Figure 4.** Cut samples prepared for use in (a) shear punch test and (b) Vickers micro-hardness (HV) test

## 3. RESULTS AND DISCUSSION

### 3.1. Powders Characteristics

#### 3.1.1. X-Ray Pattern of Powders

XRD experiment was performed on samples at various times. The XRD of pure Al and Al-$ZrB_2$ powders mechanically milled from 1 hour to 24 hours is given in Figures 5 and 6, respectively.

As shown in Figure 5, the peaks related to (100), (200), (220), and (311) aluminum planes appeared at the diffraction angles of 38.463°, 44.723°, 65.073°, and 78.183°, respectively. In Figure 6, the (0001) plane appeared at an angle of 36.573° for the resulting Al-5wt.% $ZrB_2$ MMC powder in addition to the mentioned planes.

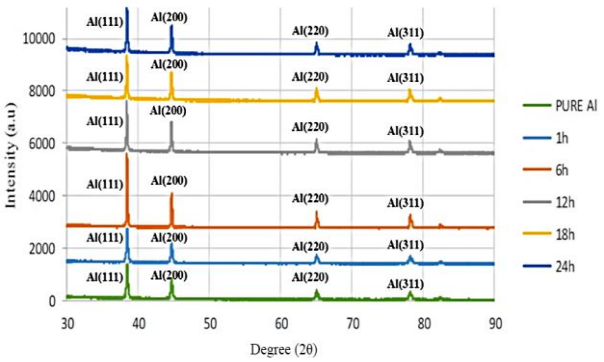


**Figure 5.** XRD of pure Al powder samples milled for 1, 6, 12, 18 and 24 hours

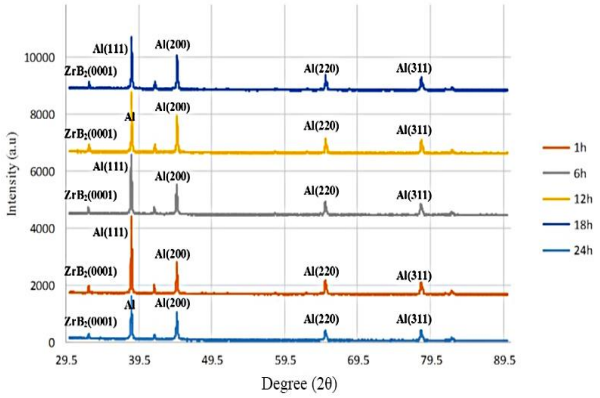


**Figure 6.** XRD of composite powder samples of Al-$ZrB_2$ (5wt.%) milled for 1, 6, 12, 18 and 24 hours

The possible reason for the peak appearance of the active (0001) plane of the hexagonal $ZrB_2$ structure is due to the lower energy of these planes compared to the aluminum FCC structure. In addition, the emergence of this peak is also likely due to the high percentage of $ZrB_2$ with a hexagonal structure (5% by weight). The peak of the reinforcing material is not observable in lower amounts (less than 1% by weight) due to the smaller size of the particles and their low dispersion compared to the matrix powder (Yue et al., 2017). A noteworthy point in the X-ray diffraction analysis of the samples is the absence of the aluminum oxide ($Al_2O_3$) peak in the graph, which is consistent with previous studies (Zhang et al., 2016).

Crystallite size and lattice strain were measured, and an analysis was performed on the samples using the Williamson-Hall formula, Equation (1). According to Figure 6, increasing the milling time leads to eliminating or reducing the intensity of additional peaks. Figure 7 shows the change in the position of the peaks relative to those of the initial samples during one up to 24h mechanical alloying. According to Figure 7, the peak angle has changed and is inclined to the left with the increase in the milling time due to the rise in the dissolution of the secondary phase. The diffusion of $ZrB_2$ into the aluminum lattice and its dissolution could be the reason for this issue. This phenomenon is consistent with the findings of other researchers (Patra et al., 2016; Suryanarayana, 1999). As shown, the intensity of the peak increased after 6 hours, and then the intensity of the peak decreased, but its width increased.

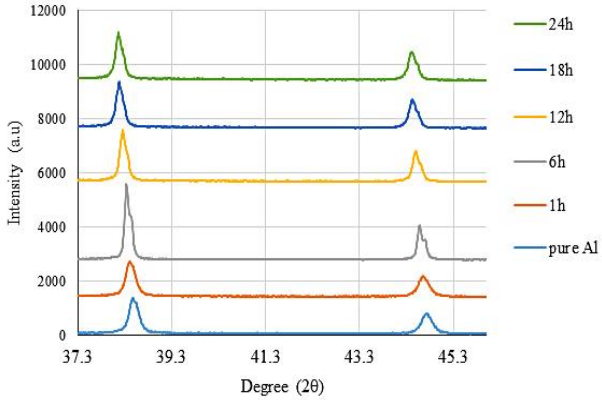


**Figure 7.** The changes in the position of peaks by increasing milling time for a mixture of pure Al and 5wt.% $ZrB_2$ powder

The graph of crystallite size and lattice strain of the powder samples is illustrated in Figure 8. The size of the crystallites decreased with the increase of milling time, and the lattice strain (calculated by the Williamson-Hall relation) increased. The equilibrium point of the curve means the time as the increase rate of the lattice parameter is declined, which specifies the equilibrium time of the two samples. This increased rate may be considered when finding the optimal time.

The change in the shape of powder particles during milling increases crystal defects such as point defects and dislocations. Defects increase the lattice strain and its internal energy and instability. The dislocations arrange themselves into a lower energy state, leading to low-angle boundaries forming. In longer milling times, the misalignment angle between the sub-grains increases due to more plastic deformation and more dislocations, and their boundaries become high-angle boundaries. Thus, the sub-grains become sub-micron grains. In addition, the size of crystallites for Al-$ZrB_2$ MMC powder is smaller than that of Al powder for each milling time, which could be due to the high hardness of $ZrB_2$ particles, reducing crystallite size during milling and facilitating the formation of nano-crystalline particles. In general, the decrease in the size of the crystallites with the increase in the milling time may be attributed to the generation and propagation of dislocations due to severe plastic deformation.

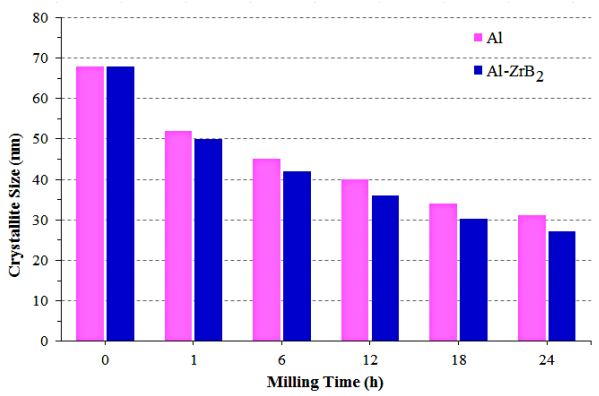


(a)

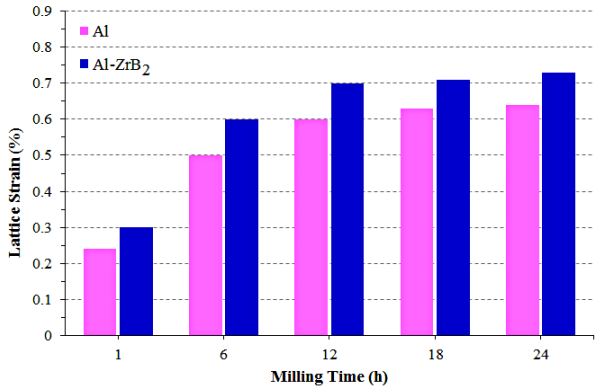


(b)

**Figure 8.** Changes in (a) size of crystallites and (b) lattice strain for Al and Al-5wt.% $ZrB_2$ MMC powders in terms of milling time at 1, 6, 12, 18 and 24 hours

In addition, the lattice strains increased up to 24 hours for both powders. This issue may be caused by dislocations, impurities, and other lattice defects during milling. Milling for more than 18 hours does not significantly affect the strain level. In addition, the lattice strain for each milling time is higher for the metal matrix composite than pure Al due to the presence of $ZrB_2$. The diffusion of $ZrB_2$ in the Al lattice and its interaction with dislocations may have increased the density of dislocations and then enhanced the strain in the particles.

### 3.1.2. The Microstructure of Powders

SEM images related to pure aluminum and Al-5wt.% $ZrB_2$ MMC powders resulting from the mechanical alloying process are shown in Figures 9 and 10, respectively.

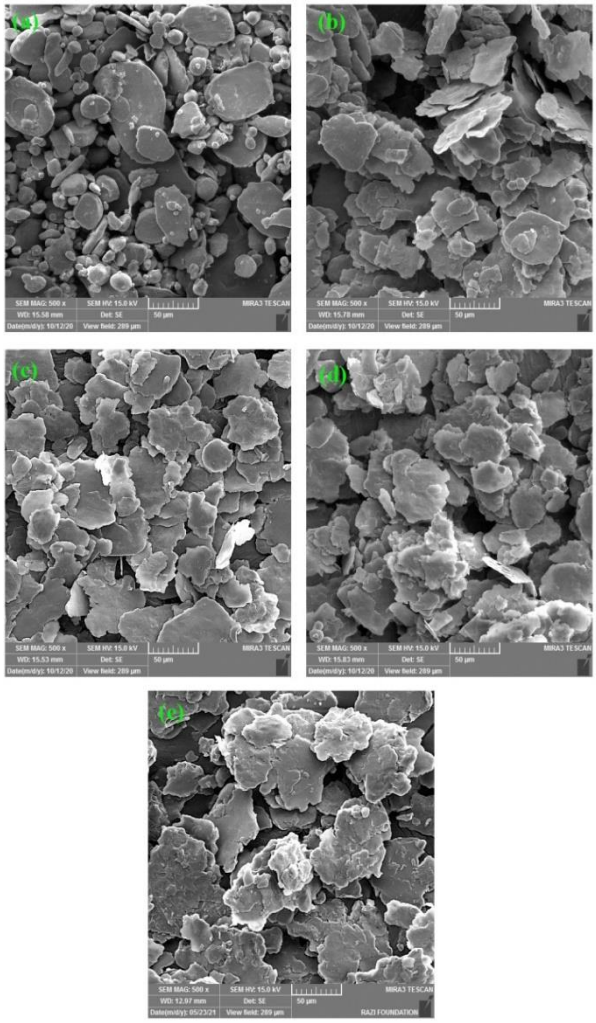


**Figure 9.** SEM images for samples of pure aluminum powder obtained from milling for (a) 1 hour, (b) 6 hours, (c) 12 hours, (d) 18 hours, and (e) 24 hours

The particle size decreased with increasing milling time. However, a more homogeneous structure was obtained by increasing the time to 12 hours. The dominant phenomena in the process of mechanical alloying are cold welding between particles and their fractures. In the early stages of milling (up to 6 hours), cold welding is the dominant phenomenon due to the softness of the particles. As a result, particle size is expected to increase, and the average particle size at this stage is 16µm. The phenomenon of fracturing the particles leads to their refinement after this stage, and along with the hardening of the particles, this phenomenon reaches its maximum value at 18 hours (Figure 10 (c) and (d)), which could be due to the balance of the two mentioned phenomena. Meanwhile, fine particles have taken up most of the powder volume, but some coarse particles are still visible in the structure. The average size of the refined grains at this stage has reached 823nm, and the coarse grains have reached 8µm. The 18

hours of mechanical alloying could be the optimum time to obtain a homogeneous microstructure. The determining mechanisms were in balance at this stage; however, after this stage, an average increase in the size of the particles was seen (Figure 10 (e)).

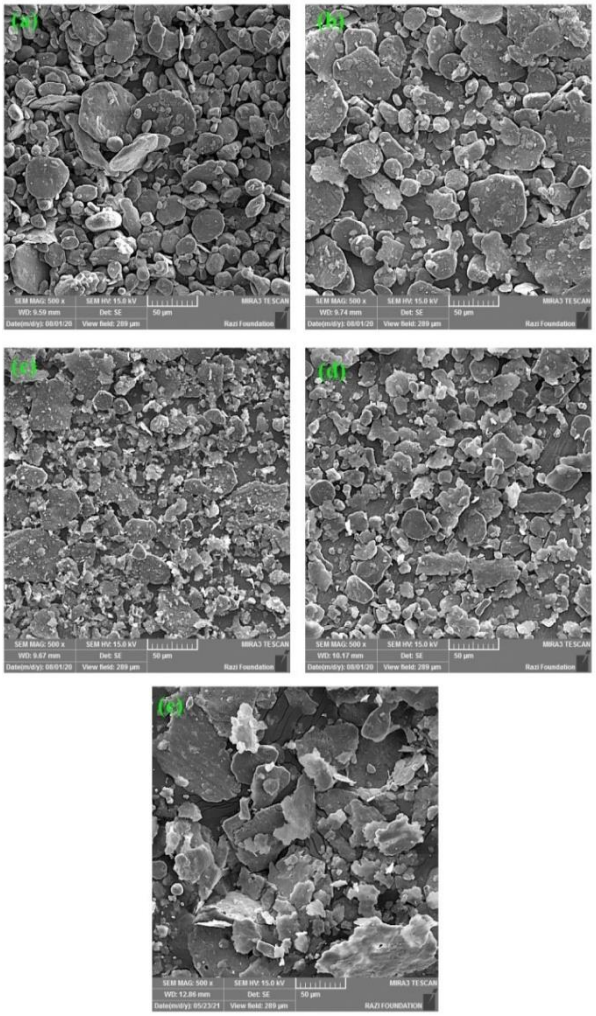

**Figure 10.** SEM images of Al-$ZrB_2$ MMC powders obtained from mechanical alloying of pure Al and 5wt.% $ZrB_2$ mixture powders for (a) 1 hour, (b) 6 hours, (c) 12 hours, (d) 18 hours and (e) 24 hours

The formation of spangle-shaped particles (Figure 11) after 12 hours of pure aluminum powder milling is observed by SEM in the microstructure of the samples. The reason for this could be the asymmetric accumulation of hardened particles and the cold welding of aluminum particles.

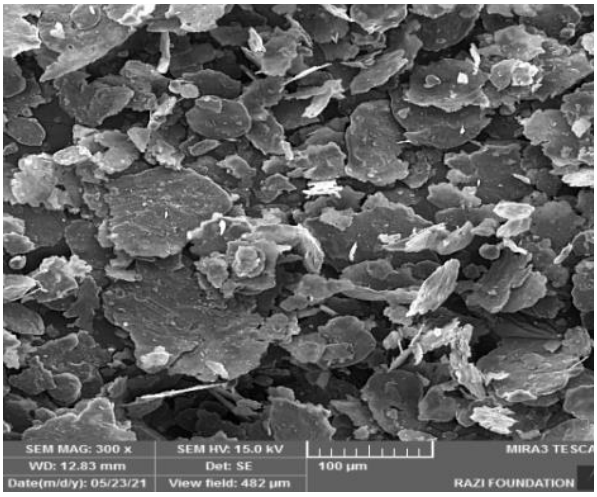


**Figure 11.** SEM images of milled aluminum powder representing the formation of spangle-shaped particles after 12 hours of milling

### 3.1.3. The Effect of Milling Time on Particle Size

Figure 12 demonstrates the size of Al particles and Al-$ZrB_2$ MMC powder obtained from mechanical alloying in terms of time. Increasing the time of mechanical alloying up to 12 hours has led to a significant reduction in the size of the particles. However, no significant reduction in the size of the particles has been achieved after this time. Increasing the mechanical alloying to more than 18 hours led to an increase in the particle size, indicating that 18 hours is the time to reach a stable state. The cold welding and particle fracture reach equilibrium (Maurice and Courtney, 1994). As shown, the slope of the variations between different milling times is higher for Al-$ZrB_2$, indicating that the addition of 5% $ZrB_2$ by weight has a significant effect on reducing the particle size by milling.

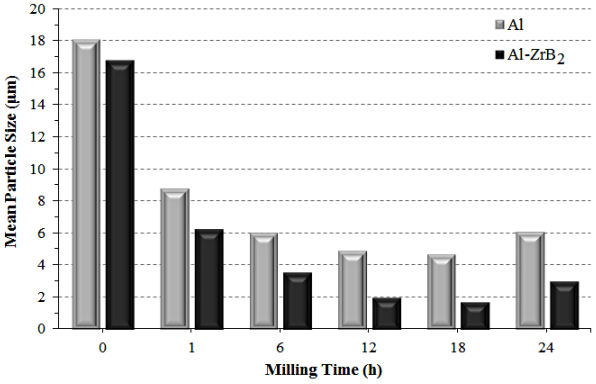


**Figure 12.** The effect of milling time on the particle size of pure Al and Al-$ZrB_2$ powders

## 3.2. Characteristics of Samples Subjected to ECAP

### 3.2.1. Physical Features of Bulk Samples

The warm ECAP method was used at 250°C to manufacture bulk pure aluminum and composite samples

from powders obtained by the mechanical alloying process. The consolidation of the 1-hour milled powders could not be performed, and the sample was incapable of bulking. The relative density and porosity percentage of the resulting bulk samples are given in Figure 13. As the milling time increased further, the porosity percentage of the resulting samples decreased. Activating dynamic recovery by increasing the milling time eliminates the effect of work hardening and causes new particles to start the densification process. This issue leads to the placement of a larger volume of particles in the grain boundaries, and the relative porosity of the samples decreases after ECAP (Ashwath and Xavior, 2014).

### 3.2.2. X-Ray Pattern of Bulk Samples

XRD patterns of bulk pure Al samples created by applying the ECAP process on the powders milled at various times of 6 to 24 hours are represented in Figure 14. As shown, increasing the initial milling time has a significant increase in the intensity of the peaks appeared in the bulk samples. The appearance of a new peak related to the (221) plane indicates the effect of the applied strain due to severe plastic deformation compared to the initial powder samples.

The X-ray diffraction patterns of the bulk composite obtained from applying ECAP on Al-$ZrB_2$ powder are shown in Figure 15. The intensity of the peaks has reached its maximum value for samples that have been mechanically alloyed for up to 12 hours, and then their intensity has decreased, but the width of the peaks has increased. After 18 hours, the trend of reducing the size of the crystallites stopped, and with additional milling, no noticeable changes could be seen in their size. The time of 12 hours of milling is considered the turning point and the time after which the rate of particle size reduction slows down and reaches a stable state. The increase in grain boundary energy, which results from very high applied strain, prevents the particles from fracture, and the grain boundaries act as places for the accumulation of dislocations. Dynamic recovery has occurred here, resulting in a decrease in particle energy, and as a result, particle refinement has been stopped (Montazeri-Pour et al., 2014).

The diffraction lines of $ZrB_2$ disappear due to the decrease in the size of $ZrB_2$ particles to the sub-micron size with the increase of mechanical alloying time. This issue is associated with the apparent change of the Al peak towards lower angles. Milling for more than 18 hours leads to the broadening of Al peaks and a decrease in their intensity, which indicates a reduction in the size of the crystallites and the accumulation of heterogeneous strain in the material (Zhang et al., 2016).

As mentioned, the appearance of new peaks in the samples consolidated by the ECAP method compared to the original powder samples (Figures 5 and 6) is definitely due to the high strain applied by the severe plastic deformation process, leading to the activation of new slip planes.

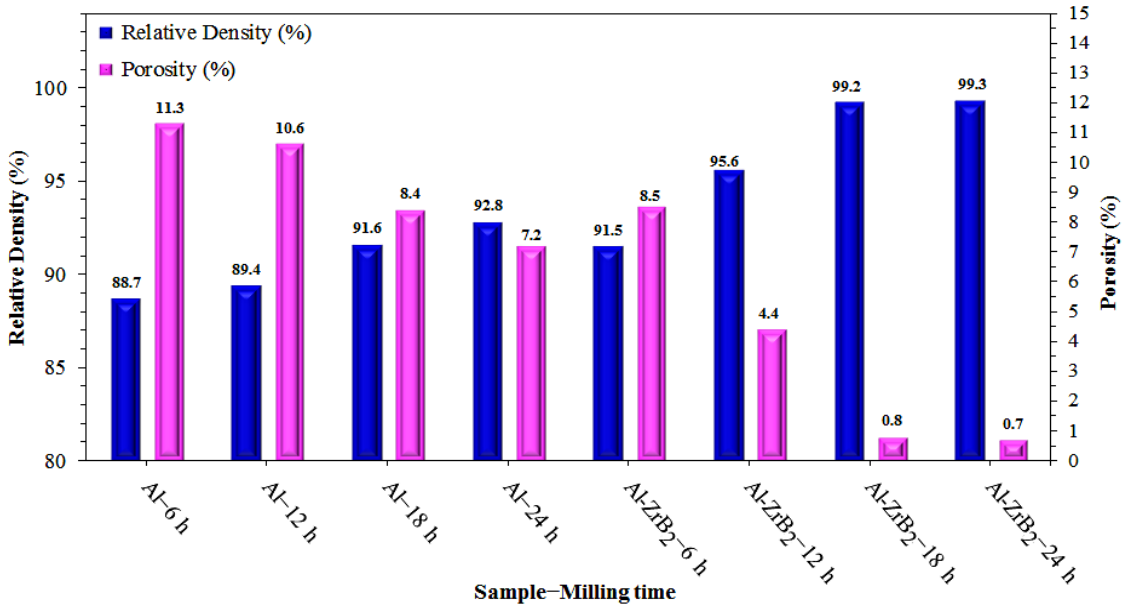


**Figure 13.** The density and the porosity of the bulk samples made by applying ECAP on the powders milled at 6, 12, 18, and 24 hours

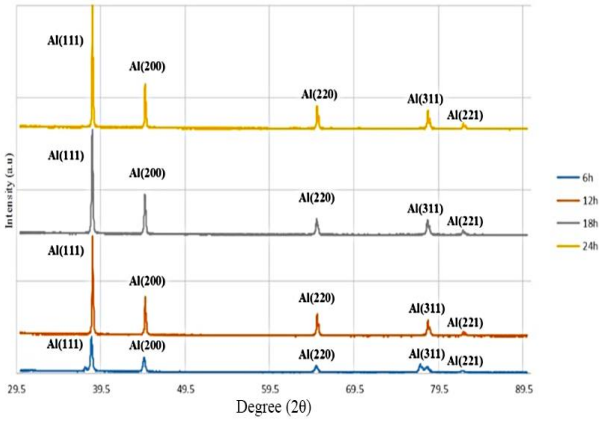


**Figure 14.** XRD diagrams of bulk pure aluminum samples fabricated by the applying ECAP process on powders resulting from milling for six up to 24 hours

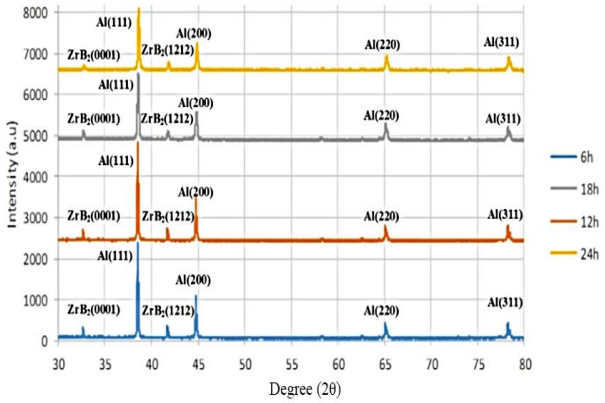


**Figure 15.** XRD of bulk Al-$ZrB_2$ samples produced by applying ECAP on powders resulting from mechanical alloying for six up to 24 hours

Figure 16 shows the changes in crystallite size and lattice strain for the bulk samples obtained by applying the ECAP process to pure Al and Al-$ZrB_2$ powders milled at varying times.

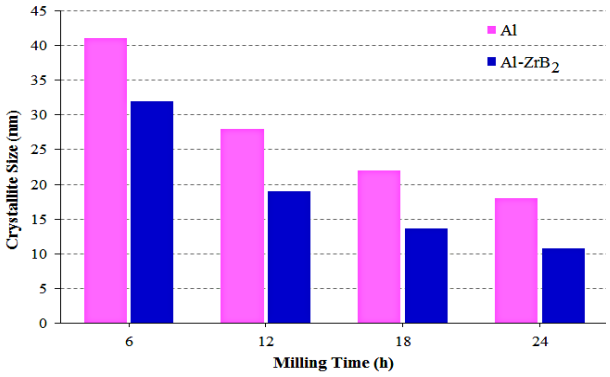


(a)

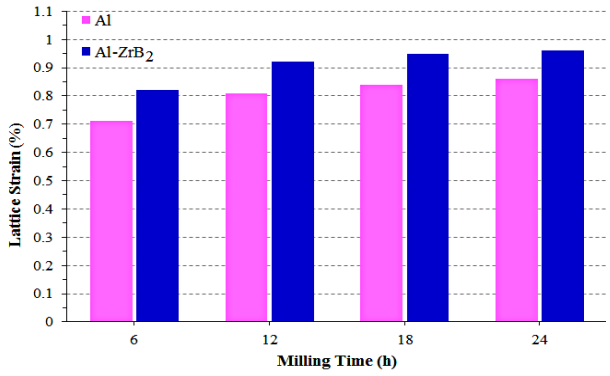


(b)

**Figure 16.** Column charts of (a) crystallite size and (b) lattice strain for the bulk pure Al and Al-$ZrB_2$ samples obtained from powders milled at various times of 6 hours up to 24 hours

As shown in Figure 16, the size of the crystallites of Al-5wt.% $ZrB_2$ MMC is finer than that of Al. In addition, the Al-$ZrB_2$ MMC sample obtained a higher lattice strain than the pure aluminum sample, and 12 hours of milling could be chosen as the turning point of the crystallite size reduction curve. The rate of crystallite size reduction decreased after 12 hours and remained almost constant after 18 hours. Hence, 18 hours could be selected as the optimum time for milling.

### 3.2.3. Microstructure of Bulk Samples

The microstructure obtained by optical microscopy for the Al and Al-$ZrB_2$ samples consolidated by ECAP is given in Figures 17 and 18, respectively. Visible holes in the obtained microstructure (Figure 17) result from burning impurities and electro-etching of the surface of the samples. All microstructures have fine precipitates in the matrix, which are finely dispersed throughout the grain boundaries in the structure of Al, and thus, homogeneity of composites increases (Asadipanah and Rajabi, 2015; Mohanavel et al., 2020). Herein, $ZrB_2$ particles appeared as spherical, angular, sub-angular, and scaly forms and distributed without forming agglomerates into the Al matrix (Alem et al., 2020b). Micrographs of an Al sample consolidated by the ECAP method with random morphology are shown in Figure 17 (a) up to (d). Al phase precipitates within and outside of grains make up the Al matrix, indicated with a white color (Alem et al., 2020a). A homogeneous dispersion of $ZrB_2$ particles significantly inhibits the development and expansion of large grains, as shown in Figure 18 (a) up to (d). Smaller particles have a stronger fixing impact on boundaries than larger particles. Dendritic structures indicate that $ZrB_2$ particulates are evenly distributed and the porosity is low, which motivates the development of a structure with more $ZrB_2$ in the Al matrix. Figure 18(d) shows that the dendrites are greatly enlarged.

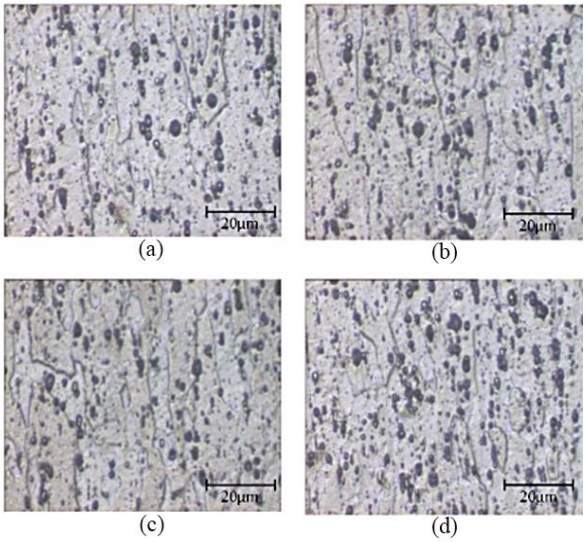


**Figure 17.** The optical microscopy images for the ECAP processed samples of pure Al produced by using powders milled for (a) 6 hours, (b) 12 hours, (c) 18 hours, and (d) 24 hours

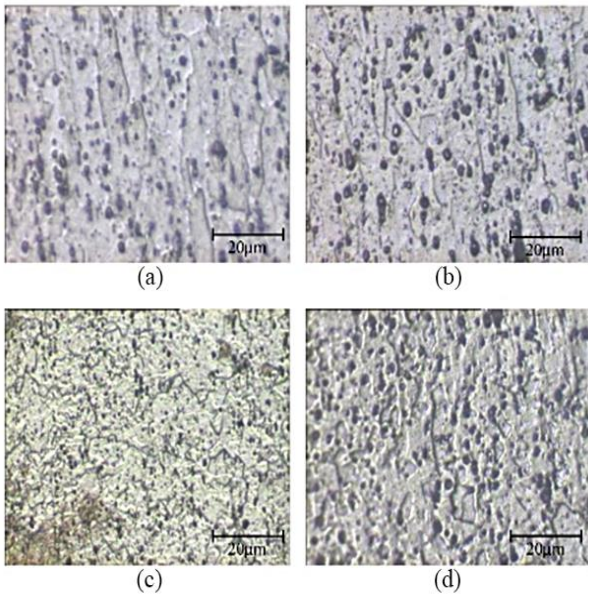


**Figure 18.** The optical microscopy images obtained for bulk samples of Al-$ZrB_2$ produced by using powders resulting from mechanical alloying for (a) 6 hours, (b) 12 hours, (c) 18 hours, and (d) 24 hours

The submicron structure obtained for the composite material is much more homogeneous than pure Al. The presence of hard ceramic particles and the accumulation of dislocations in the sub-grain and grain boundaries are the main motives for the UFG formation after the ECAP process. The obtained SEM images for bulk samples of Al-$ZrB_2$ milled at 6, 12, 18, and 24 hours are given in Figure 19. As can be seen, most grains contained small amounts of the secondary phase. Few grains contain cellular microstructures from the secondary phase, and their formation may have resulted from the secondary phase's sedimentation and agglomeration in the dendritic structure.

The difference in grain size from the surface to the center was due to the dynamic recovery phenomenon activated at this stage. As shown in Figure 19 (b), increasing the milling time by up to 12 hours has led to the diffusion of $ZrB_2$ particles in the grain boundaries. As shown in Figure 19 (d), increasing the mechanical alloying time up to 24 hours has led to larger grain sizes due to dynamic recovery as the dominant mechanism at this stage. The particles might not have had time to dissolve, so they diffused more at the grain boundaries. The increase in milling time and the crushing of aluminum particles decrease the amount of $ZrB_2$ in the grain boundaries, which is the reason for the dominance of the solid dissolution process in the more extended times of mechanical alloying. In addition, increasing the milling time leads to an increase in temperature, which increases the possibility of oxidation of aluminum. Finally, the defects created during the mechanical alloying time of 24 hours can be observed in Figure 19 (d).

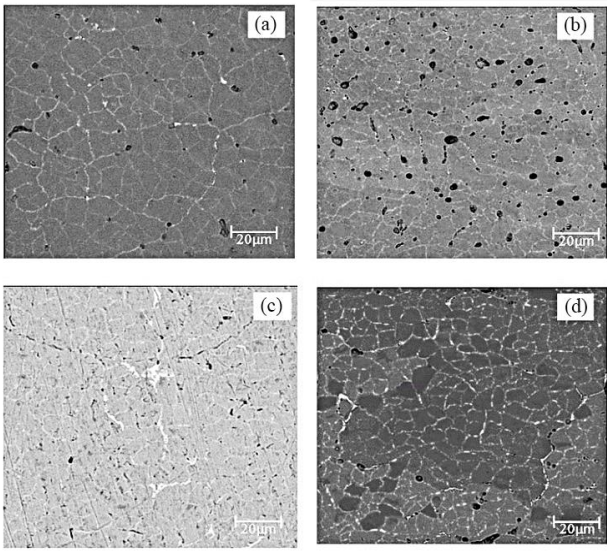


**Figure 19.** SEM images for ECAP processed bulk samples of Al-$ZrB_2$ produced by using powders resulting from mechanical alloying for (a) 6 hours, (b) 12 hours, (c)18 hours, and (d) 24 hours

As shown, the desired homogeneous microstructure corresponds to the milling time of 18 hours (Figure 19 (c)), indicating that the grains have completely refined at this stage. Therefore, the desired microstructure and, consequently, the desired mechanical properties are expected to be related to this case of mechanical alloying.

### 3.2.4. Micro-hardness of Bulk Samples

The effect of mechanical alloying time on the hardness properties of the bulk samples was evaluated using a micro-hardness tester. The results can be

observed in Figure 20, showing that the resulting micro-hardness increases at a high rate with the rise of mechanical alloying time up to 12 hours, but after this time, its rate is reduced until 24 hours when the trend of its increasing rate reaches its lowest level. Two active mechanisms could explain the increase in hardness of pure Al samples and Al-$ZrB_2$ MMC samples. One reason is the change in grain size and, consequently, the rise in grain boundaries, which in turn increases the hardness. The other mechanism is the increase in the density of dislocations due to the plastic deformation of particles during mechanical alloying and ECAP processes, which is known as the work hardening phenomenon. Aside from the two active mechanisms for both pure Al and Al-$ZrB_2$ MMC, there is also increased microhardness gradients for the Al-$ZrB_2$ MMC sample due to the high hardness of $ZrB_2$ particles and the hardening resulting from the dissolution of the secondary solid phase, compared to pure Al.

The dynamic recovery mechanism in the samples is expected to affect the trend of the grain size decrement during a further increase in milling time. Consequently, the rate of hardness increase would be reduced. Hence, the upward trend of increasing hardness continues until 24 hours of milling, but its increasing rate decreases after 12 hours of milling.

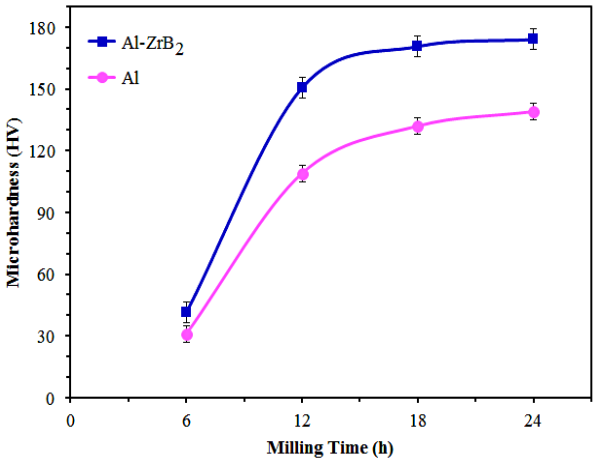


**Figure 20.** Micro-hardness (HV) changes for bulk pure Al and Al-$ZrB_2$ samples produced using powders milled for 6-24 hours

### 3.2.5. The Shear Punch Test of Bulk Samples

As summarized in column chart of Figure 21, the results of the shear punch test for ECAP-processed bulk Al-$ZrB_2$ samples indicate that the samples that have been mechanically alloyed for up to 24 hours have the highest strength due to having the minimum crystallite size.

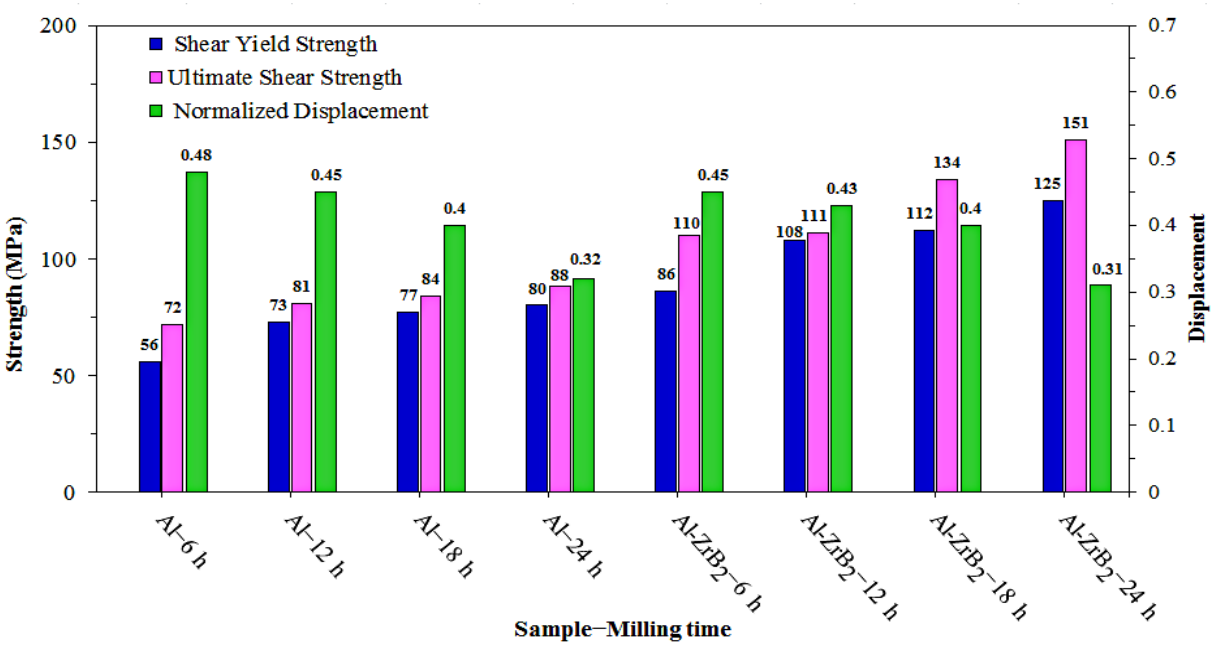


**Figure 21.** The shear punch test results of bulk samples produced by applying ECAP on pure aluminum and Al-$ZrB_2$ powders milled at different times

Conducting ECAP to compact samples causes the strength of the samples to be increased by a higher rate up to 12 hours of milling, and their strength changes slightly after that, up to 24 hours. The highest ductility is related to ECAP-processed samples produced using 6 hours of milling of pure Al and Al-$ZrB_2$ MMC powders, and the lowest ductility is related to bulk samples prepared using 24 hours of mechanical milling of both samples. This subject might be caused by the application of very high strain by the warm ECAP process (Iwahashi et al., 1996; Montazeri-Pour et al., 2014) and the work hardening phenomenon due to the deformation of

powders during the milling procedure (Suryanarayana et al., 2001).

In general, the absorption of dislocations by grain boundaries and the balance between work-hardening caused by severe plastic deformation and dynamic recovery have led to a decrease in the rate of grain size reduction (Montazeri-Pour and Parsa, 2016; Montazeri-Pour et al., 2014). Based on the calculated grain size, the rate of grain size reduction with increasing milling time was higher for Al-$ZrB_2$ MMC. The increase in the density of dislocations and their presence in the grain boundaries and the precipitation hardening resulting from Al-$ZrB_2$ MMC at higher times could lead to equilibrium or dynamic recovery. This issue is consistent with the lower grain size and the higher rate of grain size reduction of Al-$ZrB_2$ MMC compared to pure Al. The finer size of the crystallites and the increase of the lattice strain imply the grain size reduction with the increase of the milling time. The dominance of dynamic recovery over the hardening caused by the decrease in grain size can lead to the reduction of grain fracture rate. A dynamic recrystallization process and a relative increase in grain size are possible after 24 hours of milling. The border between the particles is the energy-rich area and the best area for the agglomeration of particles and the accumulation of impurities. The decrease in the density of holes in the boundary between grains shows that the energy of grain boundaries might be decreased during 24 hours of milling. In other words, a decrease in grain boundaries can have been happening, which confirms dynamic recovery at times longer than 18 hours of mechanical alloying (Alem et al., 2020b; Yadav Kaku et al., 2018).

## 4. CONCLUSIONS

Applying the warm ECAP process at 250°C on the Al-$ZrB_2$ composite powder obtained by milling for up to 24 hours improved the mechanical and physical properties of the obtained samples. The achieved microstructure became more homogeneous with the increase of the milling time. In addition, producing samples using the ECAP method significantly affected the homogeneity of the microstructure and the refinement of the grains. The milling time of 12 hours is introduced as the turning point of the mechanical alloying time. After that, the mechanical properties increased slowly, the grain size reduction rate decreased, and consequently, the microstructure homogenization rate decreased. Performing severe plastic deformation by the ECAP method on powder samples, turning them into bulk samples with this method, and increasing the mechanical alloying time improved the mechanical properties of Al-5wt% $ZrB_2$ MMC samples. However, its rate decreased after 12 hours of mechanical alloying, and finally, it reached a stable state after 18 hours, and no significant changes were observed in mechanical properties up to 24 hours. The results of the shear punch test of Al-5 wt.% $ZrB_2$ MMC samples indicated that the samples that have been mechanically alloyed for up to 24 hours had the highest strength. Therefore, the production of Al-$ZrB_2$ MMC by powder metallurgy method found a favorable result through the ECAP process for the consolidation of powders milled for 24 hours.

## ACKNOWLEDGEMENT

The authors gratefully acknowledge Imam Khomeini International University (IKIU) for providing the financial support of this work.

## Declaration of Competing Interest

The authors declared no conflicts of interest.

## REFERENCES

1. Alem, S. A. A., Latifi, R., Angizi, S., Hassanaghaei, F., Aghaahmadi, M., Ghasali, E., & Rajabi, M. (2020a). Microwave sintering of ceramic reinforced metal matrix composites and their properties: a review. *Materials and Manufacturing Processes*, Vol. *35*(3), 303-327. https://doi.org/10.1080/10426914.2020.1718698
2. Alem, S. A. A., Latifi, R., Angizi, S., Mohamadbeigi, N., Rajabi, M., Ghasali, E., & Orooji, Y. (2020b). Development of metal matrix composites and nanocomposites via double-pressing double-sintering (DPDS) method. *Materials Today Communications*, Vol. *25*, 101245. https://doi.org/10.1016/j.mtcomm.2020.101245
3. Asadipanah, Z., & Rajabi, M. (2015). Production of Al–$ZrB_2$ nano-composites by microwave sintering process. *Journal of Materials Science: Materials in Electronics*, Vol. *26*(8), 6148-6156. https://doi.org/10.1007/s10854-015-3195-9
4. Ashwath, P., & Xavior, M. A. (2014). The effect of ball milling & reinforcement percentage on sintered samples of aluminium alloy metal matrix composites. *Procedia Engineering*, Vol. *97*, 1027-1032. https://doi.org/10.1016/j.proeng.2014.12.380
5. ASTM B311-22. (2022). Standard Test Method for Density of Powder Metallurgy (PM) Materials Containing Less Than Two Percent Porosity. In: ASTM International. https://www.astm.org/b0311-17.html
6. Bhat, A., Budholiya, S., Raj, S. A., Sultan, M. T. H., Hui, D., Shah, A. U. M., & Safri, S. N. A. (2021). Review on nanocomposites based on aerospace applications. *Nanotechnology Reviews*, Vol. *10*(1), 237-253. https://doi.org/10.1515/ntrev-2021-0018
7. Bhoi, N. K., Singh, H., & Pratap, S. (2019). Developments in the aluminum metal matrix composites reinforced by micro/nano particles – A review. *Journal of Composite Materials*, Vol. *54*(6), 813-833. https://doi.org/10.1177/0021998319865307
8. Brodova, I. G., Petrova, A. N., Shirinkina, I. G., Rasposienko, D. Y., Yolshina, L. A., Muradymov, R. V.,…Shorokhov, E. V. (2021). Mechanical properties of submicrocrystalline aluminium matrix composites reinforced by in situ graphene through severe plastic deformation processes. *Journal of Alloys and Compounds*, Vol. *859*, 158387. https://doi.org/10.1016/j.jallcom.2020.158387
9. Chak, V., Chattopadhyay, H., & Dora, T. L. (2020). A review on fabrication methods, reinforcements and mechanical properties of aluminum matrix composites. *Journal of Manufacturing Processes*, Vol. *56*, 1059-1074. https://doi.org/10.1016/j.jmapro.2020.05.042
10. Chandel, R., Sharma, N., & Bansal, S. A. (2021). A review on recent developments of aluminum-based hybrid composites for automotive applications. *Emergent Materials*, Vol. *4*(5), 1243-1257. https://doi.org/10.1007/s42247-021-00186-6

11. Diler, E. A., & Ipek, R. (2012). An experimental and statistical study of interaction effects of matrix particle size, reinforcement particle size and volume fraction on the flexural strength of Al–SiCp composites by P/M using central composite design. *Materials Science and Engineering: A*, Vol. *548*, 43-55. https://doi.org/10.1016/j.msea.2012.03.066
12. Ebrahimi, M., & Wang, Q. (2022). Accumulative roll-bonding of aluminum alloys and composites: An overview of properties and performance. *Journal of Materials Research and Technology*, Vol. *19*, 4381-4403. https://doi.org/10.1016/j.jmrt.2022.06.175
13. Edalati, K., & Horita, Z. (2016). A review on high-pressure torsion (HPT) from 1935 to 1988. *Materials Science and Engineering: A*, Vol. *652*, 325-352. https://doi.org/10.1016/j.msea.2015.11.074
14. Erturun, V., Çetin, S., & Sahin, O. (2021). Investigation of microstructure of aluminum based composite material obtained by mechanical alloying. *Metals and Materials International*, Vol. *27*(6), 1662-1670. https://doi.org/10.1007/s12540-019-00583-x
15. Faraji, G., Kim, H. S., & Kashi, H. T. (2018). Chapter 2 - Severe Plastic Deformation Methods for Bulk Samples. In G. Faraji, H. S. Kim, & H. T. Kashi (Eds.), *Severe Plastic Deformation* (pp. 37-112). Elsevier. https://doi.org/10.1016/B978-0-12-813518-1.00002-3
16. Gajević, S., Miladinović, S., & Stojanović, B. (2022). Chapter 8 - Metallic nanocomposites: An Introduction. In H. Song, T. A. Nguyen, G. Yasin, N. B. Singh, & R. K. Gupta (Eds.), *Nanotechnology in the Automotive Industry* (pp. 155-161). Elsevier. https://doi.org/10.1016/B978-0-323-90524-4.00008-6
17. Gao, Q., Deane, G. B., & Shen, L. (2021). Bubble production by air filament and cavity breakup in plunging breaking wave crests. *Journal of Fluid Mechanics*, Vol. *929*, A44, Article A44. https://doi.org/10.1017/jfm.2021.890
18. Hamilton, J. D., Ramesh, S., Harrysson, O. L., Rock, C. D., & Rivero, I. V. (2021). Cryogenic mechanical alloying of aluminum matrix composites for powder bed fusion additive manufacturing. *Journal of Composite Materials*, Vol. *55*(5), 641-651. https://doi.org/10.1177/0021998320957698
19. Iwahashi, Y., Wang, J., Horita, Z., Nemoto, M., & Langdon, T. G. (1996). Principle of equal-channel angular peessing for the processing of ultra-fine grained materials. *Scripta Materialia*, Vol. *35*, 143–146. https://doi.org/10.1016/1359-6462(96)00107-8
20. Kumar, B., & Kumar, P. (2022). Preparation of hybrid reinforced aluminium metal matrix composite by using $ZrB_2$: A systematic review. *Materials Today: Proceedings*, Vol. *61*, 115-120. https://doi.org/10.1016/j.matpr.2022.04.066
21. Kumar, S. D., Ravichandran, M., Jeevika, A., Stalin, B., Kailasanathan, C., & Karthick, A. (2021). Effect of $ZrB_2$ on microstructural, mechanical and corrosion behaviour of aluminium (AA7178) alloy matrix composite prepared by the stir casting route. *Ceramics International*, Vol. *47*(9), 12951-12962. https://doi.org/10.1016/j.ceramint.2021.01.158
22. Lakshmikanthan, A., Angadi, S., Malik, V., Saxena, K. K., Prakash, C., Dixit, S., & Mohammed, K. A. (2022). Mechanical and tribological properties of aluminum-based metal-matrix composites. *Materials*, Vol. *15*(17), 6111. https://doi.org/10.3390/ma15176111
23. Maurice, D., & Courtney, T. H. (1994). Modeling of mechanical alloying: Part I. deformation, coalescence, bdand fragmentation mechanisms. *Metallurgical and Materials Transactions A*, Vol. *25*(1), 147-158. https://doi.org/10.1007/BF02646683
24. Mohanavel, V., Ravichandran, M., & Suresh Kumar, S. (2020). Tribological and mechanical properties of Zirconium Di-boride ($ZrB_2$) particles reinforced aluminium matrix composites. *Materials Today: Proceedings*, Vol. *21*, 862-864. https://doi.org/10.1016/j.matpr.2019.07.603
25. Montazeri-Pour, M., & Parsa, M. H. (2016). Constitutive analysis of tensile deformation behavior for AA1100 aluminum subjected to multi-axial incremental forging and shearing. *Mechanics of Materials*, Vol. *94*, 117-131. https://doi.org/10.1016/j.mechmat.2015.11.016
26. Montazeri-Pour, M., Parsa, M. H., Jafarian, H. R., & Taieban, S. (2015a). Microstructural and mechanical properties of AA1100 aluminum processed by multi-axial incremental forging and shearing. *Materials Science and Engineering A*, Vol. *639*, 705–716. https://doi.org/10.1016/j.msea.2015.05.066
27. Montazeri-Pour, M., Parsa, M. H., Khajezade, A., & Mirzadeh, H. (2015b). Multi-axial incremental forging and shearing as a new severe plastic deformation processing technique. *Advanced Engineering Materials*, Vol. *17*(8), 1197-1207. https://doi.org/10.1002/adem.201400467
28. Montazeri-Pour, M., Parsa, M. H., & Mirzadeh, H. (2014). Constitutive description of severely deformed metals based on dimensional analysis. *Materials Science and Technology*, Vol. *30*(6), 719-724. https://doi.org/10.1179/1743284713y.0000000424
29. Patra, A., Karak, S. K., & Pal, S. (2016). Effects of mechanical alloying on solid solubility. *Advanced Engineering Forum*, Vol. *15*, 17–24. https://doi.org/10.4028/www.scientific.net/aef.15.17
30. Sharma, S. K., Saxena, K. K., Salem, K. H., Mohammed, K. A., Singh, R., & Prakash, C. (2024). Effects of various fabrication techniques on the mechanical characteristics of metal matrix composites: a review. *Advances in Materials and Processing Technologies*, Vol. *10*(2), 277-294. https://doi.org/10.1080/2374068X.2022.2144276
31. Suryanarayana, C. (1999). Chapter 4- Mechanical alloying. In C. Suryanarayana (Ed.), *Pergamon Materials Series* (Vol. 2, pp. 49-85). Pergamon. https://doi.org/10.1016/S1470-1804(99)80050-9
32. Suryanarayana, C., Ivanov, E., & Boldyrev, V. V. (2001). The science and technology of mechanical alloying. *Materials Science and Engineering: A*, Vol. *304-306*, 151-158. https://doi.org/10.1016/S0921-5093(00)01465-9
33. Vishnu, P., Raj Mohan, R., Krishna Sangeethaa, E., Raghuraman, S., & Venkatraman, R. (2020). A review on processing of aluminium and its alloys through Equal Channel Angular Pressing die. *Materials Today: Proceedings*, Vol. *21*, 212-222. https://doi.org/10.1016/j.matpr.2019.04.223
34. Yadav Kaku, S. M., Raju, V., Bharath, K., Fuchs Godec, R., & Reddy Tiyyagura, H. (2018). Evaluation of $ZrB_2$ reinforced Al/Al alloy composite produced by powder metallurgy-vacuum arc melting technique: A unique approach. *Vacuum*, Vol. *155*, 539-545. https://doi.org/10.1016/j.vacuum.2018.06.055
35. Yue, H., Yao, L., Gao, X., Zhang, S., Guo, E., Zhang, H.,…Wang, B. (2017). Effect of ball-milling and graphene contents on the mechanical properties and fracture mechanisms of graphene nanosheets reinforced copper matrix composites. *Journal of Alloys and Compounds*, Vol. *691*, 755-762. https://doi.org/10.1016/j.jallcom.2016.08.303
36. Zhang, H., Xu, C., Xiao, W., Ameyama, K., & Ma, C. (2016). Enhanced mechanical properties of Al5083 alloy with graphene nanoplates prepared by ball milling and hot extrusion. *Materials Science and Engineering: A*, Vol. *658*, 8-15. https://doi.org/10.1016/j.msea.2016.01.076

Advanced Ceramics Progress: Vol. 10, No. 1, (Winter 2024) 34-43

Materials and Energy Research Center
MERC

Contents lists available at ACERP

Advanced Ceramics Progress

Journal Homepage: www.acerp.ir

**Original Research Article**

# Ag/Zn Codoped $TiO_2$ (AZT) Mesoporous Nanoparticles: Investigation the Optical Properties via Increasing Calcination Temperatures

Negin Ebrahimi [a], Behzad Koozegar Kaleji [b,*]

[a] *Master, Department of Materials Engineering, Faculty of Engineering, Malayer University, Malayer, Iran.*
[b] *Associate Professor, Department of Materials Engineering, Faculty of Engineering, Malayer University, Malayer, Iran.*

* Corresponding Author Email: b.kaleji@malayeru.ac.ir, bkaleji@yahoo.com (B. Koozegar Kaleji) URL: https://www.acerp.ir/article_208070.html

*ARTICLE INFO*

*Article History:*
Received: 03 June 2024
Revised: 05 August 2024
Accepted: 19 October 2024

*Keywords*:
Nanoparticles,
Ag/Zn Codoped $TiO_2$,
Photocatalytic Activity,
Band Gap,
Calcination Temperature

*ABSTRACT*

$TiO_2$ nanoparticles codoped with Ag/Zn (AZT) were prepared using a simple sol-gel method. The effect of calcination temperature on the structural, optical, and photocatalytic properties of nanoparticles synthesized at temperatures of 400, 500, and 600 °C was investigated. The synthesized nanoparticles were analyzed using various methods, including thermal analysis (TG-DTA), X-ray diffraction (XRD), spectrophotometry (UV-Vis), electron microscopy (FESEM & TEM), and surface chemical analysis (XPS). To evaluate the photocatalytic activity of the samples, the degradation of an organic solution of methylene blue (MB) was performed. The results indicated that the calcination temperature significantly affects the microstructure, optical properties, and photocatalytic activity of the samples. The crystal size of AZT nanoparticles was approximately 4.15, 8.13, and 13.6 nm, respectively, with increasing calcination temperature. The optimal condition for the photocatalytic degradation of the methylene blue solution was observed at a calcination temperature of 500 °C, with a degradation percentage of 57.9% under visible light irradiation. Additionally, the bandgap energy of AZT particles decreased from 3.06 eV to 2.25 eV as the calcination temperature increased.

https://doi.org/10.30501/acp.2024.459534.1153

## 1. INTRODUCTION

Photocatalytic degradation of toxic organic compounds has received significant attention over the past several years. Due to its strong oxidizing power, cost-effectiveness, and long-term stability against photo and chemical corrosion, $TiO_2$ is widely used in water purification technology (Savio at al., 2016, Kunnamareddy at al., 2021). Today, the photocatalytic degradation of organic compounds is a focus of interest across various industries. Titanium dioxide is one of the most effective semiconductors in this field. One notable feature is its ability to achieve complete organic mineralization under normal conditions, such as ambient temperature and pressure, making it suitable for treating wastewater containing organic pollutants. When charge carriers are available on the semiconductor surface, the holes can produce $OH^{\circ}$ radicals, which are highly reactive due to the oxidation of $OH^-$ or $H_2O$. Conversely, electrons can catch molecular oxygen to form a superoxide radical anion $O_2^{\circ -}$, which are also highly reactive (Savio at al., 2016).

$TiO_2$ exhibits remarkable stability in aqueous environments and is resilient in both acidic and alkaline solutions. It is inexpensive, recyclable, reusable, and relatively simple to produce (Vasiljevic at al., 2020, Mohammad at al., 2019). However, due to the large band

Please cite this article as: Ebrahimi, N. & Koozegar Kaleji, B. (2024). Ag/Zn Codoped TiO2 (AZT) Mesoporous Nanoparticles: Investigation the Optical Properties via Increasing Calcination Temperatures, *Advanced Ceramics Progress*, 10(1), 34-43. https://doi.org/10.30501/acp.2024.459534.1153

2423-7485/© 2024 The Author(s). Published by MERC.
This is an open access article under the CC BY license (https://creativecommons.org/licenses/by/4.0/).

gap energy of $TiO_2$, it primarily absorbs UV light, which constitutes only 3-5% of sunlight and is necessary for photocatalytic activity. Therefore, a photocatalyst activated by visible light that can utilize a larger portion of the solar spectrum is crucial for effective environmental remediation. Several competing effects limit the efficiency of the catalyst (Bellotti at al., 2023). Titanium dioxide ($TiO_2$) naturally exists in three different crystalline polymorphs: $TiO_2$ (A: Anatase), $TiO_2$ (R: Rutile), and $TiO_2$ (B: Brookite). These polymorphs differ in surface properties, crystal structure, and electronic structure. Anatase tends to transform into rutile at temperatures exceeding 450 °C (Mikrut at al., 2020). Rahmawati et. al. (Rahmawati at al., 2023) concluded that adding silver dopants to the titania structure promotes phase transformation from anatase to rutile and prevents particle growth. Rathi et. al. (Rathi at al., 2023) obtained similar results to Rahmati in their experiments. Kaleji et. al. (Kaleji at al., 2015) investigated the effect of calcination temperature ranging from 350 to 650 °C and concluded that photocatalytic activity increases with rising calcination temperature due to improved phase crystallization (Anatase and Rutile) and a reduction in band gap energy. Lal et. al. (Lal at al., 2021) explored the impact of calcination temperature from 300 to 800 °C on crystalline phases using the sol-gel method. They observed that with increasing calcination temperature, the intensity of anatase peaks decreased while the intensity of rutile peaks increased.

Much research has been done on modifying the physicochemical properties of $TiO_2$ to shift its absorption threshold to the visible region and separate the photoinduced charges (Rahimi at al., 2023). This can be achieved by coupling it to organic or inorganic dyes (Wang at al., 2016), or by modifying its surface with other semiconductors, doping it with cations, anions, or metals (Anpo at al., 2004), particularly with transition elements such as Ag (Choi at al., 1994), Au (Usha at al., 2016), among others.

Therefore, to obtain the desired photocatalyst, titania must be activated in the visible light range. Research indicates that the addition of impurities to the titania structure significantly affects its properties. The aim of this study is to investigate the effect of calcination temperature on the optical, structural, and photocatalytic properties of titania nanoparticles doped with silver and zinc.

## 2. MATERIALS AND METHODS

### 2.1. Raw Materials

Tetrabutyl orthotitanate (TBT = $Ti(OC_4H_9)_4$, purity: 99%), Ethanol (EtOH=$C_2H_5OH$, purity: 99%), Nitric acid ($HNO_3$, purity: 65%), Zinc nitrate ($Zn(NO_3)_2$, purity: 99%), and Silver nitrate ($AgNO_3$, purity: 99%) were used in this study. To measure the photocatalytic activity of the samples, methylene blue was used as the color pollutant. All raw materials used in this research were purchased from Merck company with high purity (>98-99%).

### 2.2. Experimental Procedure

Titania sol was prepared as illustrated in Figure 1. First, 28.8 mL (approximately 0.5 mol) of ethanol was poured into a 100 mL beaker. Then, 3.42 mL (0.01 mol) of the alkoxide precursor (TBT: Tetra n-butyl orthotitanate) was slowly added to the ethanol and stirred for 60 minutes. Next, 0.47 mL (0.0105 mol) of nitric acid (HNO3) was added to the solution. After stirring for 30 minutes, 1.8 mL (0.1 mol) of distilled water was introduced. Following the addition of water, stirring continued for 1-2 hours, and to complete the hydrolysis process, the TiO2 yellow sol was kept at room temperature (25 °C) for 24 hours. Subsequently, the samples were transferred to an oven and dried at 100 °C for 10 hours. The addition of ingredients at each step was carried out slowly and continuously. The samples were calcined at temperatures of 400, 500, and 600 °C in an electric furnace. Following this, two solutions of silver and zinc were added with appropriate content (1 mmol = 0.17 g AgNO3 and 1.5 mmol = 0.3 g Zn(NO3)2) to the TiO2 sol. The prepared solution was stirred on a magnetic stirrer for 1 hour and then dried to form a gel. Finally, the dried gel was placed in the furnace and calcined at different temperatures (400, 500, and 600 °C) to synthesize the desired nanoparticles.

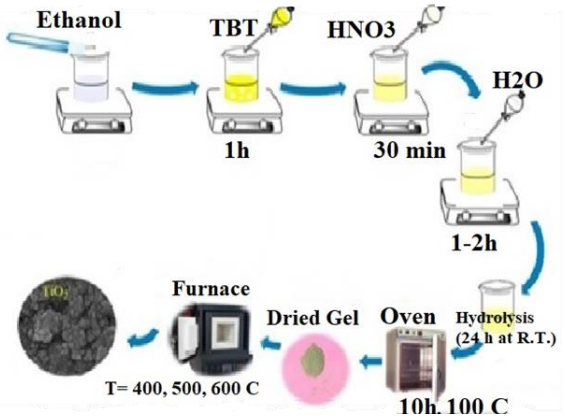


**Figure 1.** Schematic diagram of preparation of $TiO_2$ nanoparticles by sol–gel method.

### 2.3. Nanoparticle Characterization Methods

To check the phase transformation of the jelly sample obtained from titania sol, it was subjected to air atmosphere using TG-DTA analysis with a heating rate of 10 °C/min. The crystal structure and degree of crystallization of the samples were recorded using the MPD-XPERT model XRD machine with a wavelength of $\lambda$ = 1.54 Å in the angle range of 2θ = 20-80˚, available at Malayer University.

To determine the specific surface area of the synthesized nanoparticles, a BET device (model Belsorp mini II, Japan) was used. The BET system measures the volume of nitrogen gas absorbed and desorbed by the

material surface at a constant temperature of liquid nitrogen (77 K). To investigate the optical properties and calculate the band gap energy of the synthesized samples of titania and titania nanoparticles in the presence of Zn and Ag dopants, a UV-Vis device (model 2000, manufactured by Spekol, Germany) was utilized, also available at Malayer University. X-ray Photoelectron Spectroscopy (XPS) was recorded by a PHI 5000C spectrometer using MgKα radiation (hυ = 1253.6 eV). The reference peak for calibrating the device was C1s at 284.6 eV.

Field Emission Scanning Electron Microscope (FE-SEM), MIRA3-TESCAN (10-15 kV) model, and Transmission Electron Microscopy (TEM: Philips EM208, 100 kV) were used to examine the morphology.

### 2.4 Photocatalytic Activity

In this research, the photocatalytic test involved the degradation of methylene blue solution with a concentration of 10 ppm in the presence of synthesized nanoparticles. To determine the amount of absorption, 0.1 g of the synthesized powder was added to the methylene blue solution, and the light absorption was measured at different time intervals under visible light radiation at a wavelength of 664 nm (the maximum absorption for methylene blue) using a spectrophotometric device. The irradiation time for the synthesized samples was set at 1 hour, with intervals of 15, 30, 45, and 60 minutes. Using Equation (1), the degradation percentage of pollutant was calculated based on the absorption peaks (Zou at al., 2017).

$$\eta(\%) = (1 - A_t/A_0) \times 100 \quad (1)$$

In this relation, $A_0$ represents the initial absorption without radiation in the dark environment (t = 10 min at dark place), and $A_t$ the absorption of methylene blue solution after irradiation in different time intervals. Spectrophotometer data was used to obtain the $A_t$ value. To measure the band gap energy of the synthesized samples in this research, first, 0.01 g of the synthesized powder was ultrasonicated with 8 ml of EtOH and 2 ml of $HNO_3$ for 1-2 hours and then, all samples were irradiated. Visible light UV-VIS spectroscopic analysis was also performed.

The optical band gap energy ($E_g$) of the samples was calculated using the relationships and previous research (Ahmadi at al., 2021), as summarized in the following formula:

$$E_g\ (eV) = 1240/\lambda_{edge} \quad (2)$$

where $\lambda_{edge}$ represents the absorption limit of the semiconductor obtained from the UV-Vis spectrophotometric results.

## 3. RESULTS AND DISCUSSION

### 3.1. TG-DTA analysis

In Figure 2, the differential thermal analysis curve of pure titania gel is presented.

An endothermic peak is observed in the temperature range of 0 to 135 °C, which is associated with the release of ethanol solvent, water, and volatile substances in the raw materials (8.66 wt%). An exothermic peak occurs in the temperature range of 375 to 425 °C, corresponding to the maximum crystallization temperature of the anatase phase at 395 °C. Another exothermic peak appears in the temperature range of 520 to 580 °C, related to the transformation of the anatase phase to rutile (500 °C) (Choi at al., 1994). The second stage of weight loss, which occurs at temperatures above 135 °C and accounts for about 10%, is associated with the removal of structural water and the phase transformation of titanium hydroxide to titanium dioxide. The weight change curve at temperatures above 600 °C remains almost constant, indicating the complete removal of water and other organic compounds, with a total weight loss of 15.88%. Based on the results of thermal analysis, the temperature range of 400 to 600 °C has been selected for the calcination process of the samples.

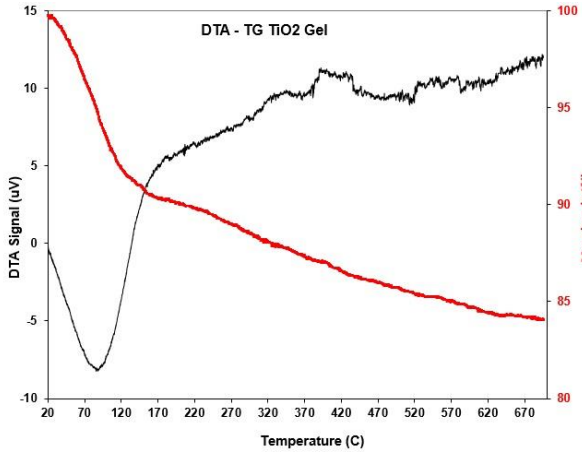


**Figure 2.** TG-DTA curve titania precursor gel.

### 3.2. XRD Analysis

The phase analysis of pure (T) and doped samples (AT, ZT, AZT) calcined at 400 °C is given in Figure 3a. All peaks at this temperature across all samples are attributed to the anatase phase with reference code 21-1272, observed at the angles (2θ) of 25.45, 37.5, 47.7, 54.26, 55.62, and 62.97, respectively. These angles align with the Miller indices (101), (112), (200), (105), (211), and (204), respectively. In the doped samples, the partial shift of the (101) plane to lower angles (Figure 3b) is observed, attributed to the larger ionic radius of the dopant elements ($Ag^{+}$-$Zn^{2+}$) compared to the matrix phase ($Ti^{4+}$). This peak shift was greater in the codoped sample (AZT400), as shown in Figure 3b.

Figure 3a shows no trace of the oxide peaks from $Ag_2O$ and ZnO metal cations, nor from $Zn^{2+}$ and $Ag^{+}$ cations in any of the samples. This absence indicates the successful replacement of metal cations within the titania lattice. The addition of dopants increases the distance between plates (d(hkl)), broadens the peak widths (β), and decreases their intensity, all of which provide evidence for the presence of dopants in the titania lattice, suggesting finer grains. The crystallite sizes of the T, AT, ZT, and AZT samples calcined at 400 °C are 9.15, 8.87, 7.72, and 4.15 nm, respectively. Furthermore, the addition of transition metals to the structure of titania nanoparticles inhibits the phase transformation from anatase to rutile (Lal at al., 2021).

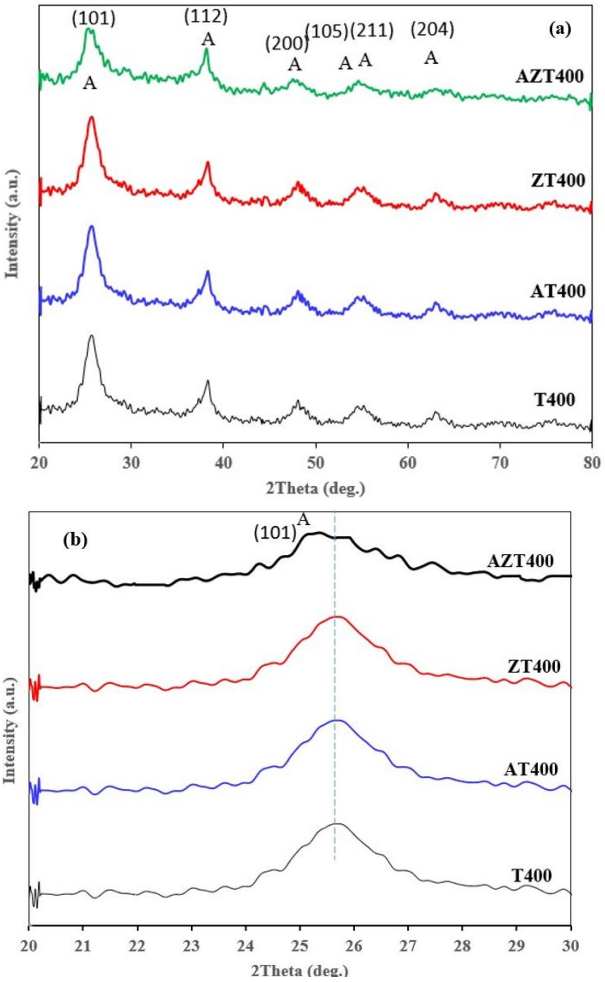


**Figure 3.** a) XRD patterns of pure sample (T400) and codoped $TiO_2$ mesoporous nanoparticles (AT, ZT, AZT) calcined at 400 °C for 1 h, b) shift (101) peak with details.

The XRD results of the doped sample at different temperatures (400, 500 and 600 °C) are reported in Figure 4. As the calcination temperature increases, the intensity of the peaks in all samples also increases, indicating a rise in the crystallinity of the structures. Conversely, with increasing temperature, there is a higher percentage of the rutile phase compared to the anatase phase. The percentage of phases and the crystallite sizes of the samples are reported in Table 1.

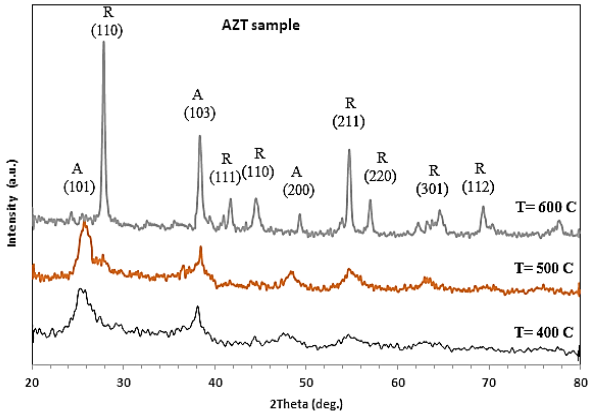


**Figure 4.** XRD samples of Ag/Zn codoped $TiO_2$ (AZT) mesoporous nanoparticles calcined at different Temperatures.

**TABLE 1.** Physical properties of doped samples synthesized at different temperatures.

| Samples | Crystallite size (nm) | A (%) | R (%) | BET ($m^2/g$) |
|---|---|---|---|---|
| AZT400 | 4.15 | 100 | - | 133.8 |
| AZT500 | 8.13 | 86 | 14 | 49.5 |
| AZT600 | 13.6 | 7 | 93 | 6.4 |

According to Table 1, the crystallite size of AZT400 is equal to 4.15 nm. At a temperature of 400 °C, we observed 10% of the anatase phase; as the temperature increased, the percentage of the rutile phase also increased. At 500 °C, there is 86% anatase and 14% rutile, calculated using the following formula (Eq. 3). At 600 °C, the percentage of the rutile phase has increased to 93%. The crystallite sizes of the samples at 500 °C and 600 °C are 8.13 nm and 13.6 nm, respectively. The percentage of the rutile phase in the sample is calculated using the following equation (Choi at al., 1994)

$$X_R = (1+0.8I_A/I_R)^{-1} \quad (3)$$

where, $X_R$ represents the weight percentage of rutile phase while $I_A$ and $I_R$ denote the peak intensity at diffraction angles of 25.4 corresponding to the (101) plane of the anatase phase and 27.3 corresponding to the (110) plane of the rutile phase.

### 3.3. Optical Analysis

The results of UV-Vis spectrophotometric analysis of AZT samples calcined at different temperatures (400, 500, 600 °C) are shown in Figure 5. The highest amount (57.9%) of photocatalytic degradation corresponds to the sample synthesized at 500 °C. According to the phase analysis of the AZT calcined at 500 °C, we can see that it consists of two phases, anatase and rutile, with a higher percentage of the anatase phase compared to the rutile phase (Table 1). According to some research, a

combination that includes both anatase and rutile phases, with a higher percentage of the anatase phase relative to the rutile phase, demonstrates better photocatalytic activity (Usha at al., 2016).

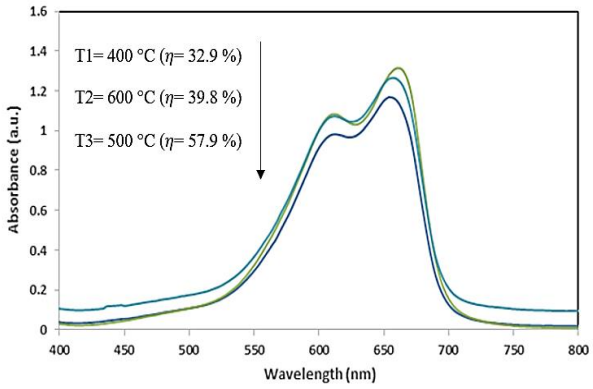


**Figure 5.** UV-Vis analysis of MB solution in the presence of AZT at different temperatures during 1h under visible light irradiation.

In fact, the main factor contributing to the separation of electrons and holes is the presence of the rutile phase in the structure alongside the anatase phase (Zou at al., 2017). Excited electrons in the rutile phase move to the conduction band of the anatase phase, creating a hole in the valence band of the rutile phase, thereby reducing electron-hole recombination (Ahmadi at al., 2021). Generally, the mixture of the two phases, anatase and rutile, facilitates the transfer of electrons from the anatase phase to the rutile phase (which has a lower energy level). This transfer reduces the rate of recombination in the catalysts of the two-phase mixture and improves electron-hole separation, leading to increased photocatalytic activity. Additionally, the sample calcined at 600 °C exhibits the highest degradation after the sample calcined at 500 °C, which can be attributed to the greater crystallization of the structure.

The proposed mechanism in this research for the photocatalytic process is as follows: $TiO_2$ is an optically active semiconductor. When it is exposed to light with an energy equal to or greater than its band gap energy ($E_g$), electrons are excited from the Valence Band (VB) to the Conduction Band (CB), thus creating positive holes ($h^+$) at the valence level. $TiO_2$ nanoparticles doped with Ag can indirectly change the charge transfer process on the surface and act as an effective electron acceptor. Reduction in the electron-hole pair recombination can lead to photocatalytic activity. Ag fermi level is lower than $TiO_2$ conduction band, and electrons can easily transfer from $TiO_2$ conduction band to Ag. Therefore, it is possible to form a Schottky barrier in the contact area of Ag and $TiO_2$. Like Ag, Zn cation has a lower fermi level than $TiO_2$, thus enabling it to trap the excited electrons. As a result, the presence of a small amount of metal in contact with the photocatalyst can trap the generated electrons ($e^-$) and holes ($h^+$) and prevent their recombination. Given that Ag and Zn fermi level is lower than $TiO_2$, electrons can be easily transferred from $TiO_2$ to Ag and Zn. In this case, it is not possible to recombine these electrons with holes created on the surface of $TiO_2$. Consequently, more holes areformed on the surface and participate in oxidation reactions - OH and $H_2O$ to hydroxyl radicals. Hydroxyl radicals have a high oxidation potential to destroy the pollutants and turn them into $CO_2$ and $H_2O$.

The BET-BJH analysis of the nanoparticles was also conducted. All the calcined samples (AZT400, AZT500, AZT600) exhibit a mesoporous structure, which is most pronounced in the AZT500 sample (Figure 6). The BET surface areas ($m^2/g$) of the nanoparticles at calcination temperatures of 400, 500, and 600 °C are approximately 133, 49, and 6 $m^2/g$, respectively. The results of this analysis for the AZT samples at three temperatures 400, 500, and 600 °C are reported in Table 1. The hysteresis loop for this sample is classified as type IV according to the IUPAC standard (Gorgani at al., 2020, Dinkar at al., 2016), and the absorption-desorption curve indicates that this sample possesses a mesoporous structure. The average pore diameter in the AZT500 sample is 8.3 nm (Fig- 6b).

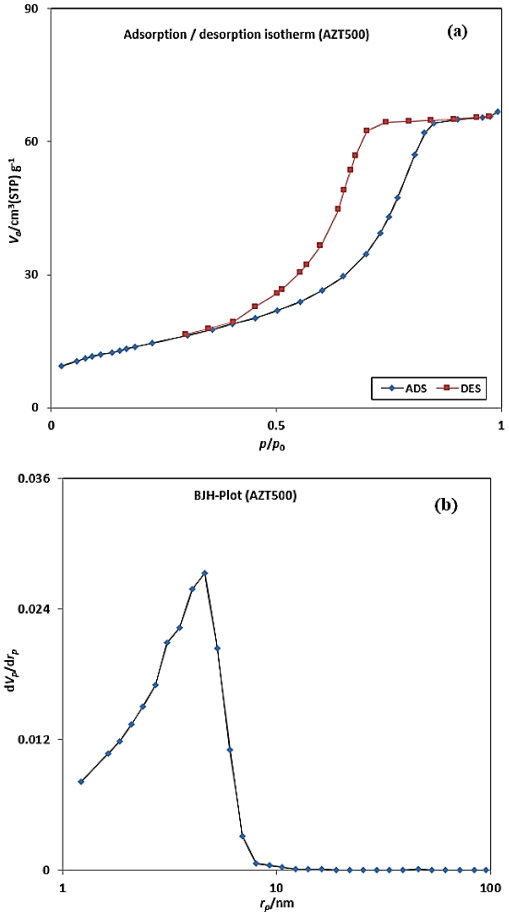


**Figure 6.** N2 physisorption isotherms (BET) of AZT500 mesoporous nanoparticles calcined at 500 °C. a) BET, b) BJH.

The results of the band gap energy (Eg) of the sample, along with the valence band energy (EVB) and conduction band energy (EcB) of pure and codoped TiO2 samples at temperatures of 400, 500, and 600 °C, are reported in Table 2. Typically, the absorption spectrum of the AZT500 sample, shown in Figure 7, is reported to calculate the band gap energy using Formula 2.

Using the optical band gap energy (Eg) results of the samples and the equations below (Eq. 4 and 5), the valence band energy and conduction band energy of the samples were calculated and reported in Table 2.

$$E_{VB} = X - E_e - 0.5 \times E_g \quad (4)$$

$$E_{CB} = E_{VB} - E_g \quad (5)$$

where $E_{VB}$ is the valance band edge potential, X the electronegativity of the semiconductor which is the geometric mean of the electronegativity of the constituent atoms (X of $TiO_2$ is 5.81 eV), $E_e$ the free electron energy in the hydrogen scale (4.5 eV) (Gupta at al. 2012, Khan at al., 2017), and $E_g$ the optical band gap.

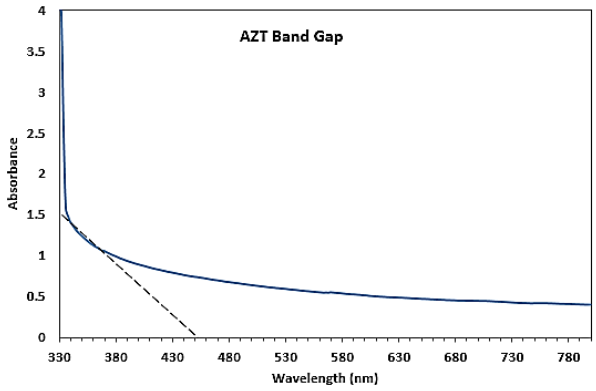


**Figure** 7. UV-Vis spectra of AZT500.

**TABLE 2.** Optical properties of synthesized samples at different temperatures

| Sample | Eg (eV) | VB (eV) | CB (eV) |
|---|---|---|---|
| T400 | 3.22 | 2.92 | - 0.3 |
| T500 | 2.88 | 2.75 | - 0.13 |
| T600 | 2.83 | 2.73 | - 0.105 |
| AZT400 | 3.06 | 2.84 | - 0.217 |
| AZT500 | 2.75 | 2.69 | - 0.062 |
| AZT600 | 2.25 | 2.44 | - 0.109 |

### 3.4. XPS Analysis of AZT-500 sample

The chemical states of the elements in T500 and AZT500 samples were analyzed based on the XPS analysis, the results of which are given in Figure 8. Figure 8a is the broad spectrum of pure titania sample (T500). As shown in Figure 8a, the presence of Ti and O elements indicates the presence of pure titania in the composition. Additionally, a wide scan of the doped sample (AZT500) is shown in Figure 8b. The presence of Ag and Zn cations indicates the doping of these cations in the titania structure. For further investigation, higher resolution spectra of the samples were obtained. The high-resolution Ti 2p spectrum of the AZT500 sample is shown in Fig.8c. Two peaks are observed around the binding energies of 458.3 eV and 464.3 eV, which correspond to Ti 2p3/2 and Ti 2p1/2, respectively. The binding energy difference between these two peaks is about 6 eV, confirming the presence of the Ti element in the form of $Ti^{4+}$ (Dinkar at al., 2016). Figure 8d displays the high-resolution Ag 3d spectrum of the AZT500 sample. The two peaks identified at binding energies of 372.1 eV and 378.8 eV are related to Ag 3d5/2 and Ag 3d3/2. There is an energy difference of 6.7 eV between the binding energies of the Ag peaks, indicating that Ag is in the Ag0 state on the $TiO_2$ lattice (Khan at al., 2017). Figure 8e Figure 8e shows two peaks related to the presence of Zn cations at binding energies of 1021.9 eV and 1045.7 eV, corresponding to Zn 2p3/2 and Zn 2p1/2. The difference in binding energy between these two peaks is 23.8 eV, indicating the presence of Zn2+ ions in the sample (Choi at al., 1994). The XPS spectrum of the O1s level (Figure 8f) is indicative of a chemical state for oxygen. The lattice oxygen in the crystal ($O_L$) of $TiO_2$ is approximately 530.5 eV. The O 1s spectrum can be split into two types of oxygen species: (I) the binding energy at 530.5 eV, which is associated with the lattice oxygen ($O_L$); and (II) the 531.4 eV peak, which is assigned to the hydroxyl groups (OH) (Ana at al. 2023, Ghotbi at al., 2020, Kingsley at al., 2021).

### 3.5. Morphological Analysis

FESEM analyses have been used to investigate the morphology of pure and doped titania nanoparticles. From the optimal photocatalytic conditions (AZT500), FESEM images and elemental analysis (EDS) have been obtained, as shown in Figures 9. As depicted in the images (Figure 9a), the nanoparticles are largely agglomerated, with a particle size range of 25-50 nm for the pure sample (T500, Figure 9a) and 15-30 nm for the doped sample (T500, Figure 9a) and 15-30 nm for the doped sample (AZT500, Figure 9b). The elemental analysis (EDS) of the samples confirmed the presence of titanium and oxygen elements in the pure sample (Figure 9c) as well as the presence of titanium, oxygen, zinc, and silver elements in the doped sample (AZT500, Figure 9d).

To accurately check the size of the particles, the analysis of transmission electron microscope images was carried out. TEM images of the sample calcined at 500 °C with the best photocatalytic conditions are shown in Figure 10. The particle size distribution is in the range of 10-20 nm (Figure 10a). The interplanar spacing was estimated using HRTEM images (Figure 10b), obtaining values of 0.351 nm and 0.335 for the anatase and rutile phase.

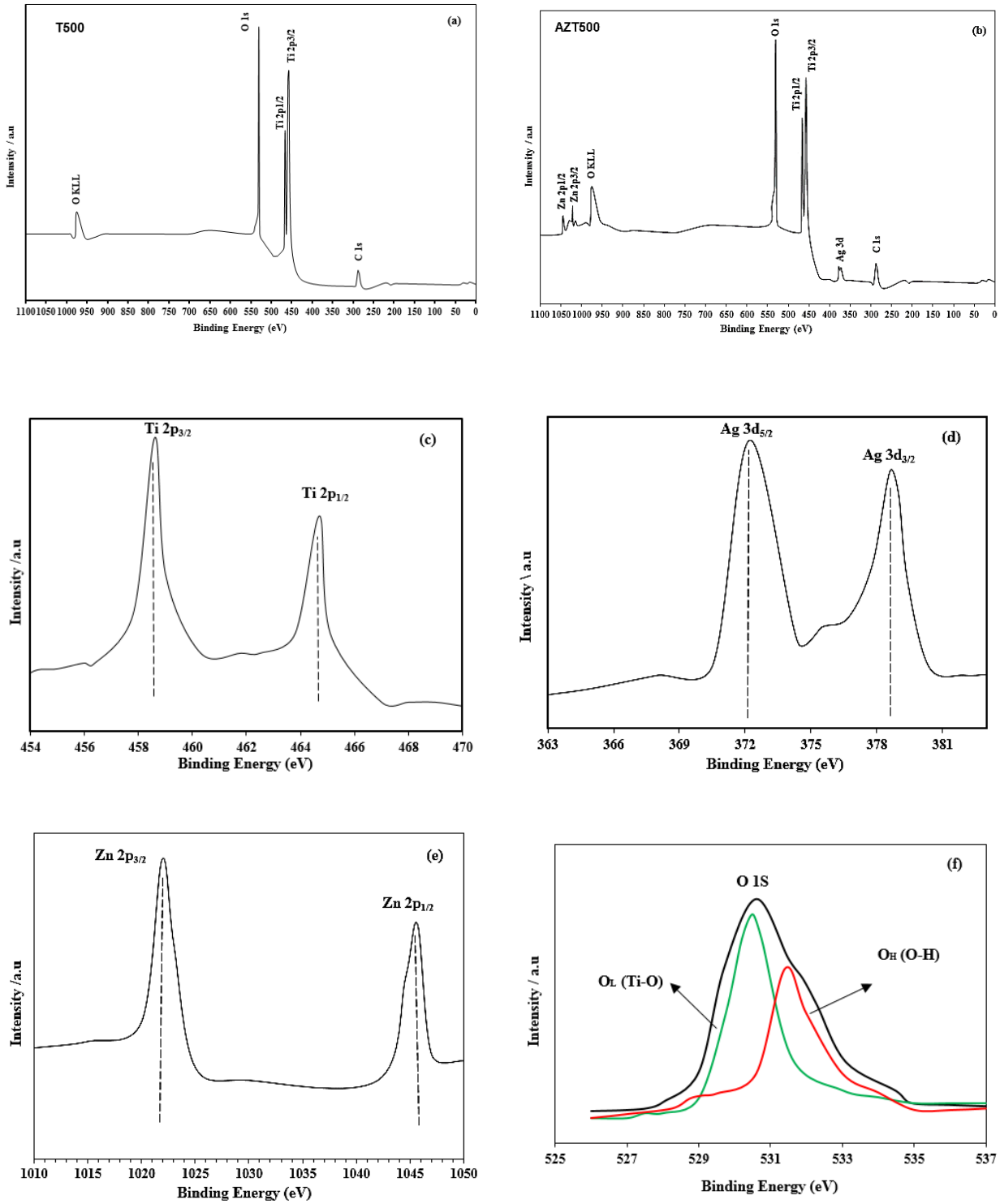


**Figure 8.** XPS spectra (a) wide scan of pure $TiO_2$ nanoparticles (T500), (b) codoped $TiO_2$ nanoparticles (AZT500) calcined at 500 °C, (c) Ti2p region (d), Ag 3d region, (e) Zn 2p region and (f) O 1s region.

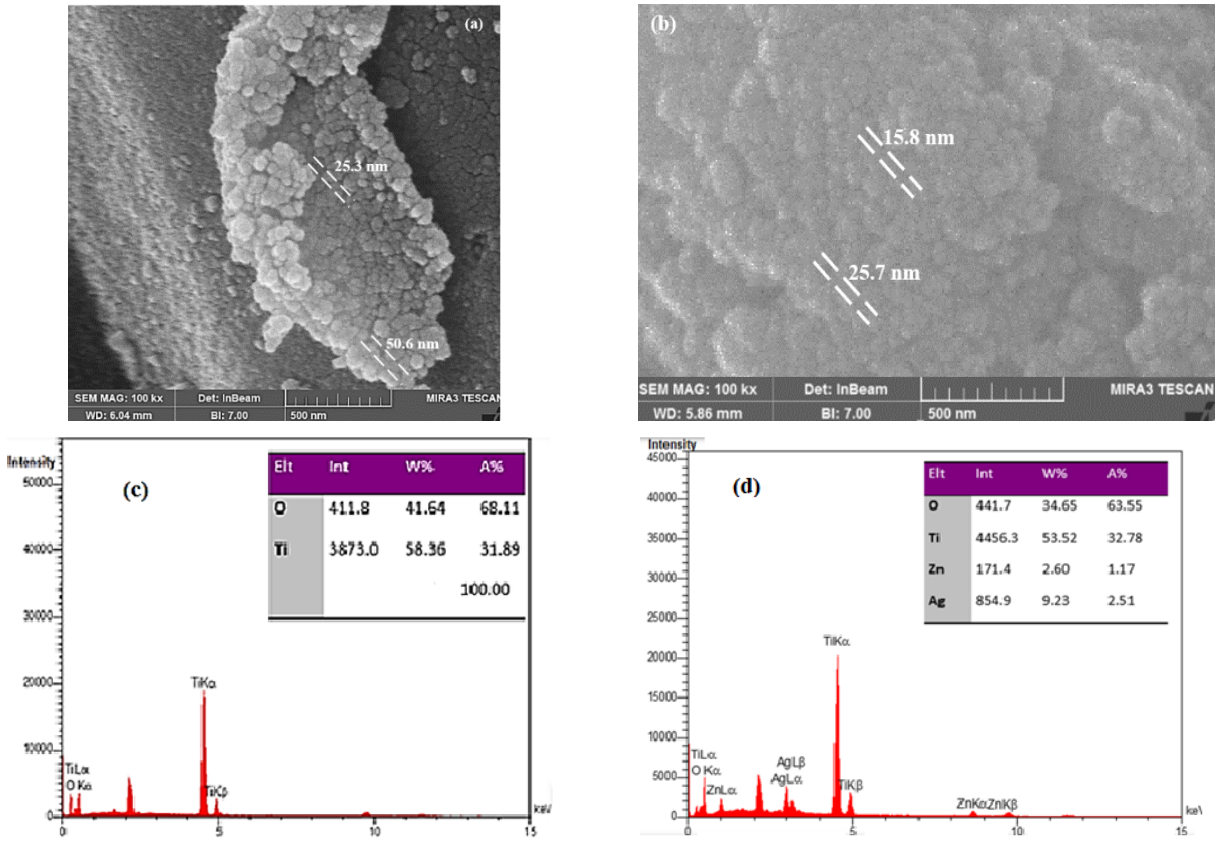


**Figure 9.** FESEM-EDS images of undoped $TiO_2$ (**a, c**) and codoped (AZT) sample (**b, d**) calcined at 500 °C.

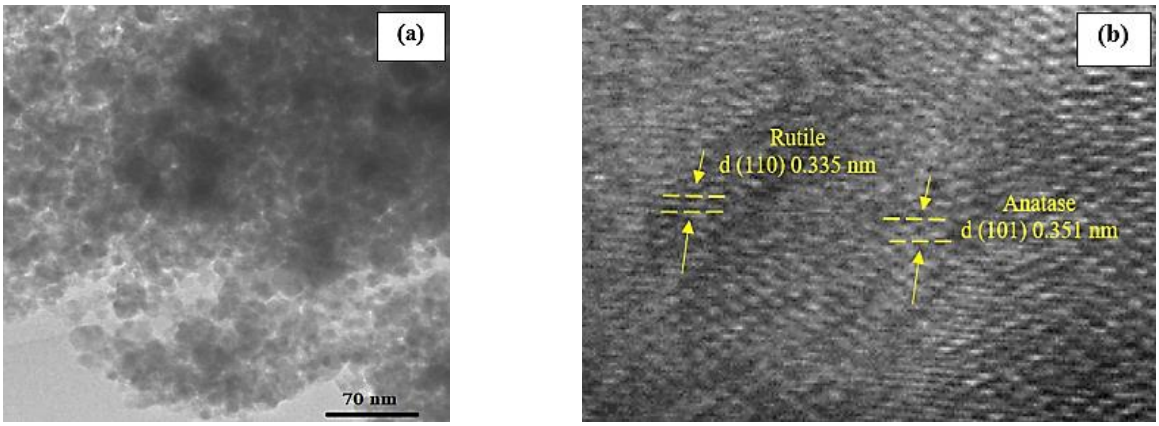


**Figure 10.** The TEM (a) and HRTEM (b) images of an AZT500 nanoparticles.

Briefly, one of the parameters affecting the photocatalytic activity of the samples is the surface area of the particles, which, in turn, depends on their morphology (spherical, needle-shaped, rod-shaped, amorphous, etc.). Considering that nanoparticles with dimensions less than 25 nm were obtained during the synthesis process, it is expected that these particles will exhibit better photocatalytic properties. Based on the results from Figure 9 and Figure 10, the synthesized particles have an almost spherical shape. According to the BET results (Table 1), they are suitable for photocatalytic activity due to their high specific surface area. To study the effects of morphology and other parameters such as specific surface area on photocatalytic activity, both the as-grown and air-annealed nanostructures were tested for methylene blue (MB) degradation under Visible light. Of note, the morphology of a sample affects the optical properties. The significance of morphology control depends not only on modifications of the band gap (Table 2) but also on the efficiency of the photocatalytic process. The crystallinity, porosity, and morphology of a sample are closely related to the synthesis methodology, which is

why it is necessary to find a method that allows for the control of these properties.

## 4. CONCLUSION

In this research, $TiO_2$ nanoparticles codoped with Ag and Zn were prepared using the sol-gel method. The results are as follows:

- By incorporating Ag and Zn cations into the of titania nanoparticles, the crystalline particle size is reduced, and the phase transformation from anatase to rutile is prevented. In other words, the doping of these two cations in the titania lattice acts as a stabilizer for the anatase phase.
- Increasing the calcination temperature of the AZT samples led to a decrease in specific surface area, which reached 133.8 $m^2/g$ at 400 °C and 49.5 $m^2/g$ at 500 °C. This increase in temperature also caused the particle size to grow from 4.15 nm to 8.13 nm.
- The best photocatalytic properties were observed in the AZT sample calcined at 500 °C, where its degradation percentage was 57.9%.
- An increase in calcination temperature from 400 °C to 600 °C resulted in a decrease in band gap energy from 3.06 eV to 2.25 eV.
- The results from FESEM analysis showed that the particle size of the synthesized sample at the optimal photocatalytic degradation temperature (500 °C) was smaller than that of the undoped $TiO_2$ sample. The particle size range for the undoped $TiO_2$ (T500) sample was approximately 25–50 nm, while the range for the AZT500 sample was about 15–30 nm.

## ACKNOWLEDGMENTS

This study was funded by Malayer University. The authors highly acknowledge the financial support of Malayer University.

## REFERENCES

1. Ahmadi, M. & Koozegar Kaleji B. (2021). TCA (Ag doped $TiO_2$-CuO) mesoporous composite nanoparticles: optical, XPS and morphological characterization, *Journal of Materials Science, Materials in Electronic*, *32*, 13450-13461. https://doi.org/10.1007/s10854-021-05923-5

2. Anpo, M. (2004). Preparation characterization, and reactivities of highly functional titanium oxide-based photocatalysts able to operate under UV–visible light irradiation: approaches in realizing high efficiency in the use of visible light. *Bulletin of the Chemical Society of Japan*, *77*, 1427–1442. https://doi.org/10.1246/bcsj.77.1427

3. Ana E. Cardozo, Elsa M. Farfán Tores, Graciela V. Morales, Edgardo L. Sham (2023) Sol–gel synthesis of $TiO_2$ doped with chromium: photocatalytic degradation of tartrazine, *Academia Materials Science*, *1*, 1-9. https://doi.org/10.20935/AcadMatSci6142

4. Bellotti, V., Daldossi, C., Perilli, D., D'Arienzo, M., Stredansky, M., Di Valentin, C., & Simonutti, R. (2023). Mechanism of sustainable photocatalysis based on doped-titanium dioxide nanoparticles for UV to visible light induced PET-RAFT photo-polymerization. *Journal of Catalysis*, *428*, 115074. https://doi.org/10.1016/j.jcat.2023.07.015

5. Choi, W., Termin, A. & Hoffmann, M.R. (1994). The role of metal ion dopants in quantum-sized $TiO_2$: correlation between photoreactivity and charge carrier recombination dynamics. *Journal of Physical Chemistry. 98*, 13669–79. http://dx.doi.org/10.1021/j100102a038

6. Aware, D. V. & Jadhav, S. S. (2016). Synthesis, characterization and photocatalytic applications of Zn-doped $TiO_2$ nanoparticles by sol–gel method, *Applied Nanoscience*, 6, 965–972. https://doi.org/10.1007/s13204-015-0513-8

7. Gupta, S. & Tripathi, M. (2012). A review on the synthesis of $TiO_2$ nanoparticles by solution route, *Open Chemistry., 10 (2)*, 279–294. https://doi.org /10.2478/s11532-011-0155-y

8. Ghotbi M.Y., Javanmard A. & Soleimani H. (2020). A casting strategy to produce 3D bulk monolithic carbon and N-doped carbon nanosheets with high surface area and low volume, *Microporous and Mesoporous Materials*, *293*, 109791. https://doi.org/10.1016/j.micromeso.2019.109791

9. Gorgani M. & Koozegar Kaleji B. (2020). Structural, photocatalytic and surface analysis of Nb/Ag codoped $TiO_2$ mesoporous nanoparticles, *Journal of Sol-Gel Science and Technology*, *96*, 728–741. https://doi.org/10.1080/03067319.2020.1767096

10. Ilkhechi, N.N., Ahmadi, A., & Koozegar Kaleji, B. (2015). Optical and structural properties of nanocrystalline anatase powders doped by Zr, Si and Cu at high temperature, *Optical Quantum Electronic*, *47(8).* 2423–2434. https://doi.org/ 10.1007/s11082-015-0120-7

11. Khan, S., Cho, H., Kim, D., Han, S.S., Lee, S.H. K.W., Cho, S.H., Song, T. & Choi, H. (2017). Defect engineering toward strong photocatalysis of Nb-doped anatase $TiO_2$: Computational predictions and experimental verifications, *Applied. Catalyst B Environmental*, *206*, 520–530. https://doi.org/10.1016/j.apcatb.2017.01.039

12. Egbo, K. O., Shil, S. K., Kwok, C. G., Wang, Y., Liu, C. P., & Yu, K. M. (2021). Band alignment of wide bandgap NiO/MoO3 and NiO/WO3 pn heterojunctions studied by high-resolution X-ray photoelectron spectroscopy. *Journal of Alloys and Compounds*, *876*, 160136. https://doi.org/10.1016/j.jallcom.2021.160136

13. Kunnamareddy, M., Rajendran, R., Sivagnanam, M., Rajendran, R., & Diravidamani, B. (2021). Nickel and sulfur codoped TiO 2 nanoparticles for efficient visible light photocatalytic activity. *Journal of Inorganic and Organometallic Polymers and Materials*, *31*, 2615-2626. https://doi.org/10.1007/s10904-021-01914-5

14. Lal, M., Sharma, P., & Ram, C. (2021). Calcination temperature effect on titanium oxide (TiO2) nanoparticles synthesis. *Optik*, *241*, 166934.\. https://doi.org/10.1016/j.ijleo.2021.166934

15. Mikrut, P., Kobielusz, M., Indyka, P., & Macyk, W. (2020). Photocatalytic activity of TiO2 polymorph B revisited: physical, redox, spectroscopic, and photochemical properties of TiO2 (B)/anatase series of titanium dioxide materials. *Materials Today Sustainability*, *10*, 100052. https://doi.org/10.1016/j.mtsust.2020.100052

16. Mohammad, M. R., Ahmed, D. S., & Mohammed, M. K. (2019). Synthesis of Ag-doped TiO 2 nanoparticles coated with carbon nanotubes by the sol–gel method and their antibacterial activities. *Journal of Sol-Gel Science and Technology*, *90*, 498-509. https://doi.org/ 10.1007/s10971-019-04973-w

17. Rahmawati, T., Butburee, T., Sangkhun, W., Wutikhun, T., Padchasri, J., Kidkhunthod, P., ... & Sapcharoenkun, C. (2023). Green synthesis of Ag-TiO2 nanoparticles using turmeric extract and its enhanced photocatalytic activity under visible light. Colloids and Surfaces A: *Physicochemical and Engineering Aspects*, *665*, 131206. https://doi.org/10.1016/j.colsurfa.2023.131206

18. Rahimi, S., Koozegar Kaleji, B., & Kazazi, M. (2023). ZnxCo3-xO4 Hydrothermally Mesoporous Nanoparticles (ZCH): Structure, Optical, and Surface Analysis. *Advanced Ceramics Progress, 9(1)*, 28-37. https://doi.org/10.30501/acp.2023.379335.1115

19. Rathi, V. H., Jeice, A. R., & Jayakumar, K. (2023). Green synthesis of Ag/CuO and Ag/TiO2 nanoparticles for enhanced photocatalytic dye degradation, antibacterial, and antifungal properties. *Applied Surface Science Advances*, *18*, 100476. https://doi.org/10.1016/j.apsadv.2023.100476

20. Savio, A. K. P. D., Fletcher, J., Smith, K., Iyer, R., Bao, J. M., & Hernández, F. R. (2016). Environmentally effective photocatalyst CoO–TiO2 synthesized by thermal precipitation of Co in amorphous TiO2. *Applied Catalysis B: Environmental*, *182*, 449-455. https://doi.org/ 10.1016/j.apcatb.2015.09.047

21. Usha, K., Kumbhakar, P., & Mondal, B. (2016). Effect of Ag-doped TiO2 thin film passive layers on the performance of photo-anodes for dye-sensitized solar cells. *Materials Science in Semiconductor Processing*, *43*, 17-24. https://doi.org/10.1016/j.mssp.2015.11.015

22. Vasiljevic, Z. Z., Dojcinovic, M. P., Vujancevic, J. D., Jankovic-Castvan, I., Ognjanovic, M., Tadic, N. B., ... & Nikolic, M. V. (2020). Photocatalytic degradation of methylene blue under natural sunlight using iron titanate nanoparticles prepared by a modified sol–gel method. *Royal Society open science*, *7(9)*, 200708. https://doi.org/10.6084/m9.figshare.c.5105934.

23. Wang, D., Leng, Z., Hüben, M., Oeser, M., & Steinauer, B. (2016). Photocatalytic pavements with epoxy-bonded TiO2-containing spreading material. *Construction and building materials*, *107*, 44-51. https://doi.org/10.1016/j.conbuildmat.2015.12.164

24. Zou, Z., Zhou, Z., Wang, H., & Yang, Z. (2017). Effect of Au clustering on ferromagnetism in Au doped TiO2 films: theory and experiments investigation. *Journal of Physics and Chemistry of Solids*, *100*, 71-77. https://doi.org/10.1016/j.jpcs.2016.09.011

Advanced Ceramics Progress: Vol. 10, No. 1, (Winter 2024) 44-48

Materials and Energy Research Center
MERC

Contents lists available at ACERP

Advanced Ceramics Progress

Journal Homepage: www.acerp.ir

**Original Research Article**

# Effect of NiO Sintering Aid on the Electrical Properties of KNN-LST Lead-free Piezoceramics

Mehdi Delshad Chermahini
*Assistant Professor, Department of Materials Engineering, Faculty of Engineering, University of Shahrekord, Iran.*
* Corresponding Author Email: mdelshadcher@gmail.com (M. Delshad Chermahini)
URL: https://www.acerp.ir/article_182921.html

*ARTICLE INFO*

*Article History:*
Received: 01 September 2023
Revised: 03 November 2023
Accepted: 09 November 2023

*Keywords*:
Piezoelectric,
KNN,
Solid-state,
Microstructure

*ABSTRACT*

The current research focuses on the synthesis and characterization of sodium potassium niobate (KNN), a lead-free piezoelectric compound. The objective is to replace lead-based compounds like PZT using KNN-LST, which is sodium potassium niobate piezoceramic powder doped with lithium, antimony, and tantalum. To this end, solid-state method was employed to sinter the samples at 1110 °C with varying percentages of NiO sinter aid (0%, 0.75%, 1.5%, and 2.25%). X-ray diffraction analysis confirmed the formation of pure KNN-LST perovskite phase at 1110 °C with a composition containing 1.5% NiO. Scanning electron microscope images also demonstrated that cubic particles inherent in KNN were observed in samples with no NiO addition as well as those containing 0.75% and 1.5% NiO; however, these particles were transformed into cylindrical grains when incorporating 2.25% NiO. With an increase in the sintering percentage from zero NiO content to higher amounts, sample density also increases from approximately 85% up to its peak at around 94%, followed by a slight decrease by about 91%. Similarly, the dielectric coefficient increased from approximately850 without any contribution from NiO sinter addition up to1500 upon addition of 1.5%NiO sinter but then, it decreased again by approximately 1200 followed by addition of 2.25% NiO sinter. Conversely, dielectric loss initially reduced from roughly 0.14% during no NiO sinter addition by merely 0.04% during 1.

https://doi.org/10.30501/acp.2023.414402.1130

## 1. INTRODUCTION

The most important piezoelectric ceramic (lead titanate zirconate) has great applications in transducers, sensors and actuators because of its remarkable ferroelectric properties and high electromechanical nature (Chermahini et al., 2020) (Schmid, 2008) (Chermahini et al., 2018). Investigation of the lead-free piezoelectric materials gains significance particularly because of the undeniable damages of Pb to the environment (Surowiak et al., 2001) (Shieh et al., 2007) (Sushkov et al., 2008) (Yamamoto, 1996) (Cross, 1987). In addition, a great deal of attention has been paid to the sodium-potassium niobate (KNN) as the most important candidate for lead free material. It is an atomic mixture of NaNbO3 (NN) and KNbO3 (KN) ceramics (Yamamoto, 1996) (Cross, 1987) (Shafiee et al., 2019). The special torsion of octahedral voids in the NN ceramics makes its crystal structure more complicated than KN symmetry (Liu & Ren, 2009) (Halliday, 2005) (Kumar & Pattanaik, 2013) (Marandian Hagh et al., 2007) mainly due to the unfitting size of Na cations for corners of perovskite structure (Cross, 1987). Therefore, from the energy point of view, the structure of KN is more stable than the NN symmetry (Li et al., 2013) (Ye, 2008) (Nan et al., 2008) (Eerenstein et al., 2006). It is expected that the structure of KNN be similar to KN due to its high stability (Pullar, 2012). Up to 220 °C, the KNN

Please cite this article as: Delshad Chermahini, M. (2024). Effect of NiO Sintering Aid on the Electrical Properties of KNN-LST Lead-free Piezoceramics, *Advanced Ceramics Progress*, 10(1), 44-48. https://doi.org/10.30501/acp.2023.414402.1130

2423-7485/© 2024 The Author(s). Published by MERC.
This is an open access article under the CC BY license (https://creativecommons.org/licenses/by/4.0/).

piezoceramics show a duplicated unit cell with orthorhombic system (Shafiee et al., 2019). This orthorhombic structure of KNN (at room temperature) transforms into tetragonal symmetry at 220 °C. This effective phenomenon is known as Polymorphic Phase Transition (PPT) (Merz, 1956). It is established that the great electromechanical nature of the KNN system is a function of PPT behavior as well as Morphotropic Phase Boundary (MPB) (Bibes & Barthélémy, 2008) (Franke et al., 1994). The latter occurs when two types of piezoelectric symmetries are simultaneously present in the individual composition (Halliday, 2005). In the KNN case, the PPT phenomenon occurs at about 220 °C, and the MPB is detected in the K0.5Na0.5Nb2O5 composition (Franke et al., 1994). In order to decrease the PPT temperature in the application area, use of some additives such as lithium, tantalum, and antimony are frequently recommended (Schmid, 2008) (Chermahini et al., 2018) (Surowiak et al., 2001) (Shieh et al., 2007) (Sushkov et al., 2008) (Yamamoto, 1996) (Cross, 1987) . In addition, some sintering aids such as NiO, $MnO_2$, and $Y_2O_3$ that are frequently used in KNN based piezoceramic to improve the densification of bulk ceramics (Chermahini et al., 2018) (Surowiak et al., 2001) (Shieh et al., 2007) (Sushkov et al., 2008) (Yamamoto, 1996) (Cross, 1987) . This study aims to address the synthesis challenges throughout the production process of ceramic powders based on sodium-potassium niobates to achieve high-quality tablets with the desired electrical properties. Key considerations include precise initial mixing techniques and preventing evaporation of volatile elements such as sodium, potassium, and lithium. The traditional ceramic methods were employed in the present study to prepare lead-free piezoceramic powders to subsequently investigate their dielectric and piezoelectric characteristics.

## 2. MATERIALS AND METHODS

High-purity primary powders including Na2Co3, Ta2O5, Sb2O3, Nb2O5, K2Co3, and Li2Co3 were purchased from Aldrich company and then, they were utilized to synthesize piezoceramic powder using sodium-potassium niobate doped with antimony (Sb), lithium (Li), and tantalum (Ta) through the ceramic method. To mitigate moisture absorption by sodium and potassium carbonate powders during synthesis, a pre-drying step was conducted at 110 °C for one day. The solid-state approach was employed for the synthesis process at 900 °c for 2 h. The synthesis materials were combined with 0 to 2.25 % wt. Ni0. Then, the resulting powder was mixed with a weight ratio of 3% PVA solution. Tablets of approximately13 mm in diameter and 0.7 mm in thickness were prepared under the pressure of 300 MPa using uniaxial press. The tablets were sintered at 1120 °C for 2 h. The relative density of the sintered samples was determined based on Archimedes' method. Subsequently, X-ray diffraction analysis was carried out using Philips device within two-theta range between 20° and 80°. CuKα X-ray wavelength production was verified with the step size of 0.02° and scan rate of 0.5 step/s. Scanning Electron Microscope (SEM, PHILIPS XL30) was employed for microstructural characterization, investigating the particle morphology and porosity in the KNN-LST piezoceramic. Dielectric properties were measured using an LCR meter (CHY 41R) at the frequency of 10 KHz.

## 3. RESULTS AND DISCUSSION

Figure 1 illustrates the X-Ray Diffraction (XRD) pattern of the synthesized piezoceramic based on sodium potassium niobate doped with lithium (Li), antimony (Sb), and tantalum (Ta) at the synthesis temperature of 1110 °C.

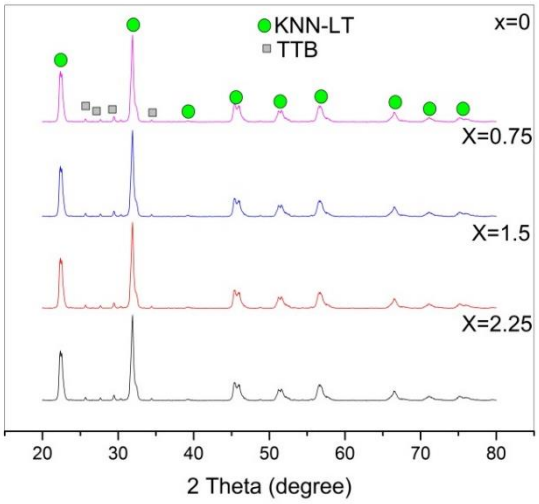


**Figure 1.** The XRD pattern of sintered samples at 1110 oC with various NiO content (x)

The analysis was conducted using Xpert software, enabling phase and structure investigations on the synthesized powder. The observed peaks correspond to both the main peaks of sodium potassium niobate and additional peaks attributed to the impurity phases , i.e., Tetragonal Tungesten Boronze (TTB), formed during the synthesis process of KNN-LST piezoceramics. In Figure 1, the circles represent the main peaks while the squares show the impurity peak symbols. The desired structure for piezoelectric sodium potassium niobate ceramic doped with Li, Sb, and Ta is a perovskite structure without central symmetry. However, the presence of an impurity phase in sodium potassium niobate-based piezoelectrics has a detrimental effect that causes a sharp decline in electrical properties (Schmid, 2008). In case the concentration of impurities exceeds an optimal value specific to electroceramic applications, it can even render the electrical properties

ineffective (Chermahini et al., 2020). The identified impurity phase known as tungsten-bronze exhibits a chemical formula K3LiNb6O17 (Sushkov et al., 2008). Its formation results from the incomplete reaction between raw materials during the synthesis process. This tungsten-bronze impurity phase forms at lower temperatures and remains stable up to 850°C; therefore, its removal from the system becomes essential to enhance the electrical properties in piezoceramic samples. Overall, these results highlight not only successful synthesis of sodium-potassium niobate-based piezoceramics but they emphasize the necessity of careful control over impurities to achieve desirable electrical characteristics essential for effective utilization in various electroceramic applications.

The SEM images provided in Figure 2 verify the presence of piezoelectric phase formation across different percentages of sintering agent.

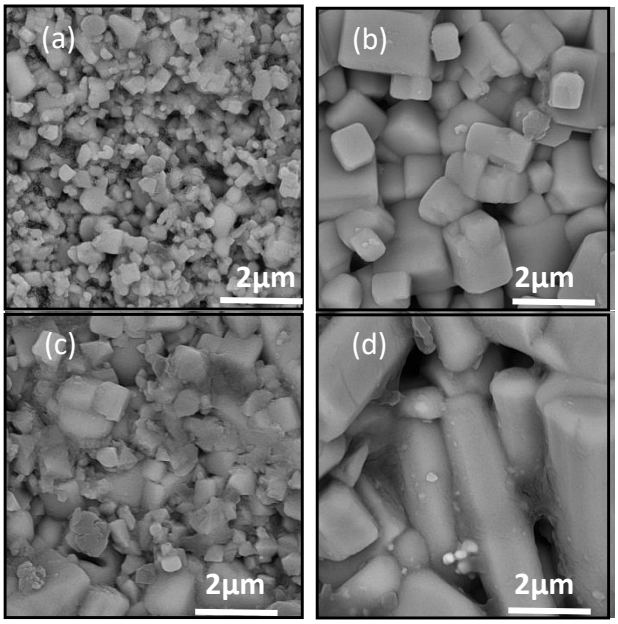


**Figure 2.** The SEM migrograph of sintered samples at 1110 oC for various NiO content (x)

The captured images taken by a scanning electron microscope (FESEM) on the fractured surfaces of these samples illustrate the size and shape of piezoceramic particles in sodium potassium niobate doped with lithium, antimony, and tantalum at various sintering agent percentages ranging from 0% to 2.25%. Figure 2 clearly shows the cubic morphology characteristics of KNN-LST piezoceramics in samples containing 0% and 0.75% sintering aids, indicating successful formation of the desired phase. Comparisons made between these observed morphologies and previous studies are noteworthy (Surowiak et al., 2001). In samples with 1.5% sinter addition, apart from grains exhibiting cubic morphology, the presence of a molten phase is visibly evident as well. As observed in the SEM micrographs, from 0 to 1.5% sintering aids, the whole porosity of ceramics decreases. It can be expected that in the mentioned range, the sample density decreases. This observation aligns with the typical characteristics seen in piezoceramic samples where increasing percentage of sinter aid results in larger grain growth for greater structural uniformity ultimately leading to higher density. As depicted by their considerable distribution within each sample composition, all piezoceramic compositions exhibit cubic particle morphology when varying amounts of sinter assistance are employed. Moreover, the absence of defects along boundaries indicates that agglomerates have been successfully broken down during pressing, resulting in the presence of KNN-LST cubic particles within the powder structure. The sample containing 2.25% displays a change in seed morphology accompanied by specific outward growth tendencies.

Figure 3 illustrates the relationship between composition and relative density in various percentages of NiO sinter contribution, ranging from 0% to 2.25%.

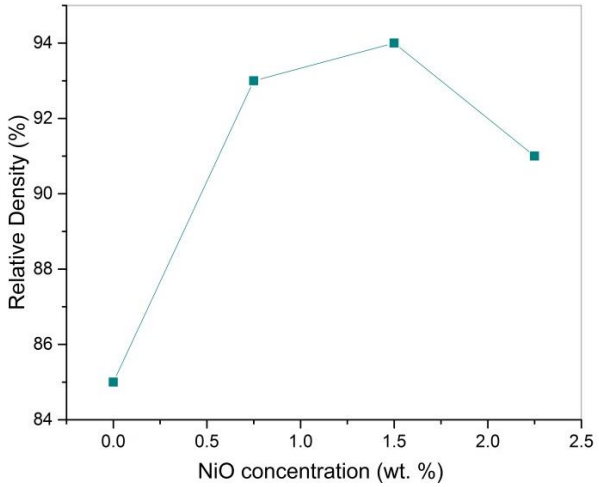


**Figure 3.** The relative density of sintered samples at 1110 ºC for various NiO content (x)

In the piezoceramic sample of sodium potassium niobate doped with lithium, antimony, and tantalum, the relative density increased gradually from 85% at 0%. NiO sintering aid to a peak value of 94% at 1.5% NiO sintering aid before declining to 2.25%. These findings indicate that the relative density of this particular piezoceramic is highly sensitive to the percentage of sintering aid used. Notably, a relative density above 90%, achieved at the content of 1.5%, signifies excellent quality for sodium potassium niobate-based piezoceramics. This increase can be attributed to the formation of an intermediate phase (Madab phase) between grains during sintering, which promotes proper grain-to-grain bonding and enhances piezoelectric properties.

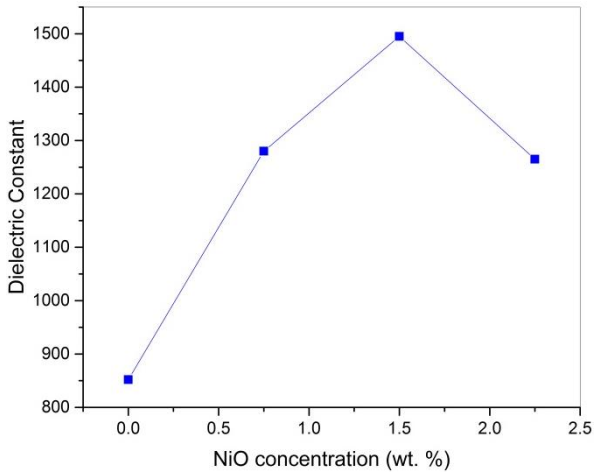


**Figure 4.** The dielectric constant of sintered samples at 1110 ºC as afunction of NiO content (x)

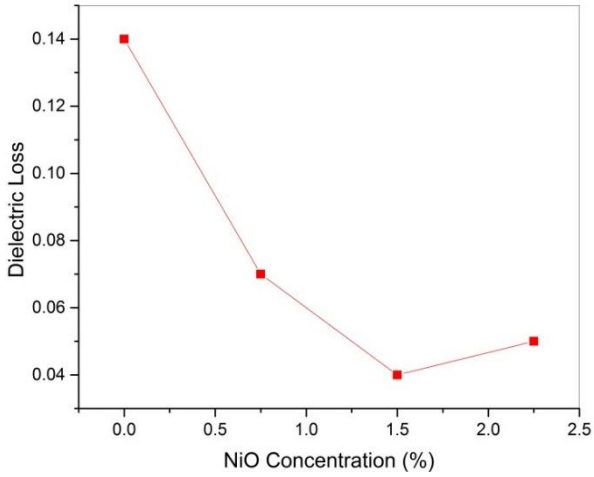


**Figure 5.** The dielectric loss of sintered samples at 1110 ºC as afunction of NiO content (x)

Further increment in the sintering aid content from 1.5 to 2.25 % causes a decrease in the relative density probably due to the abnormal grain growth during sintering caused by higher amount of sintering aids content (Surowiak et al., 2001) (Sushkov et al., 2008) (Sushkov et al., 2008) (Sushkov et al., 2008) (Shafiee et al., 2019). Figure 4 shows variations in dielectric constant (Ɛr) across different percentages of NiO sinter contribution in sodium potassium niobate samples doped with lithium, antimony, and tantalum.

## 4. CONCLUSION(S)

The synthesis of KNN-LST compound with a perovskite structure was successfully achieved using the solid-state method and calcination process, and the findings are summarized in the following. The solid-state method proved effective in eliminating the impurity peaks caused by incomplete raw material reactions, leading to improved piezoelectric and dielectric properties in the samples. Upon employing the solid-state method along with ball milling, the particle size was reduced by 2 micrometers, thus enhancing the overall quality of the synthesized KNN-LST compound. The dielectric constant of the produced KNN-LST composition initially increased and then decreased as the percentage of sintering aid contribution was raised, implying that there was an optimal percentage for achieving maximum dielectric constant. Similarly, as the sintering aid contribution percentage increased, the dielectric loss of the produced KNN-LST compound first decreased and then increased, highlighting an optimal range for minimizing dielectric loss again. Based on our findings, it can be concluded that an ideal sintering aid contribution percentage to achieve the desired properties is 1.5% for KNN-LST combination. Sintering aids at the concentration of 1.5% NiO resulted in complete formation of KNN-LST composition during the sintering process. Overall, these results provide valuable insights into optimizing synthesis methods and identifying critical factors influencing key properties such as piezoelectricity and dielectrics within KNN-LST compounds.

## ACKNOWLEDGEMENTS

The authors appreciate Mrs. N.pirkhalili for her sincere support throughout the research process.

## REFERENCES

1. Bibes, M., & Barthélémy, A. (2008). Towards a magnetoelectric memory. *Nature materials*, 7(6), 425-426. https://doi.org/10.1038/nmat2189
2. Chermahini, M. D., Safaee, I., Shahraki, M. M., Rahimipour, M. R., & Derakhshandeh, M. R. (2020). Magnetodielectric effect in novel multiferroic (1-x)(K0. 49Na0. 47Li0. 04)/(Ta0. 1Sb0. 06Nb0. 84) O3/xNi0. 1Mn0. 2Co0. 7Fe2O4 nanocomposites. *Journal of Alloys and Compounds*, 838, 155423. https://doi.org/10.1016/j.jallcom.2020.155423
3. Chermahini, M. D., Shahraki, M. M., & Kazazi, M. (2018). Multiferroic properties of novel lead-free KNN-LT/20NZCFO magneto-electric composites. *Materials Letters*, 233, 188-190. https://doi.org/10.1016/j.matlet.2018.09.001
4. Cross, L. E. (1987). Relaxor ferroelectrics. *Ferroelectrics*, 76(1), 241-267. https://doi.org/10.1080/00150198708016945
5. Eerenstein, W., Mathur, N., & Scott, J. F. (2006). Multiferroic and magnetoelectric materials. *nature*, 442(7104), 759-765. https://doi.org/10.1038/nature05023
6. Franke, K., Besold, J., Haessler, W., & Seegebarth, C. (1994). Modification and detection of domains on ferroelectric PZT films by scanning force microscopy. *Surface Science*, 302(1-2), L283-L288. https://doi.org/10.1016/0039-6028(94)91089-8
7. Halliday, D., Resnick, R., Walker, J., John Wiley & Sons, inc (2005). Fundamentals *of physics*. https://bcs.wiley.com/college/bcs/redesign/student/0_0471216437_BKS_2037___00.html
8. Kumar, P., & Pattanaik, M. (2013). Synthesis and characterizations of KNN ferroelectric ceramics near 50/50 MPB. *Ceramics International*, 39(1), 65-69. https://doi.org/10.1016/j.ceramint.2012.05.093

9. Li, J. F., Wang, K., Zhu, F. Y., Cheng, L. Q., & Yao, F. Z. (2013). (K, Na) NbO 3-based lead-free piezoceramics: fundamental aspects, processing technologies, and remaining challenges. *Journal of the American Ceramic Society*, 96(12), 3677-3696. https://doi.org/10.1111/jace.12715

10. Liu, W., & Ren, X. (2009). Large piezoelectric effect in Pb-free ceramics. *Physical review letters*, 103(25), 257602. https://doi.org/10.1103/PhysRevLett.103.257602

11. Marandian Hagh, N., Jadidian, B., & Safari, A. (2007). Property-processing relationship in lead-free (K, Na, Li) NbO3-solid solution system. *Journal of Electroceramics*, 18(3), 339-346. https://doi.org/10.1007/s10832-007-9171-x

12. Merz, W. J. (1956). Switching time in ferroelectric BaTiO3 and its dependence on crystal thickness. *Journal of applied physics*, 27(8), 938-943. https://doi.org/10.1063/1.1722518

13. Nan, C.-W., Bichurin, M., Dong, S., Viehland, D., & Srinivasan, G. (2008). Multiferroic magnetoelectric composites: Historical perspective, status, and future directions. *Journal of applied physics*, 103(3). https://doi.org/10.1063/1.2836410

14. Pullar, R. C. (2012). Hexagonal ferrites: a review of the synthesis, properties and applications of hexaferrite ceramics. *Progress in Materials Science*, 57(7), 1191-1334. https://doi.org/10.1016/j.pmatsci.2012.04.001

15. Schmid, H. (2008). Some symmetry aspects of ferroics and single phase multiferroics. *Journal of Physics: Condensed Matter*, 20(43), 434201. https://doi.org/10.1088/0953-8984/20/43/434201

16. Shafiee, E., Chermahini, M. D., Doostmohammadi, A., Nilforoushan, M. R., & Zehipour, B. (2019). Influence of sintering temperature on densification, microstructure, dielectric and ferroelectric properties of Li/Sb Co-doped KNN pizoceramics. *Ceramics International*, 45(17), 22203-22206. https://doi.org/10.1016/j.ceramint.2019.07.242

17. Shieh, J., Wu, K., & Chen, C. (2007). Switching characteristics of MPB compositions of (Bi0. 5Na0. 5) TiO3–BaTiO3–(Bi0. 5K0. 5) TiO3 lead-free ferroelectric ceramics. *Acta materialia*, 55(9), 3081-3087. https://doi.org/10.1016/j.actamat.2007.01.012

18. Surowiak, Z., Kupriyanov, M., & Czekaj, D. (2001). Properties of nanocrystalline ferroelectric PZT ceramics. *Journal of the European Ceramic Society*, 21(10-11), 1377-1381.https://doi.org/10.1016/S0955-2219(01)00022-X

19. Sushkov, A., Mostovoy, M., Aguilar, R. V., Cheong, S., & Drew, H. (2008). Electromagnons in multiferroic RMn2O5 compounds and their microscopic origin. *Journal of Physics: Condensed Matter*, 20(43), 434210. https://doi.org/10.1088/0953-8984/20/43/434210

20. Yamamoto, T. Y. T. (1996). Ferroelectric properties of the PbZrO3–PbTiO3 system. *Japanese journal of applied physics*, 35(9S), 5104. https://doi.org/10.1143/JJAP.35.5104

21. Ye, Z. (2008). Handbook of advanced dielectric, *piezoelectric* and ferroelectric materials. Synthesis, *properties and applications. CRC Press*. https://doi.org/10.1007/s10832-007-9171-x

# Advanced Ceramics Progress

**Volume 10, Number 1, Winter 2024**

CONTENTS



**Journal Home Page: www.acerp.ir**